Doctoral Thesis

Fabrication and Effective Application of Strategically Designed Nano-Structures

Kwanghyun Kim

Department of Energy Engineering
(Energy Engineering)

Graduate School of UNIST

2018

ULSAN NATIONAL INSTITUTE OF
SCIENCE AND TECHNOLOGY

Fabrication and Effective Application of Strategically Designed Nano-Structures

Kwanghyun Kim

Department of Energy Engineering
(Energy Engineering)

Graduate School of UNIST

Fabrication and Effective Application of Strategically Designed Nano-Structures

A thesis/dissertation
submitted to the Graduate School of UNIST
in partial fulfillment of the
requirements for the degree of
Doctor of Philosophy

Kwanghyun Kim

6/29/2018
Approved by

____
Advisor
Ji-Hyun Jang

Fabrication and Effective Application of Strategically Designed Nano-Structures

Kwanghyun Kim

This certifies that the thesis/dissertation of Kwanghyun Kim is approved.

6/29/2018

Advisor: Ji-Hyun Jang

Jin Young Kim

Kwanyong Seo

Jungki Ryu

Ji-Wook Jang

Abstract

In this thesis, strategically designed nanostructures were fabricated by various methods and applied to several devices using solar energy conversion to enhance their performance through their many advantages such as enormous surface area, and light trapping effect *etc*.

To absorb the much more light energy for the efficient photoanode in the photo-electrochemical water splitting system, plasmonic effect of gold nano-particles and lower bandgap energy materials (CdSe and hematite) were used with the special three-dimensional patterned nano-structures such as surface textured inverse opal structure, hybrid structure and square patterned current collector. The structures trapped the incident light with the enormous surface area to help the visible light absorption and the charge transfer at the interfaces. As the results, photocurrent density values of the photoanodes were significantly improved. In addition, three-dimensionally mesoporous graphene-based nanostructure was fabricated via relatively simple procedure and utilized to the solar steam generation for the desalination of seawater. Therefore, the photothermal conversion and steam generation rate were dramatically improved compared with other control samples and pure water due to the advantages such as significantly enormous evaporation sites and capability of easy vapor-escaping to the air.

By strategically designing to have the capabilities needed for a variety of applications respectively, we could achieve the significantly enhanced efficiency much easily and effectively. There are a unlimited methods to make nanostructures with more interesting shapes, and a lot of applications that can maximize performance by using them effectively. Thus, this approach will continue to be applied effectively in various fields in the future.

Contents

List of figures

List of tables

Chapter 1

Introduction (Literature review)

1.1 Motivations

Recently, nanotechnology has been widely applied to many fields such as the materials, sensors, bio, and energy etc. The unit of “nano” means one billionth of one as shown in **Figure 1.1**. It is corresponding to the size of about three to four atoms. It means a technology that can control or change a very small (atomic scale) design. As it can has a lot of advantages to many applications, the scope of its use has expanded to include the manufacture of highly integrated devices, manufacturing of high performance sensors, and accurate diagnosis or curing system etc. Additionally, various nanomaterials can also improve the performance of many energy devices such as the photovoltaic facilities (dye-sensitized solar cells containing the nano-scaled semiconductor materials that mimic natural photosynthesis from green plants), wind power facilities (organic nano-materials utilization as coatings on the rotor blades of turbines for lower weight and increase of the energy yield), and lithium-ion batteries (improved storage capacity, stability, and lifespan *etc*. by the nano-optimized manufacturing procedures) *etc*. **Figure 1.2** shows the variety of energy fields for the nano-materials applications classified according to the priority reported at the European GENNESYS project. They also explain that nanotechnology in the energy field will give the significant impact to the efficiency of energy conversion and storage as the current performance barriers are overcome in the very short period. Especially, the most powerful and potential energy resource, solar energy, could be much improved to utilize and global funding has been supported a lot. In this thesis, various methods of making patterned nanostructures would be presented with their effect to improve the performance of solar energy conversion systems by utilizing many advantages strategically such as the photo-electrochemical water splitting for hydrogen generation and solar steam generation for seawater desalination and wastewater decontamination *etc*.

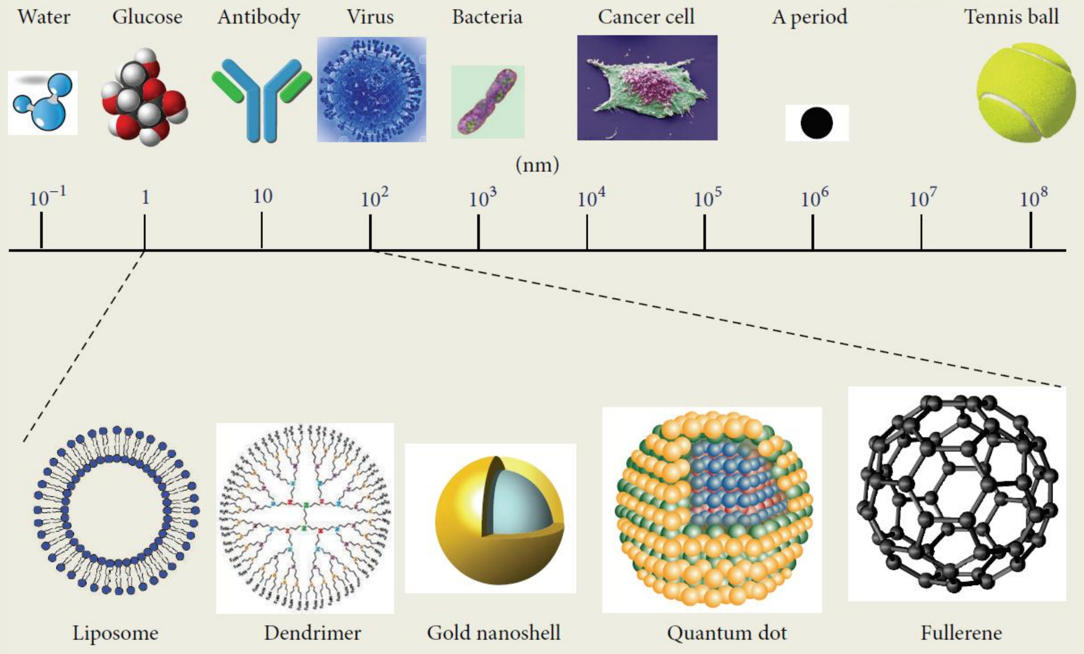

Figure 1.1 Nanometer unit ruler to show the comparison of nano-scaled materials.[1]

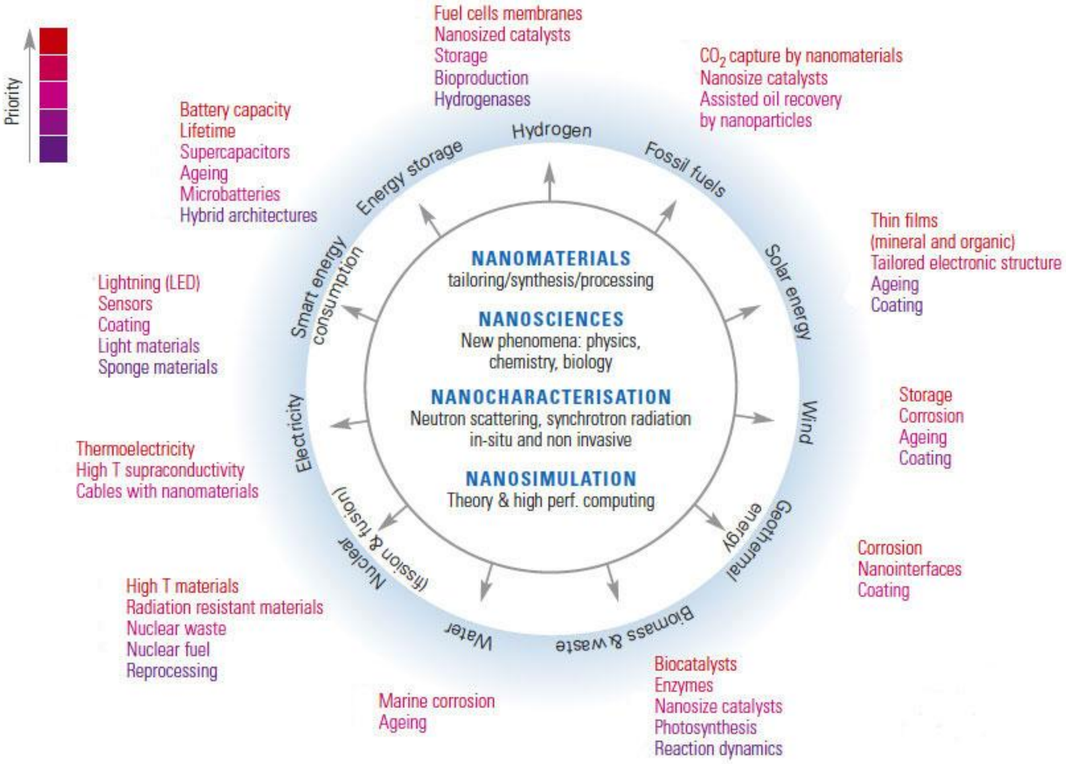

Figure 1.2 Research infrastructure for energy materials in nanotechnology.[2]

1.2 Fabrication of the periodic patterned structures

1.2.1 Self assembly

Self-assembly is the certified and reliable technique to attain outstanding qualities for various interesting shaped and periodically patterned nanostructures. Assembly of tiny unit cells to form the periodic patterned structures by the interaction of themselves is the self assembly. With the available neighboring interactions and forces between the tiny unit cells and without any external directions, any elements could be arranged by the assembled spontaneously, which results the self-aligned and assembled nanostructures. **Figure 1.3** shows the self assembled micelle shape block copolymers that can be transformed slightly through a series of procedures such as the addition of organic solvents and anisotropic growth *etc*. In addition to such spherical or disk-like shapes, nanostructures can be formed with a lamellar structure or a number of other interesting shaped patterns. Furthermore, self assembly can be combined other techniques for making periodic patterned nanostructures. **Figure 1.4** shows the regular metal vapor deposition treated onto the self assembled colloidal particles to make the two-dimensional nanostructures. It is the one of examples of combined technique with lithography that will be described from now on.

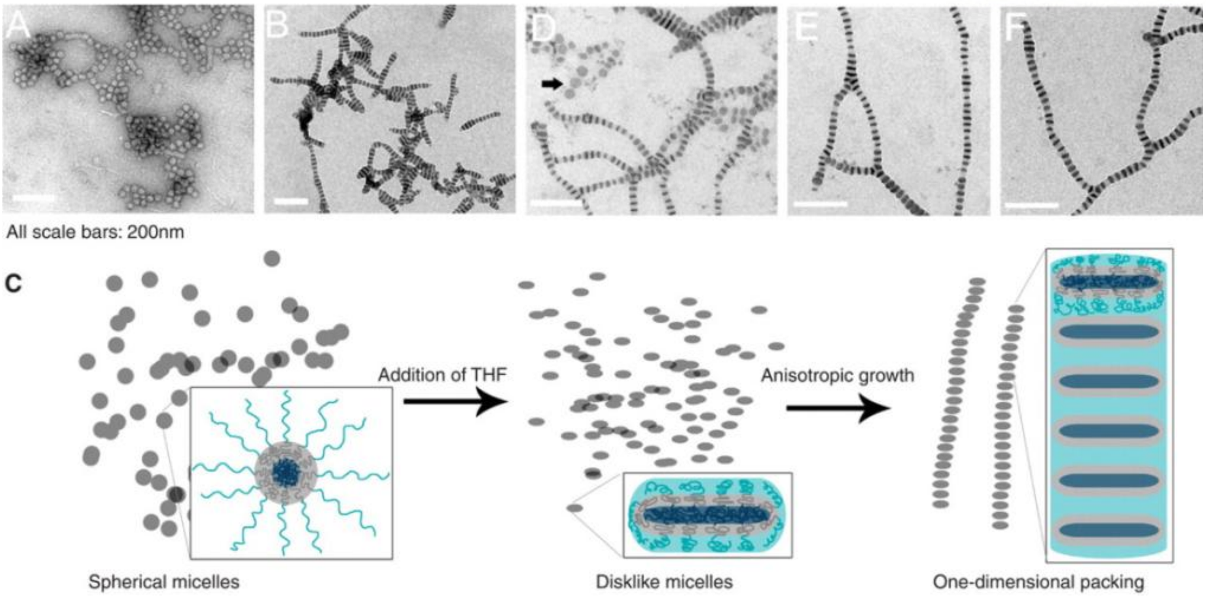

Figure 1.3 Self assembled block copolymers as various shaped micelles.[3]

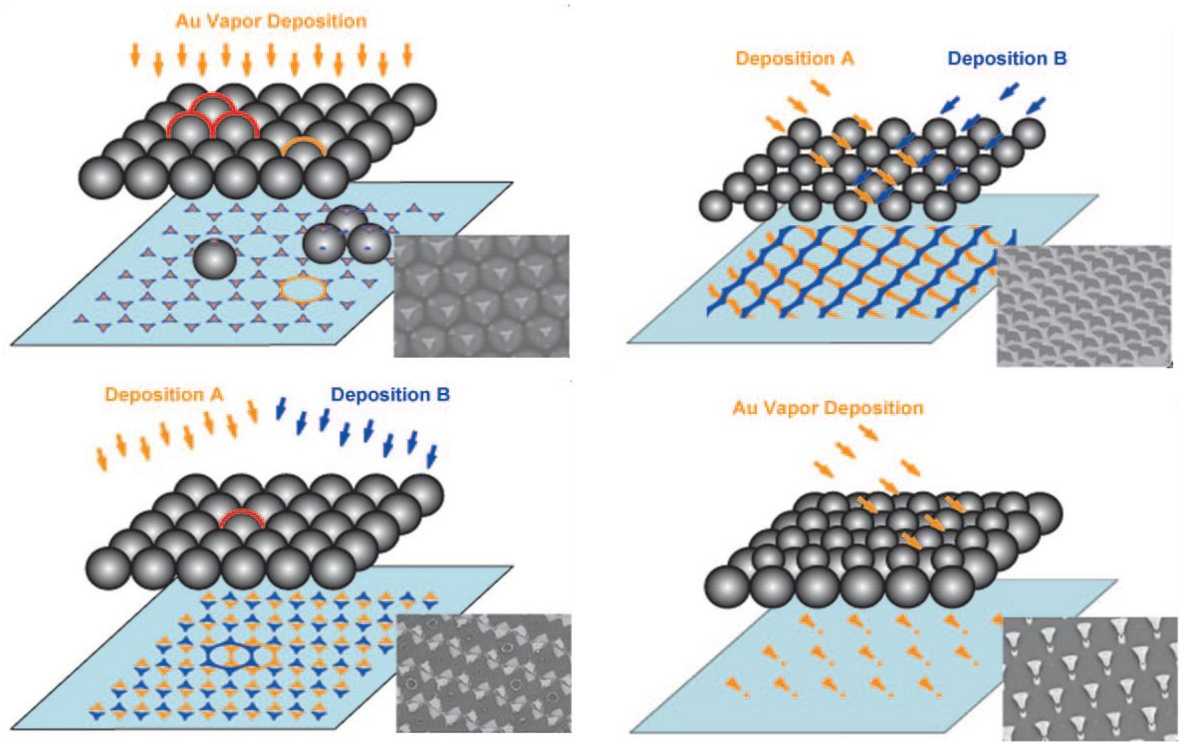

Figure 1.4 Regular metal vapor deposited lithography combined with self assembly of colloidal spheres.[4]

1.2.2 Lithography

Lithography has been the most effective technique in manufacturing fields of integrated devices, periodic pattened structures and microchips *etc*. There are various kinds of lithography techniques and their applications are even more varied as shown in **Table 1.1**. The lithography techniques are broadly divided into two types by the use of shadow masks; masked lithography and maskless lithography. Masked lithography can have a high throughput since the patterns can be fabricated over a wide area simultaneously using the mask (or mold). The representative masked lithography techniques are soft lithography and imprint lithography *etc*. On the other hand, maskless lithography includes electron beam lithography, focused ion beam lithography, and scanning probe lithography, which fabricates arbitrary patterns by a serial writing without the masks. These techniques create ultrahigh-resolution patterns of arbitrary shapes with a minimum feature size of a few nanometers. However, it is inappropriate for mass production due to the very low throughput. Here, the photolithography has been broadly used as both the masked and maskless methods. Interference photolithography, which uses interference phenomenon of multiple laser beams to fabricate periodically patternd nanostructures, is a very effective technique for forming clear and defect-free structures with very precise and fine patterns, and high throughput. The representative masked photolithography is the proximity field nanopatterning, called as PnP. **Figure 1.5** shows the schematic illustration of procedures for the fabrication of three-dimensional (3D) patterned nanostructures using a periodic patterned high-resolution phase mask. Placing such a phase mask onto the surface of a solid state photoresist polymer film leads to intimate, conformal contact driven by van der Waals forces at the first and second steps. When a laser beam is passing through a periodically patterned phase mask, a certain 3D interference phenomenon occurs in the photoresist film. Through this phenomenon, the patterns same as the interference are formed by cross-linking reactions in the photoresist film at third step. Finally, a developing process that rinses off non-crosslinked photoresist materials can be used to obtain elaborately formed 3D periodic-patterned structures. The one of the maskless methods of photolithography techniques is the multi-beam interference lithography. **Figure 1.6** shows the schematic illustration of procedures for the fabrication of holographic patterns using four laser beams from multiple directions, forming diamond-like interference. Same as the previous PnP lithography process, a structure with the same patterns as the interference patterns are fabricated elaborately through cross-linking and developing processes. These 3D patterned nanostructures made by various lithography techniques are applied to four major fields such as electronics and microsystems, medical and biotech, optics and photonics, and environment and energy harvesting, as shown in **Table 1.1**. In addition, rapid development of modern technology has created a number of 3D patterned nanostructures applicable fields, and the lithography technique must serve as a major role in innovation.

Table 1.1 Specifications and applications of the major lithography techniques.[5]

Lithography Technique	Minimum Feature Size	Throughput	Applications
Photolithography (contact & proximity printings)	2-3 μm [22]	very high	typical patterning in laboratory level and production of various MEMS devices
Photolithography (projection printing)	a few tens of nanometers (37 nm) [2]	high - very high (60-80 wafers/hr) [1]	commercial products and advanced electronics including advanced ICs [1], CPU chips
Electron beam lithography	< 5 nm [23]	very low [1, 3] (8 hrs to write a chip pattern) [1]	masks [3] and ICs production, patterning in R&D including photonic crystals, channels for nanofluidics [23]
Focused ion beam lithography	~20 nm with a minimal lateral dimension of 5 nm [2]	very low [3]	patterning in R&D including hole arrays [125, 134], bull's-eye structure [132], plasmonic lens [137]
Soft lithography	a few tens of nanometers to micrometers [2, 13] (30 nm) [2]	high	LOCs for various applications [13, 96]
Nanoimprint lithography	6-40 nm [14, 15, 18]	high (> 5 wafers/hr) [1]	bio-sensors [17], bio-electronics [18], LOCs: nano channels, nano wires [97, 102, 104]
Dip-pen lithography	a few tens of nanometers [39, 40, 43]	very low – low, possibly medium [39]	bio-electronics [43], bio-sensors [40], gas sensors [42]

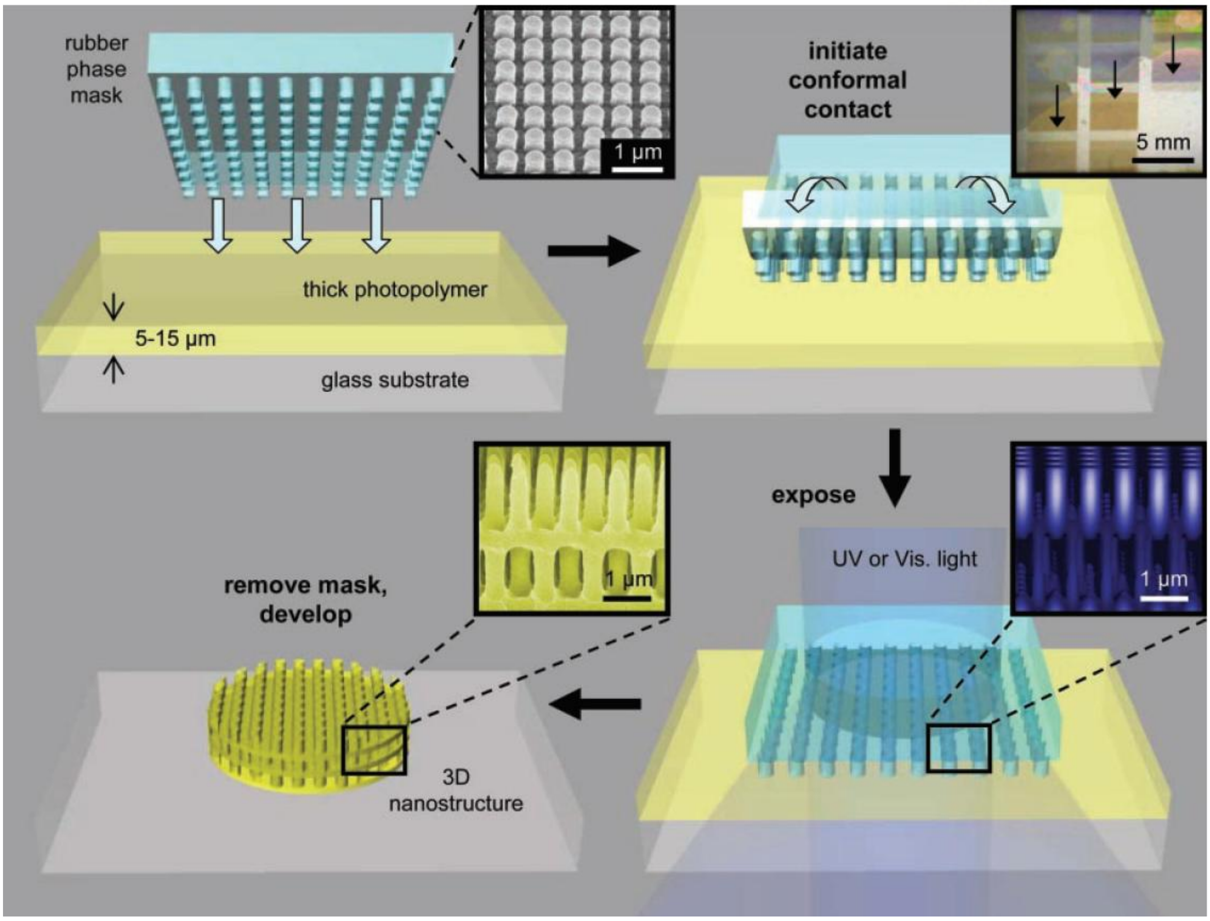

Figure 1.5 Scheme for the procedures of 3D patterned nanostructures through the PnP technique.[6]

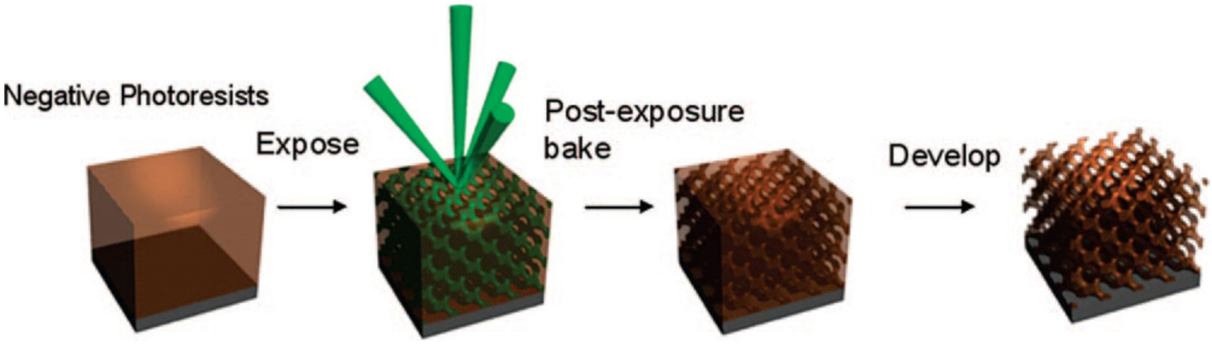

Figure 1.6 Scheme for the procedures of 3D patterned nanostructures through the 4 beam interference lithography technique.[7]

1.3 Advantages for efficient energy devices

1.3.1 Surface to volume ratio

The multi-dimensional nanostructures made by previous methods can be applied to various energy devices for their performance improvement due to the several advantages. The first one of the advantages is the excellent surface to volume ratio, compared with the bulk equivalents. **Figure 1.7** shows the typical example for the higher surface to volume ratio of nanostructures by using cubes. When the bulk cube is divided into eight smaller cubes again and again hierarchically, surface to volume ratio increases exponentially. Thus, assuming that such a unit cell is reduced to a nanometer scale size, the surface to volume ratio must be tremendously large. In other words, the total amount of exposed surfaces increased exponentially by dividing the cube into smaller components, but the total volume doesn't change from the initial value. The enormous surface area means the improvement of the reactions that can occur on the surface such as the physical ion adsorption and interfacial charge transfer *etc*. As the result, this much increased surface area is the very important advantage in that the 3D patterned nanostructures are utilized in various fields.

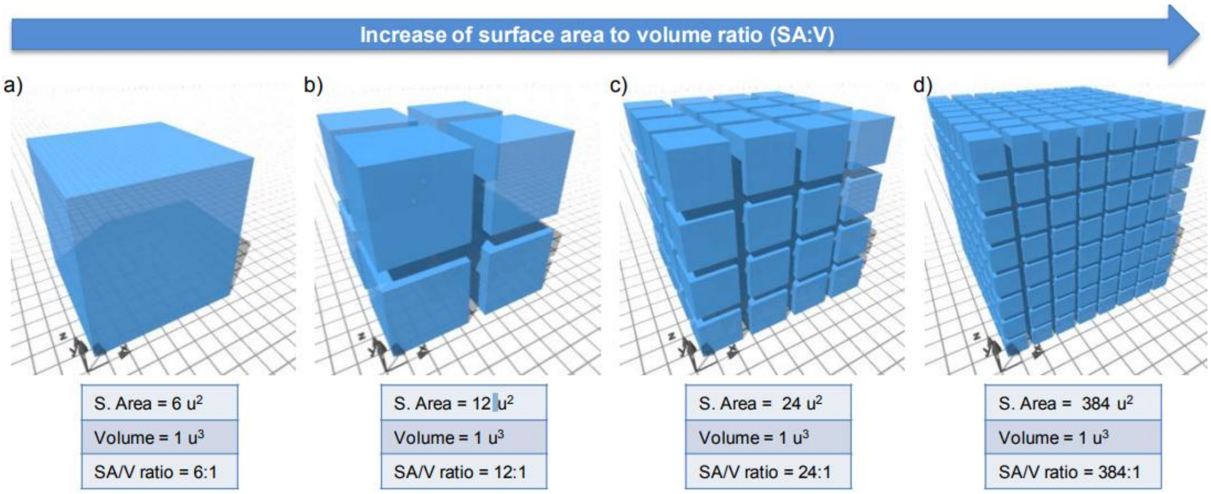

Figure 1.7 Surface area to volume ratio. The increment of surface area vs. volume is graphically represented from the lowest ratio to the highest ratio.[8]

1.3.2 Light trapping effect

The incident light is reflected and refracted when it meets the surface of certain material (i.e. at the interface of two media). When the light is incident to a flat film, the significant portion of light energy cannot be absorbed by the Bragg reflection and transmission. On the other hand, **Figure 1.8** is a sketch showing the heterojunctions of CdS quantum dots attached to the TiO_2 frame structure and the multiple-scattering phenomenon into the patterned nanostructure. The frame structure shows the periodic patterns to get the photonic bandgap property as the photonic crystal structure. Photonic crystals modulate the propagation of the certain wavelength of light. As the result of the multiple-scattering effect, the most energy of incident light can be absorbed by the structure.

In addition, nanostructures can be applied as the anti-reflection layer as shown in **Figure 1.9**. The anti-reflection layer prevents the loss of light energy by the reflection at the surface. Reflectance of incident light from the air to the certain structure can be calculated by the **Equation (1)** with the refractive indices of the two media forming the interface, the air and the structure here.

Equation (1) : $$R = \frac{n_s - n_0^2}{n_s + n_0}$$

Where n_s is the refractive index of structure and n_o is the refractive index of air. Reflectance can be reduced as the difference between two refractive indices becomes smaller. When the layer with a medium refractive index between the air and the titania is formed, the energy of the incident light can be absorbed much more with the reduced reflection.We can combine the two upper phenomena; multiple-scattering into the photonic crystal and anti-reflection effects, to trap the incident light into the strategically designed hybrid structure effectively for the tremendous absorbance of light energy.

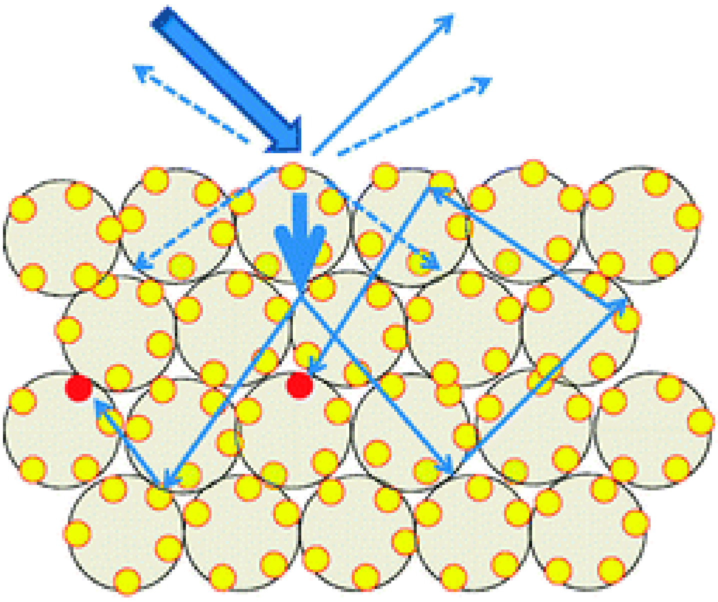

Figure 1.8 Sketch showing the multiple-scattering of incident light into the photonic crystal nanostructure.[9]

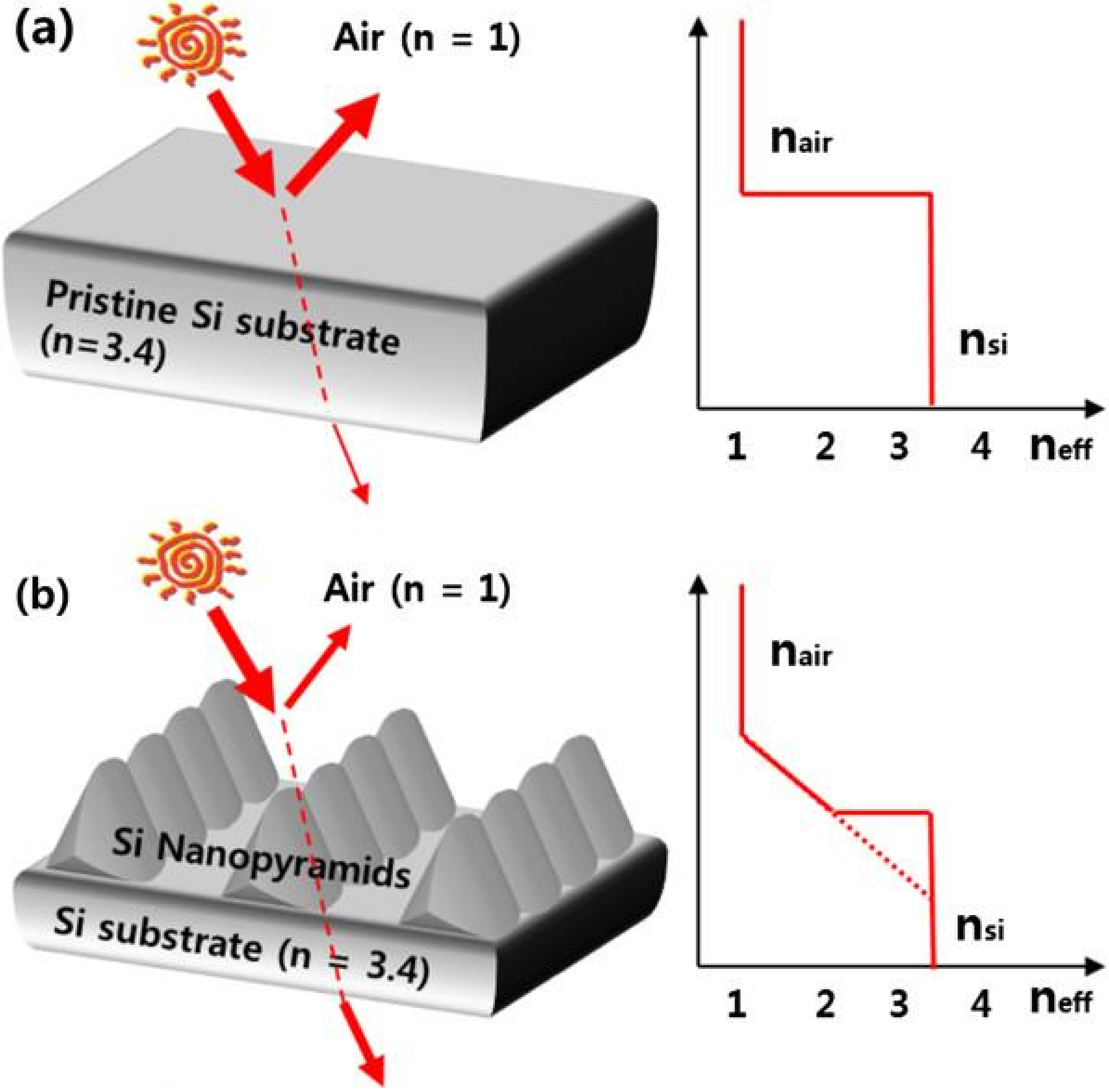

Figure 1.9 Scheme for the effect of the anti-reflective nanostructure.[10]

1.3.3 Plasmonic effect

A plasmon is the concept to explain collective oscillation of free electrons in a metal. For the case of nanoparticles, plasmons exist at the surface with localization. In other words, plasmons take the form of surface plasmons confined to the surfaces of metals and interact strongly with light, resulting in polaritons. It might be called as the localized surface plasmon; collective oscillations of delocalized electrons in response to an external electric field around the metallic nanoparticles that are excited by incident light. Localized surface plasmons enhance the electric field near the surface of the nanoparticles. **Figure 1.10** shows the collective oscillation maximized at the resonance wavelength, which occurs at the visible wavelength region for noble metal nanoparticles such as the gold and silver etc. Such a strong electric field has larger magnitude than one of the incident light, and has the property of an evanescent wave that decreases exponentially as it is far from the interface in the vertical direction. This surface plasmon resonance phenomenon means that light energy is converted into surface plasmon and accumulated on the surface of the metal nanoparticles. As the size of nanoparticles, affected wavelength of the incident light could be changed as shown in **Figure 1.11**. Hot electrons generated at the surface of metal nanoparticles can be transferred to the adjacent semiconductor frame materials over the junction barrier. This light controllable surface plasmon resonance phenomenon can be useful for light trapping effect in various energy devices using solar energy conversion what we will discuss from now on.

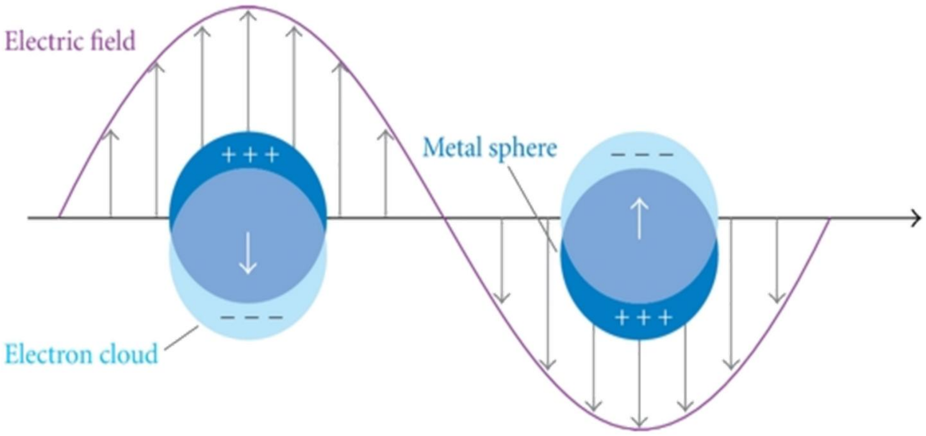

Figure 1.10 Scheme of the localized surface plasmon resonance (LSPR) phenomenon.[11]

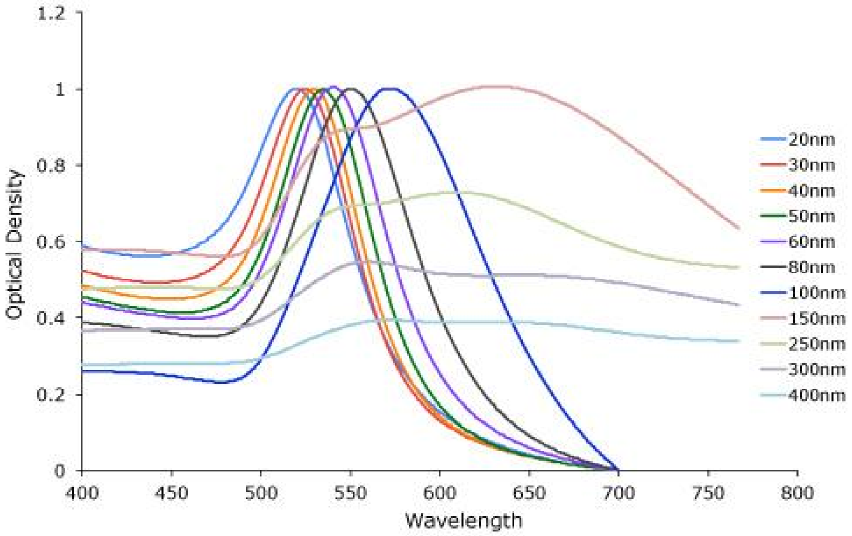

Figure 1.11 The effect of various sized gold nanoparticles for light wavelength.[12]

1.4 Applications of solar energy conversion

Energy is the most important factor as the major driving force for all machinery industry as well as all living things in everyday life. There are numerous energy resources which we are using in the earth such as fossil fuels, nuclear power, renewable energy resources etc. Fossil fuels which occupy the largest portion of the global energy consumption until now have been considered as the most important energy resource after industry revolution generation. However, they cause a serious environmental pollution problem with ill effects on all human beings and eco-system, and depletion of fossil fuel reserves is not the topic of future far from now, due to the dramatic increase of global energy consumption. World power consumption was estimated to be about 17 terawatt in 2015, and the expected power in 2050 is around 30 terawatt.[13-15] Many studies have been reported about the alternative energy solutions instead of fossil fuels which must be able to contribute to this challenge to cause the global scale appreciable impact because the demand for fossil fuels is continuously increasing day by day and finding new oil sources becomes very harder with the soaring prices for the products from crude oil and petroleum.[16, 17] In addition, a lot of social issues were raised such as drastic climate change, environmental degradation, political instability in major oil-producing nations, and need for new more advanced techniques for driving new oil/gas sources etc. The serious reliance on fossil fuels has negative effects of political and socioecological issues in the terms of economic dependence for oil-producing nations.[18]

On the other hand, the renewable energy resources have been utilized with gradually increased dependence with the various critical advantages such as eco-friendly working system and significantly abundant resources etc. The most of renewable energy resources such as the solar energy, wind power, geothermal power, and hydropower etc. generate the main source of energy as the form of electricity and recently, a lot of researches for generation of electricity by the energy conversion and for storage of electricity have been studied to improve the efficiency of energy conversion and to have sufficient energy density and power density owing to greater mass- and charge-transfer properties. Among them, solar energy is the most powerful and semi-permanent renewable and sustainable energy resource. The amount of solar energy reaching the earth for one hour is greater than the global energy consumption for one year.[19] **Figure 1.12** shows the global energy potential of renewable and non-renewable energy resources. The area of the circles is proportional to the amount of supplied energy. Renewable energy sources represent terawatts, and non-renewable energy sources show their potential in terawatt-hour units based on estimated reserves. Global energy consumption in 2013 was 15.97 terawatt, corresponding to 139,891 terawatt-years or 12730.4 Mtoe. For the case of non-renewable resources, if the amount of remaining reserves is exhausted in 30 years, the area of the circle is the amounts we can consume each year. Non-renewable energy sources with limited reserves are nearing depletion issues, and only the wind power and solar energy represent the amount of power that can overcome global energy consumption by themselves in renewable energy sources. Considering the various social situations mentioned above, solar energy is the obvious candidate for the most potential renewable energy resource we can find to alternate fossil fuels. Solar energy can be harvested in various different ways.[20-23] For example, photosynthesis, which plays an important role in all life on the earth, can convert sunlight into chemical energy as the biomass. Biomass can be produced in plants that have low water and fertilizer requirements without any competition for food production. Other resources such as wind power and wave power which are indirectly affected resources from solar energy can also generate electricity, although relatively small amount. This thesis focuses on two methods of using the energy of sunlight. The first one is to use solar energy to break chemical bonds and store energy in a chemical form, which is to split the water by absorbing solar energy, that is, producing the potential hydrogen fuel from water, the richest resource on the earth.[24-26] It is called as the "photoelectrochemical water splitting" for hydrogen generation. The second one, "solar steam generation", is the photothermal conversion form to generate the vapors of freshwater with the desalination of seawater by the thermal evaporating procedures and decontaminate of wastewater.

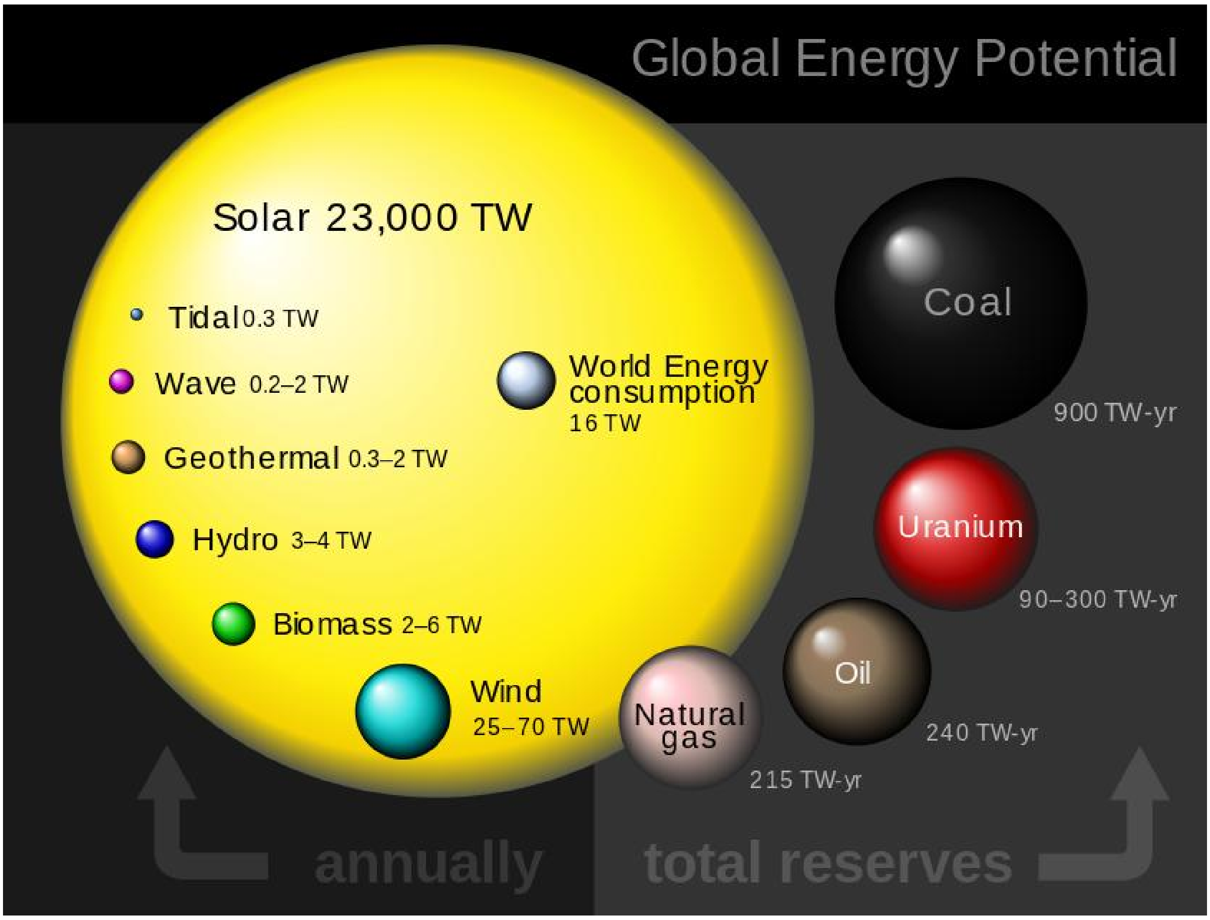

Figure 1.12 The global energy potential comparing energy resources by their potential.[27]

1.4.1 Photoelectrochemical water splitting

Hydrogen fuel is the one of the most effective resources to address global problems related to energy. Unlike fossil fuels, hydrogen fuel reactions don't produce major reasons for greenhouse gases such as carbon monoxide, carbon dioxide, sulfur dioxide, or suspended molecules etc. Hence, the utilization of hydrogen fuels will be increased with the reduction of greenhouse gas emissions so that the environmental health could be improved as well as the air quality. Herman Kuipers, head of exploration research at Royal Dutch Shell, commented on hydrogen fuel: “We are at the peak of the oil age but the beginning of the hydrogen age. Anything else is an interim solution. The transition will be very messy, and will take many technological paths. ... but the future will be hydrogen-fuel cells.” On the earth, there are hydrogen fuels in the form of water as one of the most abundant resources, and hydrogen fuels have the greatest potential in the future.

The characters of Jules Verne's novel “The Mysterious Island”, Cyrus Smith, emphasized the importance of water as a fuel resource through the famous saying, "Water is the coal of the future."[28] Solar energy has enormous capacity to meet present and future global energy demands in an environmentally friendly manner by hydrogen fuel generation from water through efficient conversion to electrical and chemical energy. Many semiconductor materials can be applied as photocatalysts which are energy harvesting systems that efficiently split water under sunlight illumination conditions. In other words, Light in the visible wavelength range which occupies about 50% of the sunlight spectrum has enough energy to split water into hydrogen gas and oxygen gas. Unfortunately, water cannot absorb the light energy to be split by itself without any supporting materials called as photocatalysts. Water splitting can be carried out through the various techniques such as electrolysis, photoelectrolysis, photocatalysis or photoelectrochemical (PEC) and thermochemical reactions, and biophotolysis etc. The semiconductor materials are capable of capturing photons with energy higher than its bandgap energy so that electrons can be excited from the valence band to the conduction band.[29-33] The free energy change for the conversion of one water molecule into hydrogen gas and the half of oxygen gas under standard conditions is $\Delta G = +237.2$ kJ/mol (~4.92 eV), which corresponds to $\Delta E^0 = 1.23$ V per electron transferred according to the Nernst equation. In order to drive this reaction, the photoactive anode material must absorb radiant light to make its electrode potential higher than 1.23 V. If the photoanode material is irradiated by light that has energy greater than the band gap of the photoactive material, then the electrons of the valence band will be excited into the conduction band while the holes remain in the valence band.[34] **Figure 1.13** shows the hydrogen evolution reaction (HER) and oxygen evolution reaction (OER) using electrons/holes generated under illumination. **Figure 1.14** shows the band-edge positions of conduction and valence band versus the normal hydrogen electrode (NHE) for various p-type and n-type semiconductors used in PEC water splitting system. Several the n-type semiconductors which have large band gap energy (such as TiO_2) are placed around the O_2/H_2O reduction potential, but they cannot show the high photocurrent densities. On the other hand, the p-type semiconductor materials which have the smaller bandgap energies place their conduction/valence bands more negatively so that the reactions at the H^+/H_2 potentials are well suitable. The over-potentials which are required for water oxidation and reduction are the very important factor for the alignment of the conduction and valence band-edges to be suitable to potentials of OER and HER respectively. For example, water splitting can be negligible or very slow when the valence band potential doesn't be placed sufficiently positive for water oxidation or the conduction band potential doesn't be placed sufficiently negative for proton reduction.

In this way, the charge carriers generated by the sunlight can participate in reactions in which water is reduced and oxidized to hydrogen and oxygen, respectively PEC systems should be operated with highly competitive in cost and great solar-to-chemical conversion efficiency for a long operating period to satisfy the goals to be an ideal fuel. Numerous approaches which are applied to a lot of semiconductor materials have improved to several properties, but they cannot still successfully satisfy the standard of performance, design, cost, and stability. Therefore, an ideal photocatalyst is still one of the remaining challenges in the chemical industry for effective hydrogen fuel generation. However, insufficient mobility of charge carriers and narrow absorption range of photocatalysts could reduce the efficiency of solar energy conversion systems.

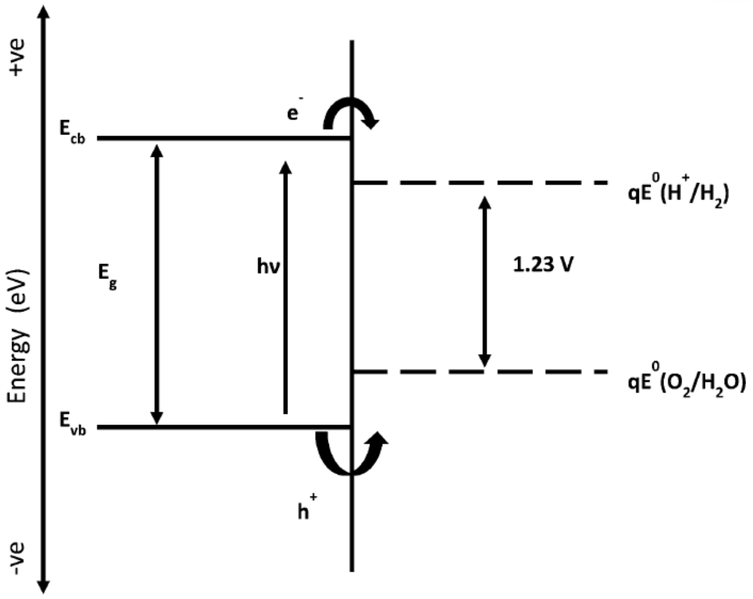

Figure 1.13 Oxygen evolution reaction (OER) and hydrogen evolution reaction (HER) for overall water splitting.[24]

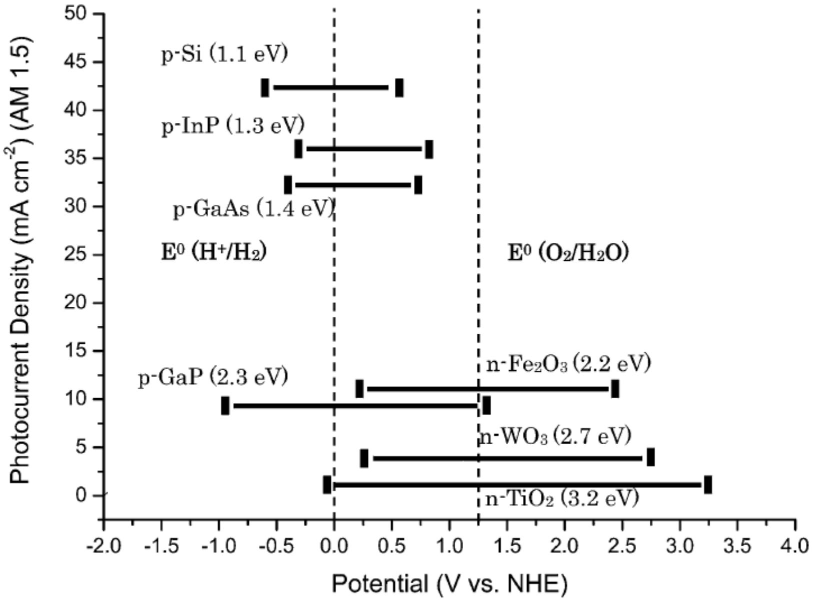

Figure 1.14 Conduction band and valence band positions vs. NHE of common semiconductors used in photoelectrolysis cells.[24]

As shown in **Figure 1.15**, schematic energy diagram indicates the basic principles in a photoelectrochemical water splitting cell using a photoactive semiconductor material as a photoanode for the OER and a counter metal electrode as a cathode for the HER. There are several main steps such as the light absorption, charge transport, and surface chemical reactions. Light energy of incident photons greater than the band gap energy of photoactive semiconductor materials can be absorbed with an efficiency of light absorption. The electric field separates electrons to the cathode along the charge collector and an external circuit, and holes to interface of electrolyte, respectively. Charge transport means the ratio for the photo-generated electron/hole pairs to success reaching the respective interfaces of photoanode at the opposite sides each other. Holes are transferred toward the electrolyte to take part in the OER. Electrons are transferred to the cathode through the external circuit so that they take part in the HER. An electrochemical equipment supports the water splitting by applying an external potential that can provide additional driving force to the charge carriers.

$$\mathrm{H_2O + 2\ h^+ \rightarrow \frac{1}{2}\ O_2\ +\ 2\ H^+}\quad \text{(OER by oxidation)}$$

$$\mathrm{2\ H^+ +\ 2\ e^- \rightarrow H_2}\quad \text{(HER by reduction)}$$

$$\mathrm{H_2O \rightarrow \frac{1}{2}\ O_2 +\ H_2}\quad \text{(Total water splitting reaction)}$$

To perform those reactions, generated electrons and holes by light energy absorption in the semiconductor material electrode must be transported without recombination to the interfaces. The energy required for water splitting photoelectrochemically at a semiconductor photoelectrode with consideration of losses due to the concentration and kinetic over-potentials is frequently reported as about 2 eV per electron–hole pair generated.[35, 36] As the result, four electron–hole pairs must be generated in a photo-induced process for OER at the photoanode.

The incident photon-to-current conversion efficiency (IPCE) of photoanode can be calculated by

$$\mathrm{IPCE\ (\%)} = \frac{1240\ \times\ J}{\lambda\ \times I}\ \times 100\ \%$$

where J represents the photocurrent density (mA/cm^2), λ is the wavelength of incident light (nm), and I is the intensity of incident light (mW/cm^2).

Then, the overall solar energy conversion efficiency can be calculated by

$$\eta\ (\%) = \frac{J \times (E^0_{\mathrm{rex}} - E)}{I} \times 100\ \%$$

where E is the bias voltage applied against the counter electrode (= 0 V for the photoanode) and E^0_{rex} is usually 1.23 V (pH = 0) for the reactions of water splitting.

As the result of previous calculations, the solar-to-hydrogen efficiency for a photoelectrochemical water splitting system can be expressed as

$$\eta\ (\%) = \frac{J \times 1.23}{I_{\mathrm{light}}} \times 100\ \%$$

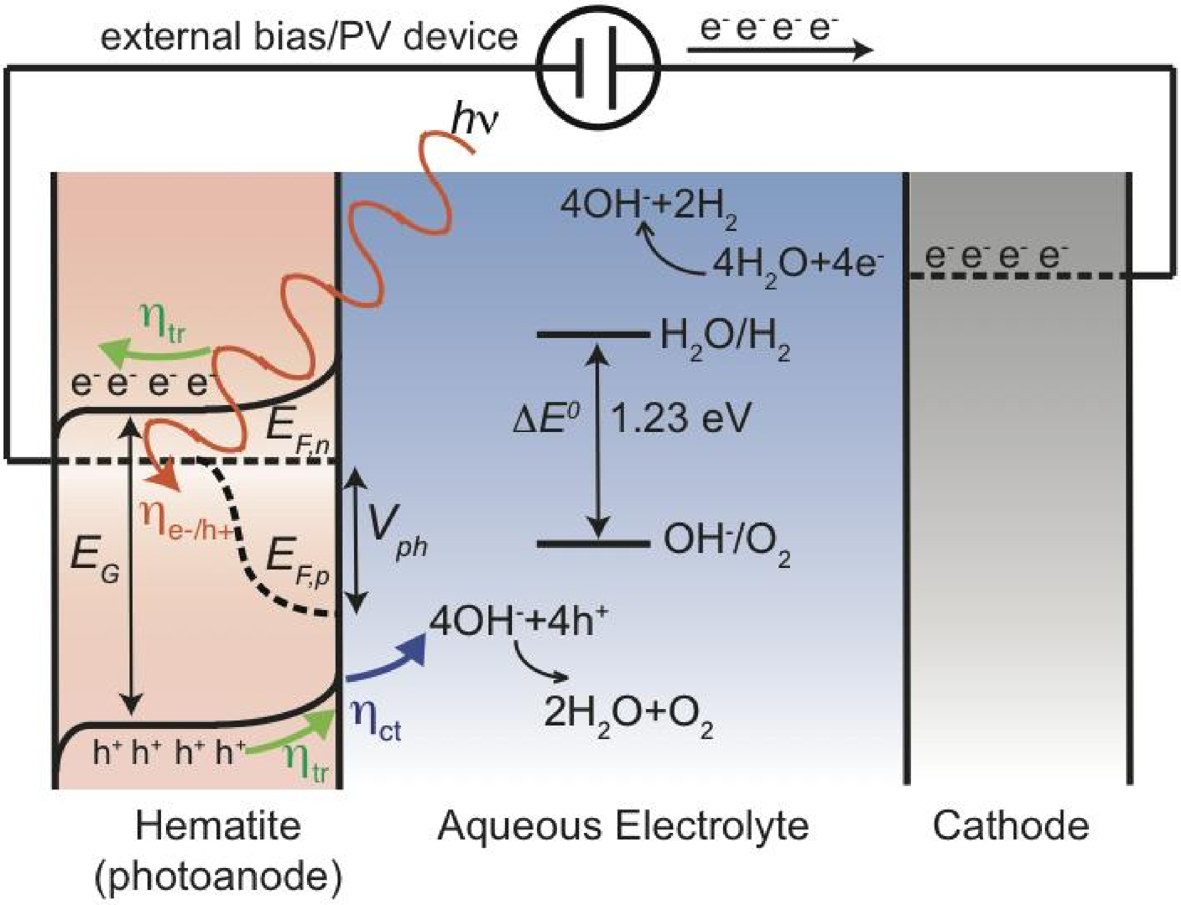

Figure 1.15 A schematic energy diagram for a photoanode (n-type semiconductor).[37]

Here, there are the several criteria that an ideal photoanode material should have. First, as I already mentioned before, with respect to efficiencies of processes with energy losses, a more practical bandgap energy is about 2 eV (the bandgap energy must be greater than 1.23 eV). The photoanode can be working by the energy from the visible light and shorter ultraviolet wavelength which occupy about 55% of incident sunlight spectrum. Second, band-edges should be placed for bandgap to cover the reduction potentials of water splitting reactions. Third, the mobility and lifetime of electron-hole should be secured sufficiently to allow reaching to the active sites, because the materials with few defects and small size of particles inhibit recombination of generated electron-hole pairs. Fourth, the OER rate must be dramatically greater than the one of recombination. Finally, the materials have to be stable chemically in an aqueous solution and under illuminating conditions to prevent itself being oxidized by photogenerated holes instead of water. However, there is the quite large difference of performances between an actual and an ideal photoanode as shown in **Figure 1.16**. There are three main factors limiting performance as the increase to anodic potential such as generation of electron/hole pairs by light absorption of semiconductor material, charge transfer within photoanode and at the photoanode/electrolyte interface.

As discussed above, many semiconductor materials can be used as electrode materials which can absorb the sunlight of ultraviolet and visible wavelength for water splitting. To improve the performance for the efficient solar light energy conversion, two of mainly studied approaches recently such as the improvement of the light absorbance and the charge-transfer in photoelectrochemical water splitting system. In this regard, strategically designed nanostructures should be introduced as promising materials. Nanometer-scale designed structures have many interesting properties compared with corresponding bulk materials such as the excellent surface to volume ratio and light trapping effect *etc*. Recently, nano-structured photoelectrode materials are very attractive and considerable attention in the development of the photoelectrochemical water splitting system. **Figure 1.17** shows various approaches to satisfy the demands of the photoelectrochemical water splitting in nanotechnology field.

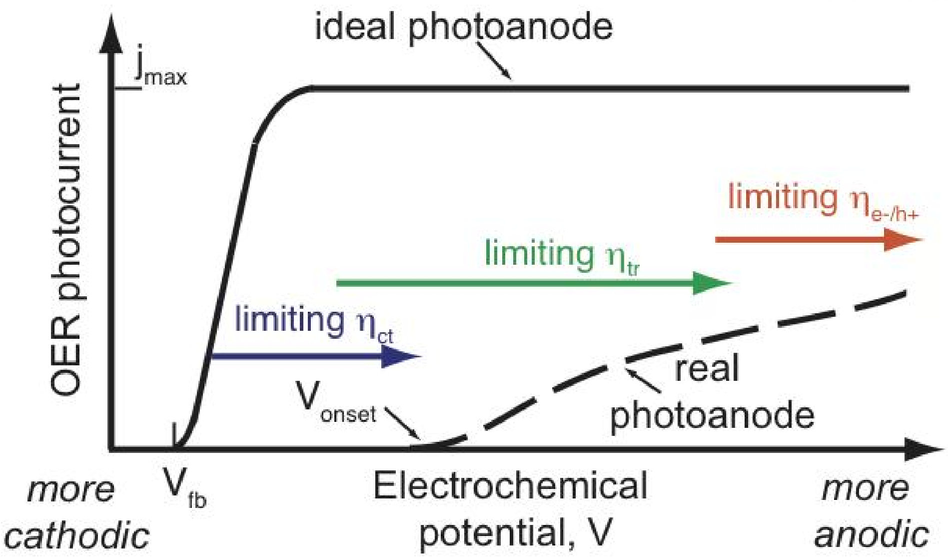

Figure 1.16 PEC performance gap between a state-of-the-art photoanode and the ideal photoanode.[37]

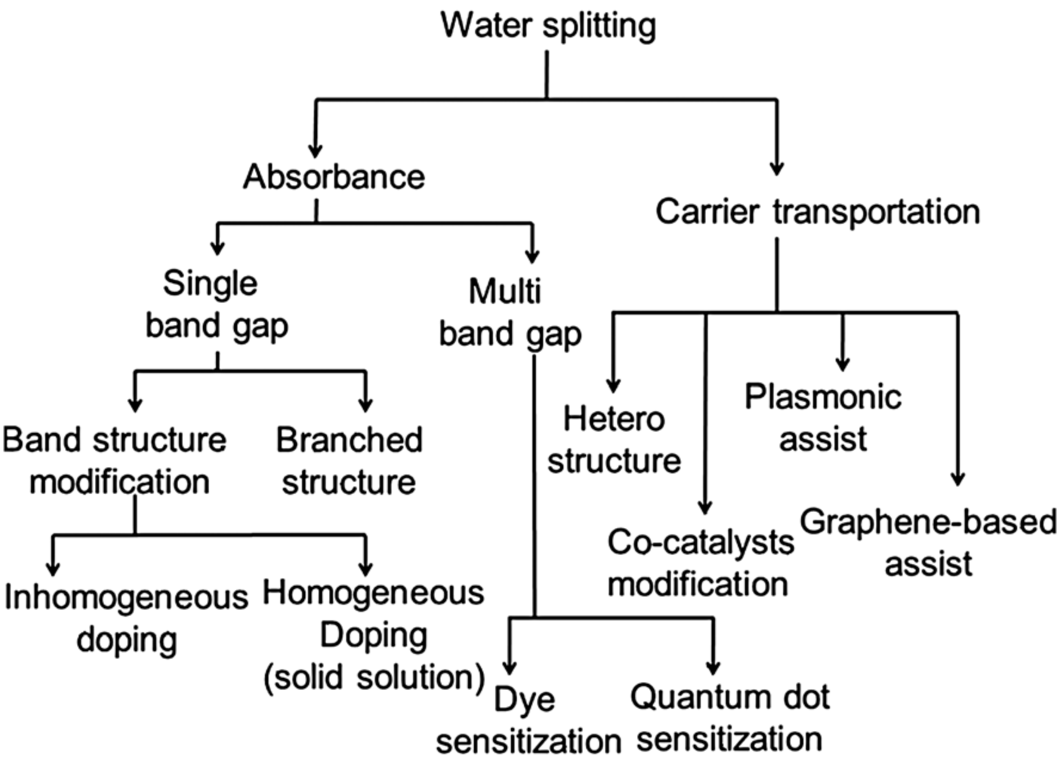

Figure 1.17 Scheme of various approaches to improve the water splitting performance.[38]

1.4.2 Solar steam generation

The combination of solar energy and water has been very attractive in a slightly different studies recently. Solar steam generation is one of the most important fields in the global modern society due to the applicable devices in the broad range such as power generation, seawater desalination systems, decontamination of wastewater and sterilization systems.[39–42] Solar steam generation techniques which have been carried out until now depends on the surface of photoabsorber to absorb sunlight energy, and convert the solar energy to heat as followed by the efficient transferring the accumulated heat to the bulk seawater directly or through the intermediate transfer media to produce vapors by evaporation.[43, 44] The devices require a high concentration of generated heat to overcome the high loss of light energy and heat at the surface. For the design, the photothermal system must be added complexity with high cost. Therefore, high efficient photothermal conversion system with competitive cost and strategic designs reducing energy loss should be developed for the solar steam generation. Recently, nano-structured photothermal systems have been widely studied with the absorption of light energy over a broadband wavelength of sunlight spectrum as low cost and promising approaches. At the beginning of the research of this field, nanoparticles minimize their surface energy loss as the volumetric absorbers by constant temperature in the fluid so that thermal conductivity can be improved such as the dispersed gold nanoparticles in a bulk seawater achieve a solar-thermal-conversion efficiency of about 24%.[45–47] Nevertheless, the significant portion of light energy cannot be absorbed by the high scattering, and the heat generated by the conversion of the absorbed light energy cannot be concentrated. The efficiency of solar steam generation by the evaporation indicates considerably lower value through the conductive loss of the whole bulk solution.[48] To address this issue, floating film type devices have been suggested to localize the generated heat by the photoabsorber materials onto air/solution interface such as paper, carbon foams, anodic aluminum oxides, and cellulose membranes *etc*.[49–54] Thermal insulators were additionally introduced between photoabsorber and bulk solution to perform the thermal localization much efficiently at the interface and to minimize the conductive heat loss to the bulk solution, which could be effectively accomplished through the cooperation of water transport by the capillary force.[55-58] **Figure 1.18** shows the schematic illustration to explain working procedures of solar steam generation in the film type floating devices. At first, solar light energy was harvested by the photoabsorber which could be micro-structured for the light trapping effect, and then converted into heat to evaporate the water at interface. The thermal insulation layer is made by the materials which have a low thermal conductivity to localize generated heat at the interface. Also, it must have the water transporting channels which work through the capillary force as shown in the figure. Photoabsorbers have been usually studied using various carbon-based black materials, noble metal nanoparticles to occur plasmonic effect and nano-structured semiconductors for efficient absorption over a broadband wavelength of whole sunlight spectrum.

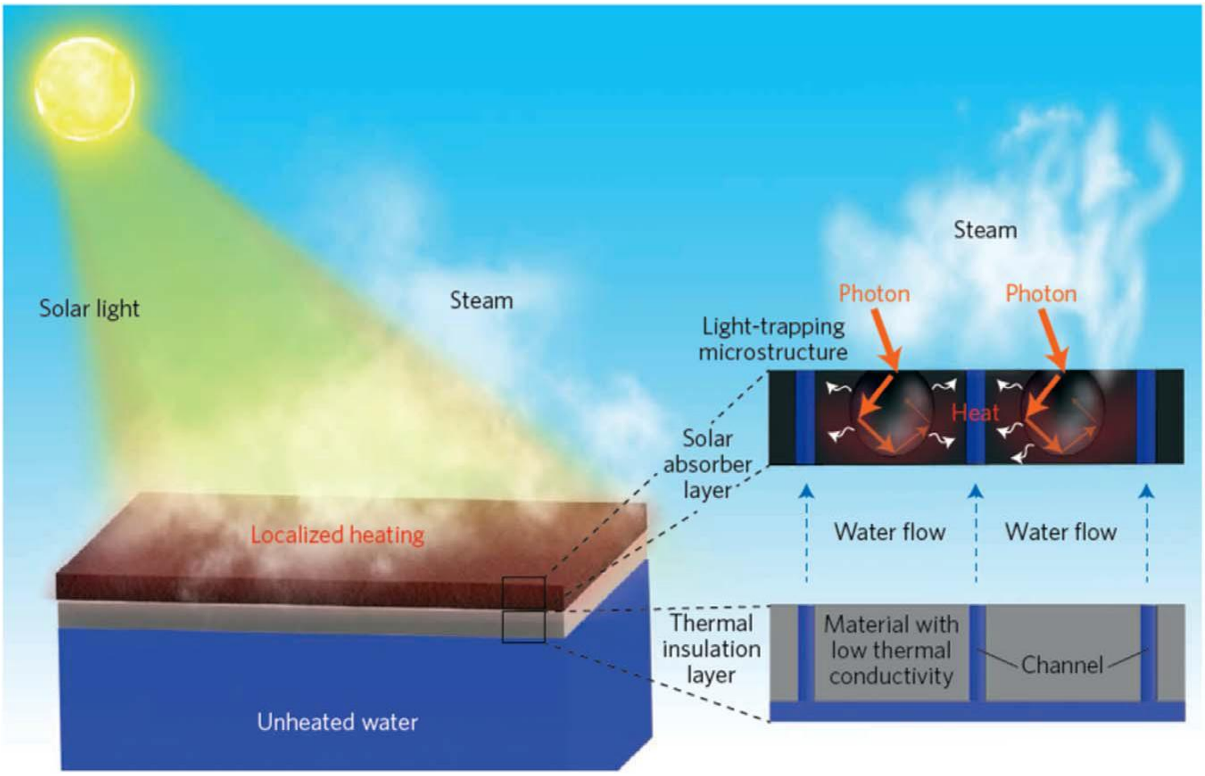

Figure 1.18 Scheme of the photothermal film type device floating at air-water interface.[55]

Representative materials for the candidates of photoabsorbers is divided by mainly three types such as carbon-based black materials, metals which can occur plasmonic effect, and semiconductor materials. At first, amorphous carbon doesn't have crystallinity in a large range and it usually contains hydrogen and nitrogen. It has very high light absorption properties to the broadband wavelength of light with the composition of a mixed sp^2 and sp^3 bondings due to dense energy levels of the relatively free π electrons. Moreover, excellent stability secured by the aromatic functional groups makes the materials inactive at atmospheric temperatures and insoluble in aqueous solutions and other organic solvents.[59] Conventional carbon-based materials with the π-band can absorb the visible wavelength of sunlight due to optical transitions. However, a moderate reflection of about 10% at the interface with air limits absorption of light energy.[60] To overcome the limit, there are various approaches using strategically designed nanostructures, such as vertically aligned carbon nanotubes and porous graphene *etc*.[61–65] In this way, a large number of microscaled cavities are formed for light trapping effect, which confine light into the structures that enhance the absorption of light energy significantly by the lengthened pathway of multiple light scattering.[66] **Figure 1.19** shows the structural design of carbon-based double layer for heat localization with the steam generating performance and photothermal efficiency. *Chen et al*. reported double-layered structure which consists of the exfoliated graphite and carbon foam as a photoabsorber at the top and thermal insulator, respectively. The exfoliated graphite layer forms a high-temperature region at the top of the double-layer structure, and the solution transported through the carbon foam is evaporated at the high-temperature region to release into the air. Due to the insulating effect of the carbon foam, the device of double-layer structure records the highest evaporation rate as much as 2.4 times higher than pure water and it is corresponding to about 85% of solar-thermal efficiency under 10 sun illumination condition.

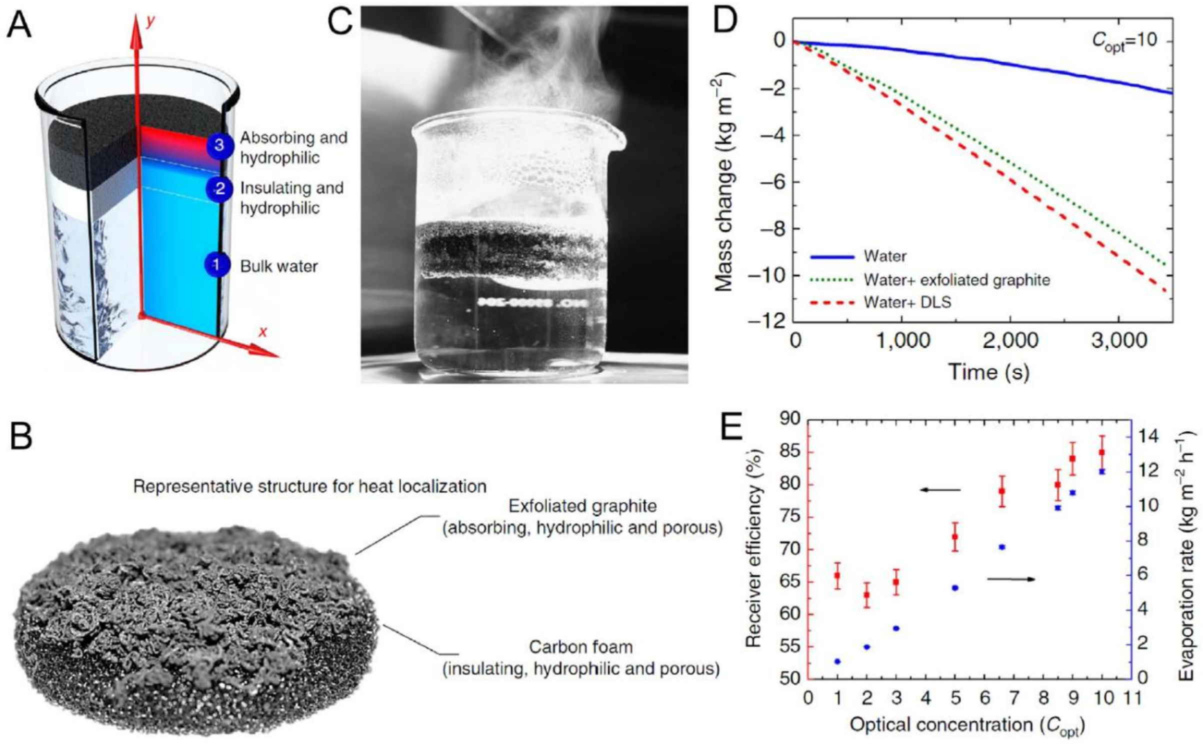

Figure 1.19 (A) Scheme of the cross section of a double-layered solar steam generation device and temperature distribution. (B) The double-layer structure that consists of the exfoliated graphite layer onto the carbon foam. (C) A real image of steam generation under 10 sun illumination. (D) Steam generation induced mass change performances. (E) Solar thermal efficiency and the evaporation rates as the different optical concentration conditions.[67]

Second method for the photothermal conversion is utilization of plasmon resonance which is a unique optical phenomenon of metal nanostructures. When the frequency of electrons' oscillation is well-matched with the one of incident light, the excitation of the electrons is caused collectively with the coherent oscillation for the incident electromagnetic field. Therefore, in case of heat generation by plasmon resonance effect of metal nanoparticles, many electrons make the heat conversion very strong by following the Joule mechanism.[68–70] By the scattering of electrons, the hot carriers redistribute their energy so that the plasmonic element is the remarkably heated. Then, the generated heat is further transferred to surrounding environment by the conduction.[71]

Due to its very fragile durability, the metal nanostructures for plasmon resonance need the supporting layers such as the paper-supported films[53,72,73], anodized aluminum oxide membranes[74] and filter papers[75] etc. Gold decorated airlaid paper was reported as the photoabsorber onto the supporting layer which can also serve as a thermal insulating. (**Figure 1.20**)[53] The airlaid paper supporting layer can make the light absorption increase with the multiple scattering of incident light by the increased surface roughness, and can transport the solution by the strong capillary flow of the microscale pores within the structure for the sufficient replenishment of interfacial evaporation. The gold-deposited airlaid paper device generates localized heat only at the surface of solution while bulk solution still remains at the relatively lower temperature. Effective steam generation under 4.5 sun illumination condition is well-shown compared with control samples and the photothermal conversion efficiency is about the 78% while the efficiency of the pristine gold film is just 45%. In addition, the critical advantage of this plasmonic heat conversion is the reliable stability during the recycles by multiple times.

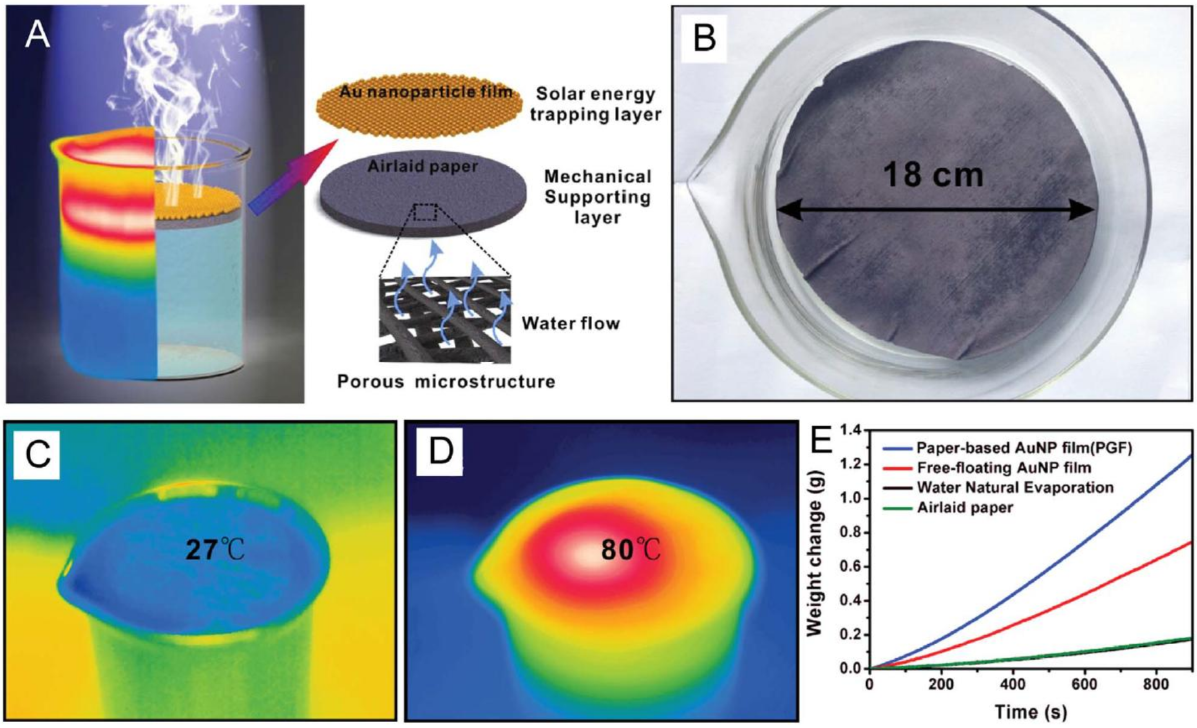

Figure 1.20 (A) Scheme of the airlaid paper-based gold nanoparticle film (PGF). (B) A top view real image of PGF. (C) The thermographic images of PGF before solar illumination. (D) The temperature distribution at the surface of PGF. (E) Steam generation induced weight changes under 4.5 sun illumination condition.[53]

Black semiconductors are studied as the photoabsorber materials due to their various advantages such as low cytotoxicity and competitive cost.[54, 76–79] Heat dissipation by the semiconductor photoabsorbers is performed by the excitation and relaxation process of photo-generated electron/hole pairs. The most photons with the higher energy than the bandgap of semiconductors can lead to the excitation of electrons above the conduction band edge. The electrons and holes generated through the photon energy absorption relax to the edges of the conduction band and valence band respectively to convert from the energy of relaxation process in form of heat. The effect of this mechanism is remarkably decreased for the semiconductor materials with broad bandgap energy in which significantly lower portion of the absorbed light energy in the generated electron/hole pairs dissipate heat at the relaxation process. Photoabsorber materials should have a high capability of light absorption and less emissivity to ensure the high photothermal conversion efficiency. They should have the competitive cost of the abundant element for the mass-production in the industrial fields. In terms of this points, titanium oxide is one of very proper materials due to the low cost, high light absorption, and very good thermal stability *etc*.[80] The most popular titanium dioxide has a very large bandgap energy (about 3.2 eV), however, a black titania made by the self-structural modification methods such as the self-doped Ti^{3+}/oxygen vacancy, or incorporation of hydrogen doping *etc*. was reported to have narrow bandgap (about 1.5 eV) which can absorb overall sunlight spectrum from 2011.[81] TiO_x ($x<2$) with color tunable from white to black can be synthesized by the reduction procedure using a magnesium to the commercial P25.[76] The increase of magnesium reduces the contents of oxygen of TiO_x with the decrease of x value, which means the improvement of light absorption. TiO_x synthesized in this way was spin-coated on the surface of a stainless steel mesh after the surface super-hydrophobization step to confirm its performance as a photoabsorber material, resulting in a 50% of photothermal efficiency under 1 sun illumination. In addition, black titania with a unique nanocage structure which can cause the light trapping effect was also reported and it shows the improvement of photothermal efficiency up to about 71%.[82]

Figure 1.21 shows the Ti_2O_3 nanoparticles deposited cellulose membranes for efficient solar steam generation. The much narrow bandgap and nanoscaled particles enable very high light energy absorption in full spectrum range, resulting in about 92.5% of absorption capacity, greater than most photoabsorber materials. Solar steam generation rate is 1.32 kg/m^2h under 1 illumination, which is 2.65 times higher than the pure water.

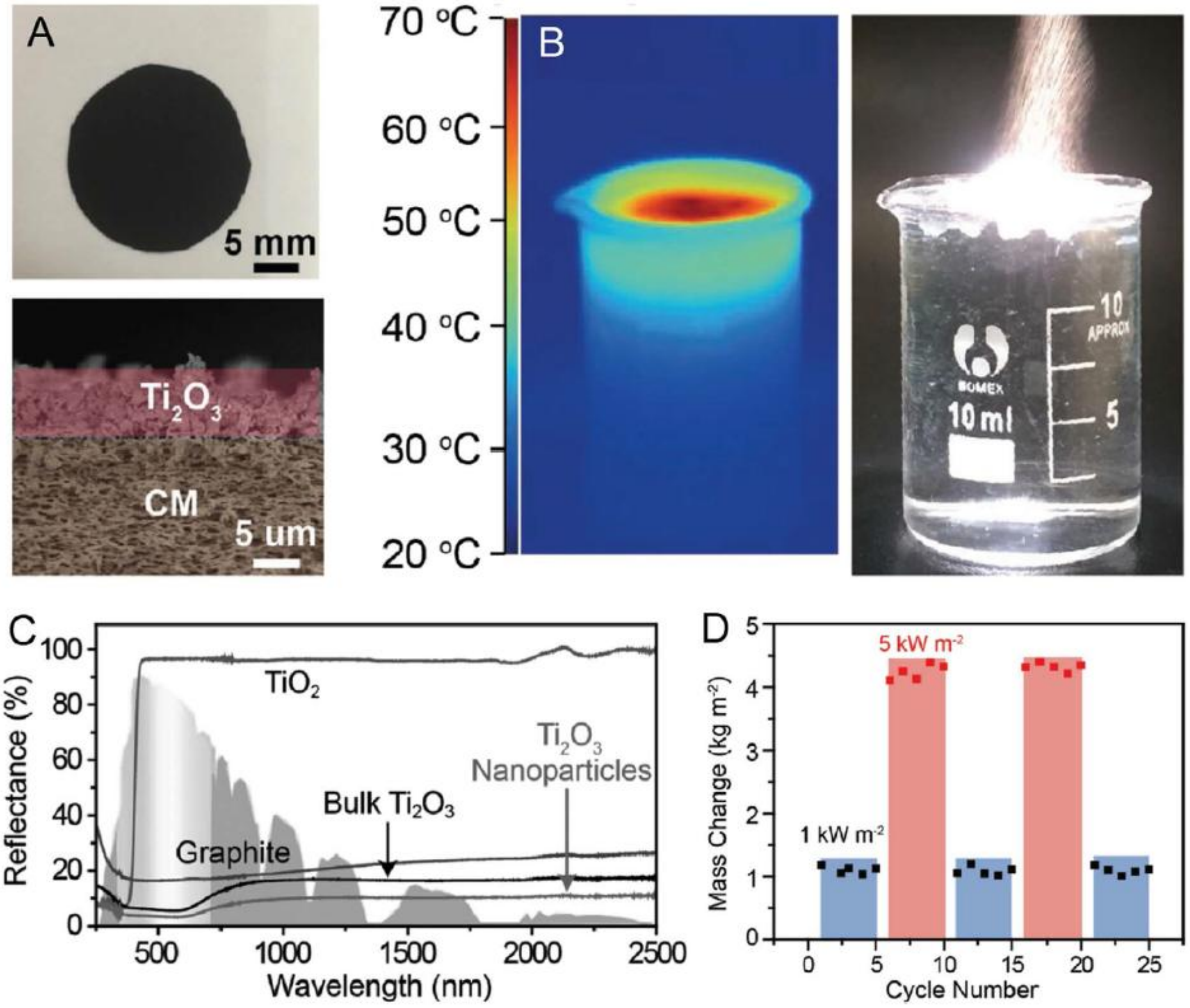

Figure 1.21 (A) A real image and SEM cross-section image of the Ti_2O_3 nanoparticle loaded cellulose membrane. (B) Thermographic image and the real image of the solar steam generation under 7 sun illumination condition. (C) Diffuse reflectance spectra analysis. (D) Evaporation cycle performance under different intensities of illuminated sunlight.

1.5 References

1. N. Pradhan, *et al.*, *BioMed Research International*, **2015**, 2015, 365672.
2. GENNESYS White paper, Max Planck Institute for Intelligent Systems, **2010**.
3. H. Cui, *et al.*, *Science*, **2007**, 317, 647-650.
4. G. Zhang and D. Wang, *Chemistry an Asian Journal*, **2009**, 4, 236-245.
5. A. Pimpin and W. Srituravanich, *Engineering Journal*, **2012**, 16, 37-55.
6. S. Jeon, *et al.*, *Proceedings of the National Academy of Sciences of the United States of America*, **2004**, 101, 12428-12433.
7. J. H. Moon and S. Yang, *Chemical Review*, **2010**, 110, 547-574.
8. L. Portilla, *Ph.D. Thesis in Soochow University*, **2017**.
9. M. E. Harakeh and L. Halaoui, *Journal of Physical Chemistry C*, **2010**, 114, 2806-2813.
10. J. M. Ha, *et al.*, *Nanoscale Research Letters*, **2014**, 9, 9.
11. Y. Hong, *et al.*, *Journal of Nanomaterials*, **2012**, 2012, 759830.
12. W. Kim and J. Park, *News & Information for Chemical Engineers*, **2014**, 32, 2, 173.
13. Statistical Review of World Energy, *BP*, **2016**, http://www.bp.com/en/global/corporate/energy-economics/statistical-review-of-world-energy.html.
14. P. Gerland, *et al.*, *Science,* **2014**, 346, 234–237.
15. G. A. Jones and K. J. Warner, *Energy Policy*, **2016**, 93, 206–212.
16. P. C. K. Vesborg and T. F. Jaramillo, *RCS Advances*, **2012**, 2, 7933–7947.
17. Z. W. Seh, *et al.*, *Science*, **2017**, 355, 6321, eaad4998.
18. N. Chouhan, *et al.*, *Electrochemical Technologies for Energy Storage and Conversion*, **2012**, 1, 12, 541-599.
19. K. Rajeshwar, *et al.*, *Springer*, **2008**.
20. J. A. Herron, *et al.*, *Energy & Environmental Science*, **2015**, 8, 126-157.
21. C. Acar, *et al.*, *International Journal of Energy Research*, **2016**, 40, 1449–1473.
22. H. Junge, *et al.*, *Inorganics*, **2017**, 5, 14.
23. L. Dura, *et al.*, *Inorganics*, **2017**, 5, 21.
24. M. G. Walter, *et al.*, *Chemical Reviews*, **2010**, 110, 6446–6473.
25. B. A. Pinaud, *et al*. *Energy & Environmental Science*, **2013**, 6, 1983–2002.
26. T. Jafari, *et al.*, *Molecules*, **2016**, 21, 900.
27. R. Perez and M. Perez, *Global energy potential*, **2009**.
28. J. Verne, *Pierre-Jules Hetzel*, **1874**.
29. Y. R. M. Navarro, *et al.*, *Chem. Sus. Chem.*, **2009**, 2, 471–485.
30. J. Xing, *et al.*, *Chemistry - An Asian Journal*, **2012**, 7, 642–657.
31. F. E. Osterloh, *Chemical Society Reviews*, **2013**, 42, 2294–2320.
32. J. Ran, *et al.*, *Chemical Society Reviews*, **2014**, 43, 7787–7812.
33. T. Hisatomi, *et al.*, *Chemical Society Reviews*, **2014**, 43, 7520–7535.
34. M. D. Bhatt and J. S. Lee, *Journal of Materials Chemistry A*, **2015**, 3, 10632-10659.
35. J. A. Turner, *Science*, **1999**, 285, 1493.
36. J. R. Bolton, *et al.*, *Nature*, **1985**, 316, 495.
37. B. Iandolo, *et al.*, *Journal of Materials Chemistry A*, **2015**, 3, 16896–16912.

38. H. M. Chen, *et al.*, *Chemical Society Reviews*, **2012**, 41, 5654–5671.
39. M.A. Shannon, *et al.*, *Nature*, **2008** 452, 301–310.
40. M. Elimelech, W.A. Phillip, *Science*, **2011**, 333, 712–717.
41. O. Neumann, *et al.*, *Proceedings of the National Academy of Sciences of the United States of America*, **2013**, 110, 11677–11681.
42. M. Thirugnanasambandam, *et al.*, *Renewable & Sustainable Energy Reviews*, **2010**, 14, 312–322.
43. M. J. Montes, *et al.*, *Solar Energy*, 2009, 83, 679–689.
44. S. Al-Kharabsheh, D.Y. Goswami, *Solar Energy*, **2003**, 75, 395–401.
45. O. Neumann, *et al.*, *ACS Nano*, **2013**, 7, 42–49.
46. H.H. Richardson, *et al.*, *Nano Letters*, **2009**, 9, 1139–1146.
47. M. Gao, *et al.*, *Energy & Environmental Science*, **2016**, 9, 3151–3160.
48. N.J. Hogan, *et al.*, *Nano Letters*, **2014**, 14, 4640–4645.
49. J. Zhou, *et al.*, *Advanced Functional Materials*, **2016**, 26, 5368–5375.
50. X. Li, *et al.*, *Proceedings of the National Academy of Sciences of the United States of America*, **2016**, 113, 13953–13958.
51. Y. Li, *et al.*, *Advanced Materials*, **2017**, 1700981.
52. L. Zhou, *et al.*, *Nature Photonics*, **2016**, 10, 393–398.
53. Y. Liu, *et al.*, *Advanced Materials*, **2015**, 27, 2768–2774.
54. J. Wang, *et al.*, *Advanced Materials*, **2017**, 29, 1603730.
55. W. Shang and T. Deng, *Nature Energy*, **2016**, 1, 16133.
56. L. Shi, *et al.*, *Journal of Materials Chemistry A*, **2017**, 5, 16212–16219.
57. X. Hu, *et al.*, *Advanced Materials*, **2017**, 29, 1604031.
58. F.M. Canbazoglu, *et al.*, *AIP Advances*, **2016**, 6, 085218.
59. Q. Zhao, *et al.*, *Carbon*, **2011**, 49, 877–883.
60. E.A. Taft and H.R. Philipp, *Physical Review*, **1965**, 138, A197–A202.
61. F.J. García-Vidal, *et al.*, *Physical Review letters*, **1997**, 78, 4289–4292.
62. K. Mizuno, *et al.*, *Proceedings of the National Academy of Sciences of the United States of America*, **2009**, 106, 6044–6047.
63. S. Thongrattanasiri, *et al.*, *Physical Review letters*, **2012**, 108, 047401.
64. A.M. Kolpak and J.C. Grossman, *Nano Letters*, **2011**, 11, 3156–3162.
65. A.V. Dudchenko, *et al.*, *Nature Nanotechnology*, **2017**, 12, 557–563.
66. X. Zheng and L. Zhang, *Energy & Environmental Science*, **2016**, 9, 2511–2532.
67. H. Ghasemi, *et al.*, *Nature Communications*, **2014**, 5, 4449.
68. M.L. Brongersma, *et al.*, *Nature Nanotechnology*, **2015**, 10, 25–34.
69. G. Liu, *et al.*, *Journal of Materials Chemistry A*, **2017**, 5 (2017) 4233–4253.
70. T. Liu and Y. Li, *Nature Photonics*, **2016**, 10, 361–362.
71. C. Jia, *et al.*, *Advanced Energy Materials*, **2016**, 6, 1600431.
72. X. Wang, *et al.*, *Applied Energy*, **2017**, 195, 414–425.
73. C. Chang, *et al.*, *ACS Applied Materials & Interfaces*, **2016**, 8, 23412–23418.
74. S. Yu, *et al.*, *Scientific Reports*, **2015**, 5, 13600.
75. C. Liu, *et al.*, *Advanced Sustainable Systems*, **2017**, 1, 1600013.

76. M. Ye, *et al*., *Advanced Energy Materials*, **2017**, 7, 1601811.
77. C. Zhang, *et al*., *Small*, **2016**, 12, 5320–5328.
78. L. Zhang, *et al*., *Advanced Materials*, **2015**, 27, 4889–4894.
79. Q. Tian, *et al*., *ACS Nano*, **2011**, 5, 9761–9771.
80. G. Liu, *et al*., *Solar Energy Materials and Solar Cells*, **2012**, 98, 24–38.
81. X. Chen, *et al*., *Science*, **2011**, 331, 746–750.
82. G. Zhu, *et al*., *ACS Applied Materials & Interfaces*, **2016**, 8, 31716–31721.

Chapter 2

Photoelectrochemical Water Splitting

2.1 Optimization for visible light Photoelectrochemical water splitting: gold-coated and surface-textured TiO_2 inverse opal nano-networks

Adapted with permission from ref. 60. Copyright 2013 Royal Society of Chemistry

2.1.1 Introduction

The conversion of solar energy to hydrogen by a water splitting process is an attractive approach to achieve clean and renewable energy systems. Photoelectrochemical (PEC) water splitting is a chemical process of electrolysis of water by sunlight generating hydrogen.[1] The PEC cells are typically designed with metal oxide semiconductors that operate at particular wavelengths of light/energies as photoelectrodes and noble metals as counter electrodes.[2] Among the metal oxide semiconductors being intensively investigated (e.g., TiO_2[3, 4], ZnO[5, 6], Fe_2O_3[7, 8], WO_3[9, 10], and Cu_2O[11, 12]), TiO_2 is very promising since it has flat band potential, fast electron pathways, photo-chemical stability, and good corrosion resistance in aqueous solutions.[13] However, TiO_2 has a large bandgap, which results in a limited photoresponse and overall low efficiency in the visible region. A strategy for bandgap engineering of TiO_2 , such as fabrication of an array of nanowires[14, 15] or nanotubes,[16-18] doping of heteroatoms,[17-19] and coating of quantum dots,[20-23] is thus necessary for efficient hydrogen generation. Metal/semi-conductor contacts have shown a great interfacial charge transfer mechanism such as hot electron injection and plasmon resonance energy transfer (PRET).[24-26] For example, a metallic nanostructure can enhance optical absorption in the range of visible light through excitation of the surface plasmons, resulting in excitation of electrons in the semiconductor at energies well below the semiconductor’s bandgap; this in turn allows for a predominance of electrons in the conduction band of a semiconductor. Light absorption is an important issue for active materials in these systems because utilization of maximal absorption of light is strongly correlated with conversion efficiency of photons to electrons.[27] It has been reported that metal NPs can exhibit outstanding absorption via scattering when the size is comparable to or larger than the wavelength of light.[28-31] However, with an increased size of the metal, the surface plasmon resonance (SPR),[32, 33] which is expected to be achievable by metal NPs and is mainly supported by a dipolar plasmon mode in small size particles, disappears, resulting in inefficient excitation of electrons.

Alternatively, on the basis of its relatively large dimensions, an inverse opal (IO) structure can be suggested as a photon trapping structure that can readily interact with light in the UV-visible region.[34, 35] A photon trapping effect is a phenomenon in which the effective optical path length is increased by several times, triggered by an interaction between an object and light, i.e., scattering. TiO_2 inverse opal structures (TIO) have been studied as photocatalysts[3, 36, 37] and electrodes for dye-sensitized solar cells (DSSCs) [38-40] during the past decade. However, a rather low surface area relative to P-25 (Degussa), a standard active material for photoconversion systems has hampered the broad use of TIO in those areas. Therefore, systematically balancing two opposing factors, surface area and light trapping effects, is crucial to maximizing the power conversion efficiency in TIO-based systems; The pore size should be decreased to less than about 30 nm to increase the surface area for maximal contact of dye molecules onto the surface of the active materials.[41-44] On the other hand, large scale structures over a few hundred nanometers are needed in order to obtain an efficient light trapping effect caused by the interaction between objects with proper dimensions and incident light.[45-47] In this regard, a hierarchical structure is advantageous in that it can facilitate these two important properties simultaneously by accommodating two different dimensions in the structure.[7]

Here, we report an optimized gold NP-coated and surface-textured TIO (Au/st-TIO) structure in the form of larger scale TIO coated with smaller scale nanostructures and Au NPs. This structure can potentially broaden the range of photoconversion below the band gap of TiO_2 by enhancing the light harvesting effect and surface plasmon-enhanced electron transfer. The surface-textured TIO (st-TIO) is created by the selective removal of one domain in the layer of TiO_2–containing block copolymer precursors coated on the surface of TIO during the sintering process. By careful control of the large scale dimensions and introduction of small scale textures, we can successfully optimize the light trapping effect while securing sufficient surface area for reaction sites. Furthermore, the visible working capability in hydrogen generation of the Au/st-TIO structure is realized by the synergistic effect of photon trapping and a plasmon-enhanced transfer mechanism observed in the metal/semiconductor contact. The excellent photocatalytic activity of the properly designed Au/st-TIO structure provides strong potential for engineering of light in hydrogen generation systems.

2.1.2 Experimental procedures

2.1.2.1 Fabrication of TIO

PS nanospheres with different diameters (d = 130 nm, 350 nm, and 600 nm) were synthesized via Colvin's method.[48] Mono-dispersed PS nanospheres were assembled onto a TiO_2 thin layer coated FTO, which ensures good contact between the final TIO structure and the substrate. An O_2 plasma treated FTO substrate was dip-coated with 40 mM of $TiCl_4$ aqueous solution followed by annealing at 70 °C for 30 minutes. Scotch tape was applied to make a window with an area of 5 mm x 5 mm for the assembly of PS spheres. PS spheres were assembled by spin coating.[54] The height of the assembled PS layers was determined by the number of spin coating. Then, the samples were annealed at 85 °C for 1 hour on a hot plate so that assembled-PS nanospheres adhere well to the substrate. 1 μl of 0.9 M of $TiCl_4$ solution (water:ethanol=1:1) was infiltrated into the self-assembled PS opal structures. The $TiCl_4$/PS composite was then heated at 500 °C for 1 hour, providing a solution-gelation reaction and calcinations of PS nanospheres. A $TiCl_4$ aqueous solution was treated once again to make efficient electron transport networks.[55, 56] In the present case, conducting sol-gel chemistry within the PS template resulted in a decrease in diameter of 17 % for the formation of TIO networks. Furthermore, the creation of cracks is inevitable in the fabrication process of the TIO structure, as reported in previous studies.[30, 39, 40, 57, 58]

2.1.2.2 Fabrication of st-TIO and Au-NP coated st-TIO

The TIO networks were dip-coated in a diluted solution of triblock copolymer, poly(ethylene glycol)-*block*-poly(propylene glycol)-*block*-poly(ethylene glycol) ($EO_{20}PO_{70}EO_{20}$, M = 5800).[59] The solution was aged at 55 °C for 2 hours. After the yellow liquid turned into a bright yellow forming powder, the sample was removed from the vial and heated at 90 °C for 10 hours. Finally samples were washed with deionized water and ethanol followed by the heat treatment at 500 °C for 1 hour to calcine the block copolymer domains. For the gold NP coating on st-TIO, 30 mM of chloroauric acid was dissolved in ethanol, to which 1 wt.% of sodium citrate dissolved in water was added. The pH of the prepared solution was adjusted to be 8~9 before deposition. The mixture containing st-TIO structure was heated to 100°C for 30 min. and then allowed to cool naturally. The samples were washed with D. I. water and ethanol.

2.1.2.3 PEC measurements

The PEC performance of the electrodes was evaluated in a three-cell electrode system under front-side illumination of AM 1.5 G using a potentiostat (Princeton Applied research VersaSTAT3, AMETEK). An Ag/AgCl electrode and a Pt mesh were used as reference and counter electrodes, respectively. The electrolyte was a solution of 0.24 M Na_2S and 0.35 M Na_2SO_3. The working electrode with an exposed area of 0.25 cm^2 was illuminated from the front side. The photoresponse was measured under chopped illumination from a Newport solar simulator equipped with an AM 1.5G filter, calibrated with a standard Si solar cell simulating AM 1.5G. Photocurrent stability tests were carried out by measuring the photocurrent produced under chopped light irradiation (light/dark cycles of 10 s) at a fixed bias of +0.5 V versus Ag/AgCl.

2.1.3 Results and discussion

Figure 2.1.1 shows the four steps of the fabrication process for the Au/st-TIO structure. First, surface-activated polystyrene (PS) beads obtained by treatment with Triton X-100 were self-assembled using a spin-coating method into polycrystalline opals with a face-centered cubic (FCC) structure (I) on a FTO substrate with a thickness of 2.4 μm.[48] A $TiCl_4$ aqueous solution was then infiltrated into the 3D assembly of PS followed by annealing in air, which induced the gelation of TiO_2 sol and calcination of PS simultaneously, thus forming the TIO structure (III). After the third step, mesoporous structures composed of ~9 nm of TiO_2 textures are created by hydrothermal reaction of TiO_2 precursors and a thin layer of triblock copolymer solution and the second sintering of the sample. The targeted structure is st-TIO (IV) of a few hundred nanometer scale textured with mesoporous TiO_2 less than tens of nanometers in diameter. Finally, gold nanoparticles of approximately 30 nm in diameter are deposited onto st-TIO via a hydrothermal method (V).[49]

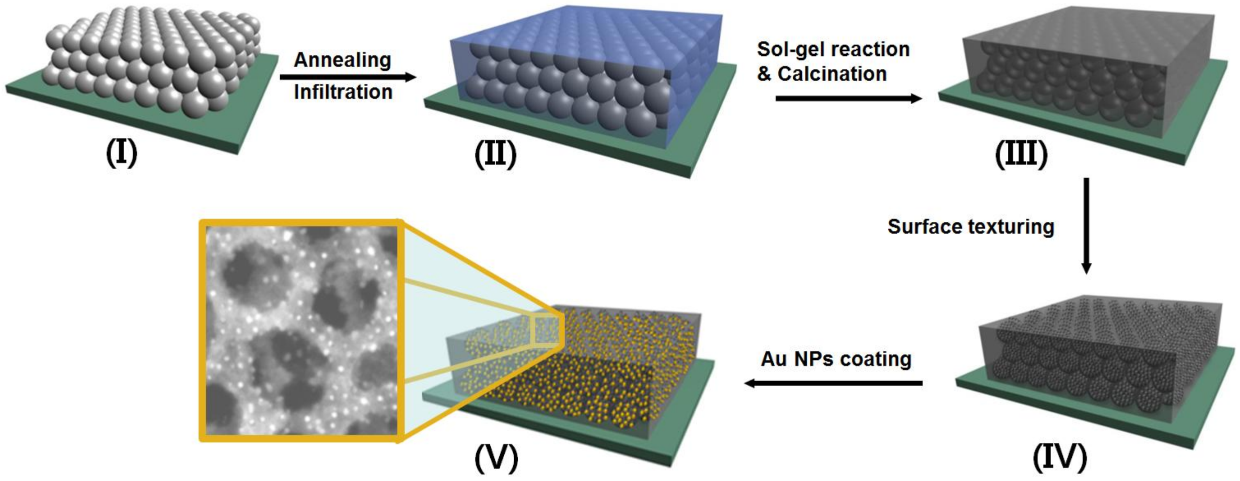

Figure 2.1.1 Schematic illustration of the fabrication process for a Au/st-TIO structure. I) Self-assembly of PS on FTO. II) 3D assembly of PS infiltrated by $TiCl_4$ solutions. III) TIO formed by the removal of PS and sol-gel reaction of TiO_2 precursors. IV) A st-TIO created by selective removal of one domain in the triblock copolymer film. V) A Au/st-TIO obtained by hydrothermal deposition of Au NPs on st-TIO.

Figure 2.1.2 presents scanning electron microscopy (SEM) images of the structure according to each step of the fabrication process (as described in the experimental section) of a visible light working electrode for surface plasmon-enhanced hydrogen generation, corresponding to the pristine PS assembly, TIO, st-TIO, and Au NP-coated st-TIO (Au/st-TIO). **Figure 2.1.2a** is a SEM image of a 3D assembly of PS with a diameter of 350 nm and a thickness of about 2.4 μm. The nearly face-centered cubic (FCC) crystal of the compact opal structure was found, as reported elsewhere.[48] **Figure 2.1.2b** is a SEM image of a 3D network of TiO_2 obtained by the gelation of $TiCl_4$ followed by the removal of the 3D assembly of PS by sintering at 500 ºC. Low-density TIO showing an underlying FCC lattice is apparent from the SEM image. The dimensions of the TIO generated from the removal of the PS template were reduced to approximately 83 % of the original thickness due to shrinkage induced by the sol-gel reaction. We varied the diameters of the PS spheres and sintering conditions in order to optimize light harvesting capability. **Figure 2.1.2c** is a SEM image of st-TIO that clearly shows the creation of small scale textures. The inset shows a close-up image of the st-TIO with a larger diameter of air holes of 290 nm and a beam diameter of ~ 40 nm coated with TiO_2 textures with a smaller diameter of ~ 9 nm. The small size textures are attributable to the selective removal of PPO domains formed by the assembly of the PEO-PPO-PEO triblock copolymer. **Figure 2.1.2d** shows the ~ 30 nm Au-NPs deposited on st-TIO with a dimension of 290 nm (fabricated from 350 nm PS nanospheres). The inset confirms the presence of two types of smaller scale nanostructures (TiO_2 textures and Au-NPs). The brighter spots represent Au NPs, due to the larger reflection/scattering cross section of Au during the process of imaging in SEM.

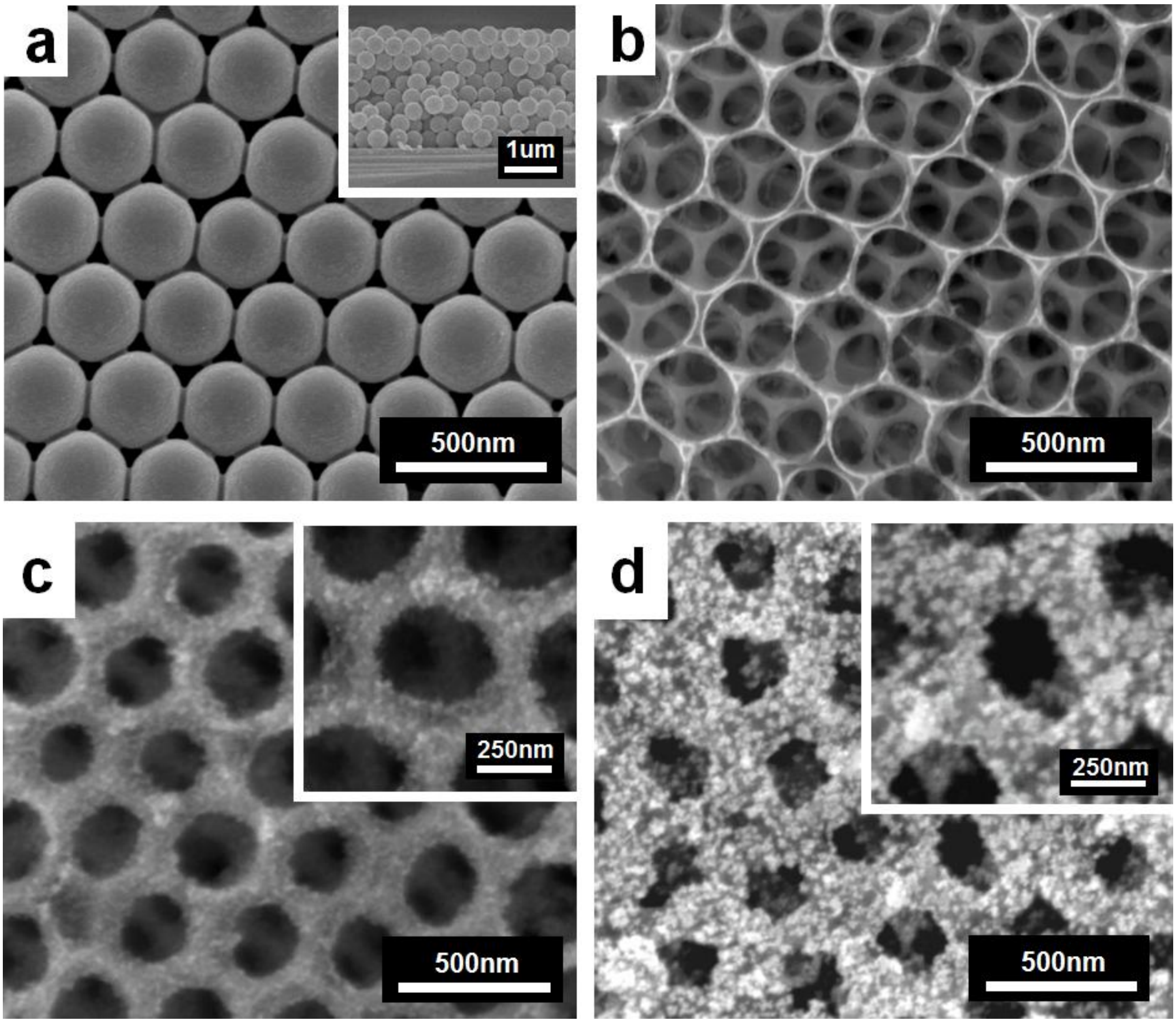

Figure 2.1.2 Morphological characterization of the structures. a) SEM image of the 3D assembly of PS. The inset shows the cross-sectional image of the 3D assembly. b) SEM image of TIO networks created from infiltration of $TiCl_4$ followed by gelation of TiO_2 sol and removal of the PS assembly. c) SEM image of st-TIO networks with a diameter of 350 nm coated with small TiO_2 textures with a diameter of 9 nm in the form of a hierarchical structure. The inset is a close-up image of st-TIO. d) SEM image of gold-NP coated st-TIO. The inset shows the presence of gold NPs and the mesoporous TiO_2 textures.

Figure 2.1.3a shows a high-resolution transmission electron microscopy (TEM) image of the as-prepared st-TIO that confirms the TiO_2 is crystalline with an interplanar d-spacing of 0.31 nm corresponding to the (101) plane. It is seen that the st-TIO is a mesoporous structure with a diameter of about 9 nm and tightly connected with a thick layer of TIO in a beam diameter of ~ 40 nm. There was a tendency in the experiment for TiO_2 textures to aggregate and form mesoporous clusters with a diameter of ~20 nm as marked in **Figure 2.1.3a**. **Figure 2.1.3b** is a TEM image of the surface of the Au/st-TIO showing the presence of two types of nanoscale structures. The two different degrees of interplanar spacing, 0.31 and 0.22 nm in **Figures 2.1.3a** and **2.1.3b**, indicate the textures of anatase TiO_2 and the Au NPs, respectively. X-ray diffraction (XRD) measurements were made to further confirm the formation of TiO_2 after the sol-gel reaction and application of the hydrothermal method. **Figure 2.1.3c** shows the XRD pattern of the sol-gel fabricated TiO_2 nanostructures (TIO), st-TIO created from hydrothermal treatment of the block copolymer on the surface of TIO, and Au/st-TIO fabricated by hydrothermal deposition of Au NPs on st-TIO. The X-ray diffraction analysis verifies that the as-synthesized st-TIOs are in an anatase phase with enhancement at 25^o and 38^o corresponding to the (101) and (004) planes, as confirmed by # JCPDS 84-1286. These peaks confirm that the $TiCl_4$ is completely converted to crystalline anatase TiO_2, which indicates the presence of feasible conducting pathways in TIO networks. The XRD peaks of Au/st-TIO with enhancement at 38^o, 44^o, 65^o and 77^o, corresponding to the planes of (111), (200), (220) and (311), confirm the crystalline nature of the Au. Furthermore, the TiO_2 textures maintain spacing and a 2 theta value in the Au/st-TIO as shown in the TEM images and XRD data, respectively, indicating the stability of the TiO_2 nanostructure in the basic condition that is applied for the deposition of Au NPs or the photocatalytic hydrogen generation reaction (see the experimental section).

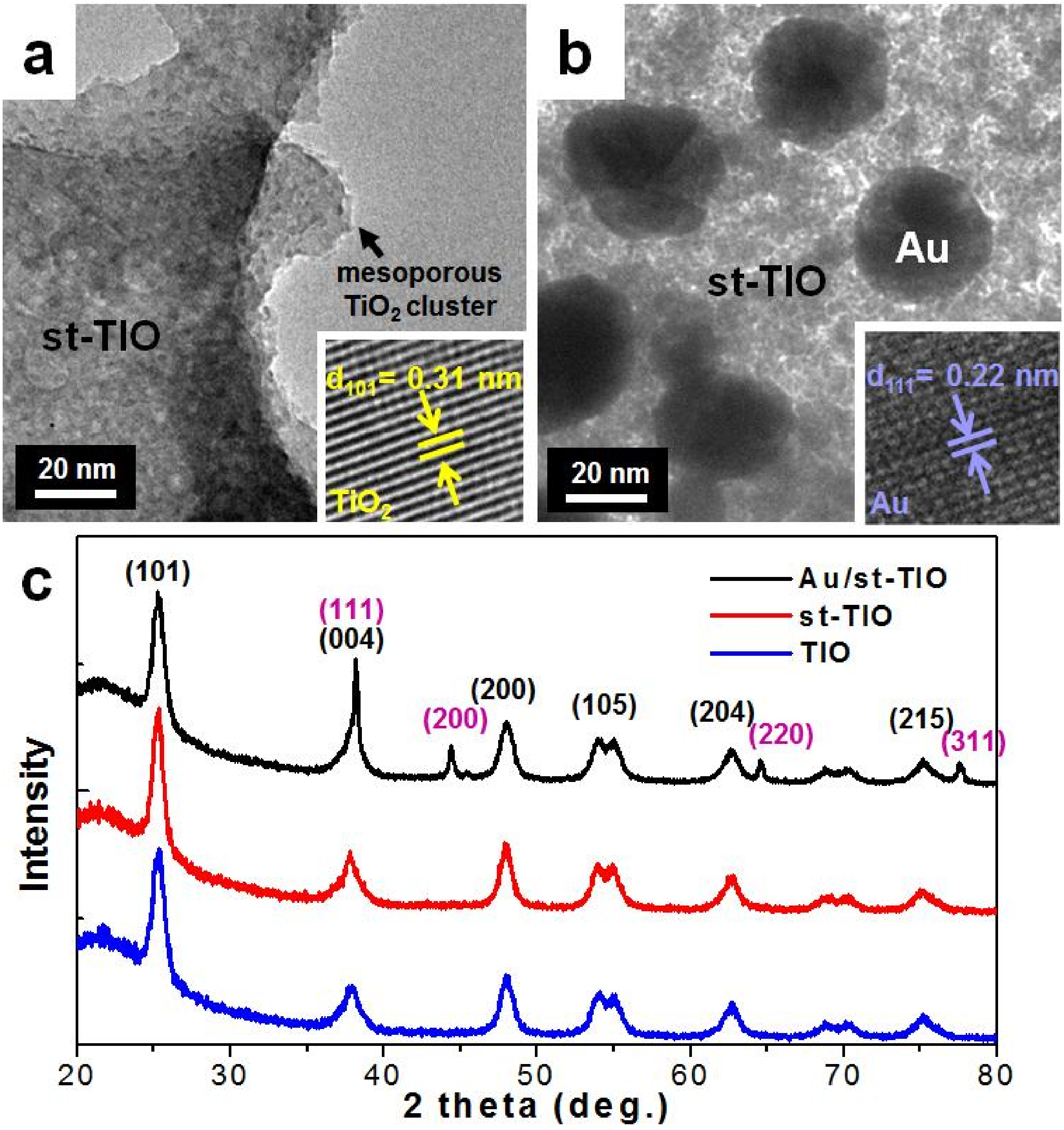

Figure 2.1.3 TEM images and XRD of st-TIO and Au/st-TIO networks. a) TEM image of the st-TIO structure. The close-up image in the inset confirms the single crystalline phase of as-prepared st-TIO with an interplanar spacing of 0.31 nm. b) TEM image of Au/st-TIO structure. The interplanar spacing of 0.22 represents the Au NPs. c) XRD of TIO and st-TIO, and Au/st-TIO from bottom to top. The numbers in brackets in black and in pink represent the lattice planes of anatase TiO_2 and gold NPs, respectively.

The enhanced optical properties due to the introduction of properly designed dimensions and Au NPs can be quantified by shining light on the front side of a P-25 control sample, TIO samples, st-TIO samples, and Au/st-TIO samples (from the top to the FTO substrate). **Figure 2.1.4a** compares the UV-Vis extinction spectra of a 2 μm thick NC-TiO_2 film (P-25), and similar thicknesses of TIO structures fabricated from PS with diameters of 130 nm, 350 nm, and 600 nm at normal incidence. All UV-vis absorption spectra are normalized by the thickness of the corresponding samples. P-25 was chosen as a control sample since it has shown excellent performance as a working electrode in photovoltaic devices. The absorption peaks spanning from 300 to 400 nm were assigned to the absorption of the conventional TiO_2 nanoparticles. Unlike the previously reported results on the photon trapping effects based on the slow photon propagation mechanism of photonic crystal structures at the bandgap edge[3, 36], the TIO samples assembled by simple spin-coating methods did not show specific reflectance peaks due to the polycrystalline nature of the opal structure with some defects. However, the TIO samples without the perfect photonic bandgaps, thus no slow photons at normal incidence, still demonstrated a strong and broad absorption band ranging from 400 to 800 nm due to scattering, relative to the P-25 control sample, even though the density of TiO_2 in the TIO samples with larger scale air holes (300 nm) is much lower than that of P-25, which is densely packed with much smaller (25 nm in diameter) scale TiO_2 particles. The enhanced absorption of the TIO samples in this region is attributed to the photon trapping effect obtained by the larger dimensions of TIO, which can readily interact with light in the visible region. This implies that much more light is able to participate in the light harvesting process in the TIO structure acting as a mirror: some photons that are not absorbed upon their first passage are scattered by the TIO frame again, effectively giving those photon multi-passes through the networks. However, compared to the large absorption cross-section of the TIO structure at a long wavelength, the absorption in the UV range of TIO is still less than that of the P-25 control sample, which is likely due to the low areal density of the TIO samples. We hypothesized that the addition of smaller dimensions to TIO by surface-texturing could successfully address this problem. In fact, the surface area of TIO (350 nm in diameter) obtained by BET is increased by surface-texturing from 33.9 m^2/g to 124.9 m^2/g, exceeding the value (117 m^2/g) of P-25, as shown in **Figure 2.1.5**. As a result, the cross-sectional area of UV-vis absorption is substantially improved after surface-texturing of the corresponding plain TIO in the entire wavelength region for all the cases as shown in **Figure**

2.1.4b. This implies that the low density of TIO could be overcome by the adoption of a mesoporous hierarchical structure. The optimal structure with the maximum cross-section area achieved by integration of small dimensions in the UV-absorption curve is st-TIO with a diameter of a 350 nm, as shown in **Table 2.1.1**. The intensity of the photon trapping effect caused by scattered light under beam irradiation on the device was further investigated by comparing the diffuse reflection spectra of a P-25 control film and st-TIO with different dimensions. As can be seen in **Figure 2.1.4c**, compared to the P-25 control film, the st-TIO structures showed significantly higher diffuse reflection spectra in the visible spectrum of light (400 nm - 800 nm), indicating that the absorbed light was efficiently scattered within the nanostructure film. This result confirms extension of the path length of the light within the TIO with a few hundred nanometers scale. Here, our approach is different from other methods that pursue hierarchical TIO[37] in that we maximize the surface area by surface-texturing of TIO without filling air holes with small dimension structures. This makes it possible to maintain a refractive index contrast between the large scale TIO frame and air, which is essential for the photon trapping effect.[50, 51] As a result, st-TIO with a diameter of 350 nm and 600 nm had a much larger photon trapping effect than P-25 and the light scattering factor of st-TIO was significant in the entire wavelength region. On the other hand, there was only a slight light scattering effect for the TIO made from 130 nm PS nanospheres, which was likely due to inefficient interaction between the relatively smaller dimension nanostructures and exposed light. We observed that the light scattering effect increased with an increase in the pore size in the range of the wavelength-scale of exposed light. The optimized dimension of the st-TIO frame is 350 nm, which allows excellent photon-trapping effects while retaining appropriate surface area, according to the data in Table 1. **Figure 2.1.4d** compares the final UV-vis absorption spectra of st-TIO and Au/st-TIO, demonstrating the potential for surface plasmon resonance in the metal/semiconductor interfaces. A broad absorption covering a range of 500-700 nm with an absorption maximum at about 540 nm appeared in the spectra of all Au/st-TIO samples, and is attributed to enhanced surface plasmons in Au NPs.

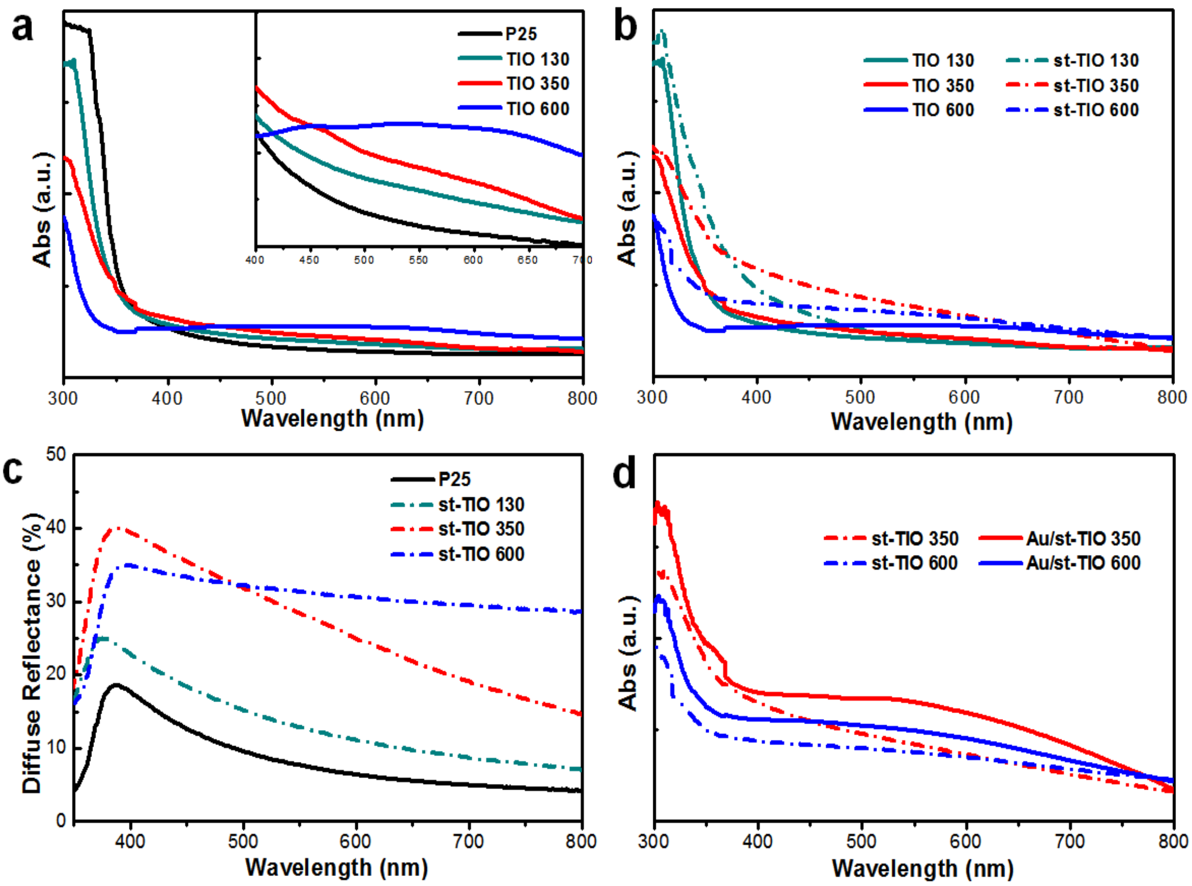

Figure 2.1.4 Optical properties of the P-25, TIO, st-TIO and Au/st-TIO structure made from PS spheres with different diameters. (a) UV-vis absorption spectra of the samples with a diameter of 130 nm, 350 nm, and 600 nm. (b) UV-vis absorption spectra of the TIO networks before and after surface texturing. (c) Diffuse reflectance spectra of the samples with a diameter of 130 nm, 350 nm, and 600 nm. (d) UV-vis absorption spectra of Au-NP coated st-TIO with a diameter of 350 nm and 600 nm.

a

Nanostructure	Surface area (m^2/g)
TIO (350 nm)	33.912
St-TIO (350 nm)	124.90
NC-TiO_2	117.21

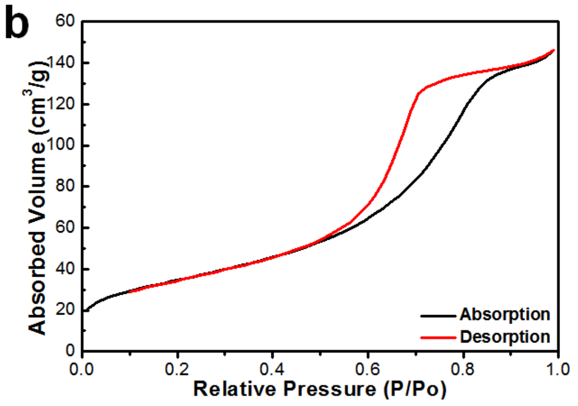

Figure 2.1.5 a) Comparison the surface area of nanostructures. b) The N_2 adsorption-desorption isotherm curve of the st-TIO with a diameter of 350 nm.

In order to investigate the hydrogen generation activity of the samples, photo-electrochemical measurements were carried out directly on P-25 control samples, TIO, st-TIO, and Au-NP coated st-TIO. Ag/AgCl, a Pt mesh, and as-prepared samples are used as a reference electrode, counter electrode, and working electrode, respectively, in a 0.24 M Na_2S/0.35 M Na_2SO_3 electrolyte solution. As shown in **Figure 2.1.6a** illustrating the electron transfer mechanism of Au/st-TIO, after the electrons are transferred from gold nanoparticles to the conduction band of TiO_2 upon illumination, the electrons travel to the counter electrode where the hydrogen generation reaction is driven. Meanwhile, the holes diffused to the surface of TiO_2 or Au oxidize S^{2-} and SO_3^{2-}.[52, 53] In detail, the photocatalytic hydrogen generation proceeds by the following three steps: (a) incident photons are absorbed by the Au NPs, which is creating electrons; (b) the electrons are transferred from Au NPs to the conduction band of TiO_2; (c) the electrons transferred from TiO_2 to the counter electrode reduce the hydrogen ions, whereas the holes induce the oxidation reaction at the surface of the working electrode. **Figure 2.1.6b** presents linear-sweep voltammograms of P-25 and st-TIOs, which can be explained by the direct photoexcitation of electrons from the valence band of TiO_2, under AM 1.5 G simulated sunlight illumination. All st-TIO samples show higher photocurrent density than the P-25 control sample, which is likely due to having an adequate surface area and additional photon trapping effects. This suggests that the larger dimensions in st-TIO trigger favorable photon trapping effects and help to transfer collected electrons more efficiently through the 3D connectivity of TIO. The photocurrent density of the st-TIO with a diameter of 350 nm, an optimized one as proved in **Figure 2.1.4** and **Table 2.1.1**, is approximately 2 times greater than that of the P-25 control sample at an applied bias of +0.5 V. Furthermore, when the system is supported by surface plasmon resonance, the photocurrent density reaches ~ 0.8 mA/cm^2, which is about three times higher than that obtained with bare TIO under illumination of 100 mW/cm^2 (**Figure 2.1.7**). More surprisingly, as shown in **Figure 2.1.6c**, the photocurrent density of Au/st-TIO created by only visible light illumination (in red, AM 1.5 with a cutoff filter (>420 nm)) is almost 1/5 and 1/8 of that of the Au/P-25 sample and the same sample, illuminated by UV-visible light, respectively, indicating that the optimized structure has solely visible light working capability. Overall, the power conversion efficiency of Au/st-TIO under the UV-visible illumination (~2.58 times larger than that of P-25) is enhanced by a factor of 2.07 and 2.86 by the adoption of surface texturing and surface-plasmon mechanism, respectively, as shown in **Figure 2.1.7**, which can be supported by the

IPCE data in **Figure 2.1.8**. **Figure 2.1.6d** shows the photoresponse over time (I-t curve) of the Au/st-TIO measured at +0.5 V with chopped illumination of AM 1.5 at a rate of 10 s exposure followed by 10 s non-illumination. The sharp spike in the photocurrent during the on/off illumination cycles indicates suitably fast two step transport of photogenerated electrons from Au NPs to the current collector via the textures of TiO_2 and the interior of the TiO_2 networks.

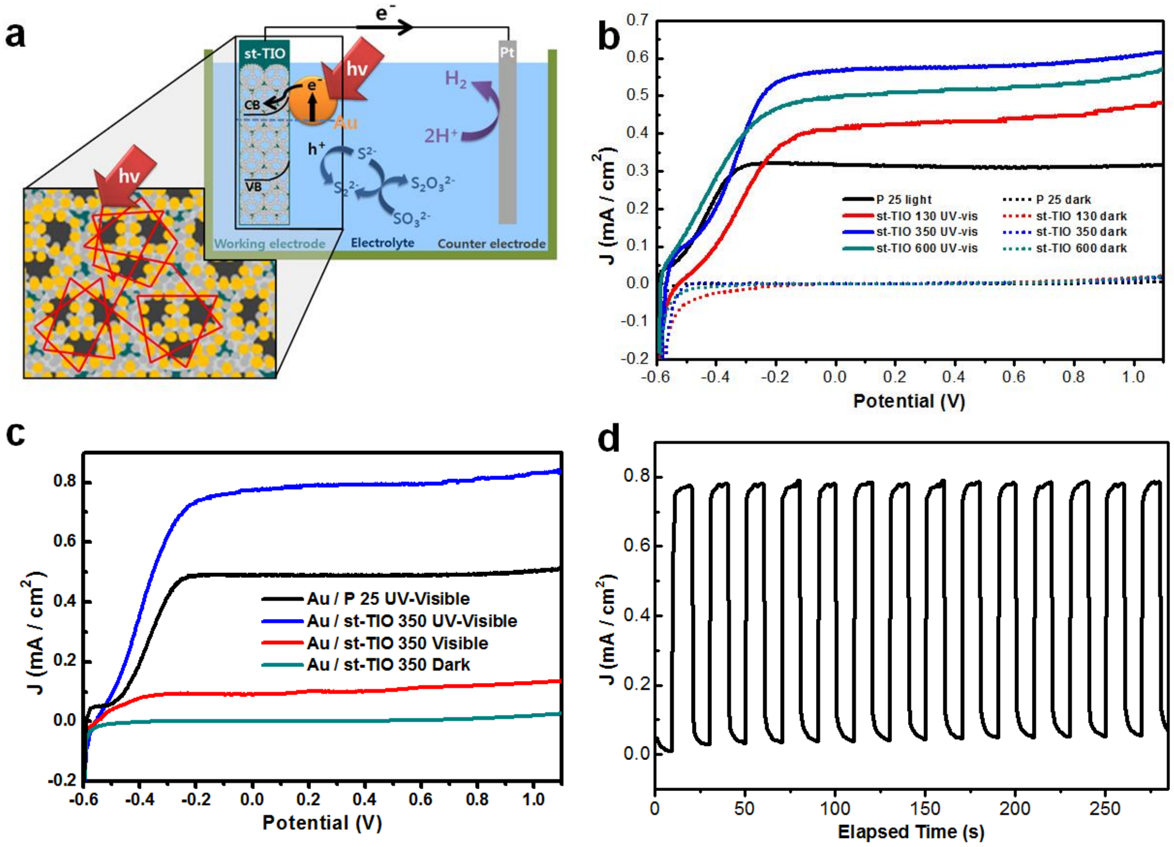

Figure 2.1.6 Photocurrent response of plain P-25, TIO, st-TIO and Au/st-TIO under AM 1.5 illumination. (a) Schematic diagram showing the hydrogen generation mechanism of Au/st-TIO. (b) I-V curve of P-25 and st-TIO structures with different diameters. (c) I-V curve of Au/P-25 under UV-visible and Au/st-TIO structures with a diameter of 350 nm under UV-visible, visible light illumination, and dark conditions. (d) I-t curve of Au/st-TIO structures with a diameter of 350 nm at a bias of +0.5V under UV-visible illumination. The photocurrents of all samples are normalized by their thicknesses.

Table 2.1.1 Comparison of UV-visible cross-sectional area obtained by the integration of UV-visible absorption curve from 300 to 800 nm and 420 to 800 nm for UV-vis and Visible values, respectively.

	TIO	st-TIO		Au/st-TIO	
	UV-vis	UV-vis	Visible	UV-vis	Visible
130	148.01	192.45	78.29	-	
350	143.03	219.80	123.21	289.88	179.88
600	136.39	175.25	115.24	220.34	143.32
P-25	156.21		55.18	-	

Figure 2.1.7 Experimental setup of PEC measurement.

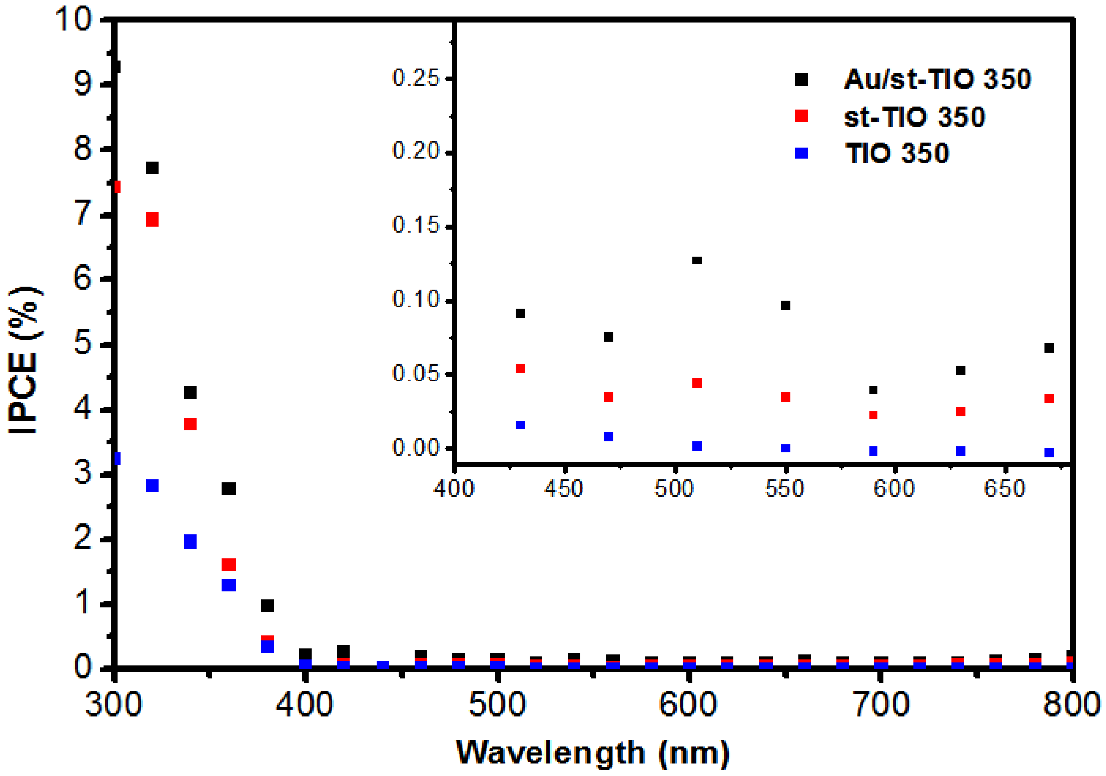

Figure 2.1.8 IPCE measurement of Au/st-TIO, st-TIO and TIO under UV-visible range illumination (300-800 nm). The inset is the zoomed-up image of IPCE data showing the increment of Au/st-TIO and st-TIO in the visible region.

2.1.4 Conclusion

In conclusion, we report a finely designed st-TIO structure that efficiently balances light trapping effects and surface area requirements by the introduction of a surface-textured coating onto a TIO structure with dimensions of a few hundred nanometer scale. The observed optical properties confirm large light harvesting effects in the TIO in the long wavelength region, which facilitate the hydrogen generation reaction of a TiO_2 semiconductor in the UV-vis range. The st-TIO was further optimized as a visible light working hydrogen generation electrode by the introduction of Au NPs, which facilitate surface plasmon-enhanced hydrogen generation. The photocurrent of Au/st-TIO was 2.58 times greater than that of the conventional P-25 photoelectrode, which is recognized for outstanding performance. The excellent performance of Au/st-TIO suggests that this strategy can provide a new route to design photoactive materials via systematic engineering of light.

2.1.5 References

1. Walter, M. G.; Warren, E. L.; McKone, J. R.; Boettcher, S. W.; Mi, Q.; Santori, E. A.; Lewis, N. S. *Chemical Reviews* **2010,** 110, (11), 6446-6473.

2. Chen, X.; Shen, S.; Guo, L.; Mao, S. S. *Chemical Reviews* **2010,** 110, (11), 6503-6570.

3. Lu, Y.; Yu, H.; Chen, S.; Quan, X.; Zhao, H. *Environmental Science & Technology* **2012,** 46, (3), 1724-1730.

4. Paramasivam, I.; Jha, H.; Liu, N.; Schmuki, P. *Small* **2012,** 8, (20), 3073-3103.

5. Qiu, Y.; Yan, K.; Deng, H.; Yang, S. *Nano Lett.* **2011,** 12, (1), 407-413.

6. Yang, X. Y.; Wolcott, A.; Wang, G. M.; Sobo, A.; Fitzmorris, R. C.; Qian, F.; Zhang, J. Z.; Li, Y. *Nano Lett.* **2009,** 9, (6), 2331-2336.

7. Liu, J.; Li, M.; Wang, J.; Song, Y.; Jiang, L.; Murakami, T.; Fujishima, A. *Environmental Science & Technology* **2009,** 43, (24), 9425-9431.

8. McDonald, K. J.; Choi, K.-S. *Chemistry of Materials* **2011,** 23, (21), 4863-4869.

9. Kim, J.; Lee, C. W.; Choi, W. *Environmental Science & Technology* **2010,** 44, (17), 6849-6854.

10. Lytle, J. C.; Denny, N. R.; Turgeon, R. T.; Stein, A. *Advanced Materials* **2007,** 19, (21), 3682-3686.

11. Zhong, J.-H.; Li, G.-R.; Wang, Z.-L.; Ou, Y.-N.; Tong, Y.-X. *Inorganic Chemistry* **2010,** 50, (3), 757-763.

12. Pang, M.; Zeng, H. C. *Langmuir* **2010,** 26, (8), 5963-5970.

13. Linsebigler, A.; Lu, G.; Yates, J. *Chemical Reviews* **1995,** 95, 735-758.

14. Hwang, Y. J.; Hahn, C.; Liu, B.; Yang, P. D. *ACS Nano* **2012,** 6, (6), 5060-5069.

15. Cheung, K. Y.; Yip, C. T.; Djurišić, A. B.; Leung, Y. H.; Chan, W. K. *Advanced Functional Materials* **2007,** 17, (4), 555-562.

16. Xie, Y.; Fu, D. *Journal of Applied Electrochemistry* **2010,** 40, (7), 1281-1291.

17. Xu, Z.; Yu, J. *Nanoscale* **2011,** 3, (8), 3138-44.

18. Park, J. H.; Kim, S.; Bard, A. J. *Nano Lett.* **2006,** 6, (1), 24-28.

19. Xiong, Z. G.; Zhao, X. S. *Journal of the American Chemical Society* **2012,** 134, (13), 5754-5757.

20. Liu, L. P.; Wang, G. M.; Li, Y.; Li, Y. D.; Zhang, J. Z. *Nano Res.* **2011,** 4, (3), 249-258.

21. Jung, M.-H.; Kang, M. G. *Journal of Materials Chemistry* **2011,** 21, (8), 2694-2700.

22. Luo, J.; Karuturi, S. K.; Liu, L.; Su, L. T.; Tok, A. I.; Fan, H. J. *Scientific reports* **2012,** 2, 451.

23. Cheng, C.; Karuturi, S. K.; Liu, L.; Liu, J.; Li, H.; Su, L. T.; Tok, A. I. Y.; Fan, H. J. *Small* **2012,** 8, (1), 37-42.

24. Thiyagarajan, P.; Ahn, H.-J.; Lee, J.-S.; Yoon, J.-C.; Jang, J.-H. *Small* **2013**.

25. Liu, Z.; Hou, W.; Pavaskar, P.; Aykol, M.; Cronin, S. B. *Nano Lett.* **2011,** 11, (3), 1111-1116.

26. Cushing, S. K.; Li, J. T.; Meng, F. K.; Senty, T. R.; Suri, S.; Zhi, M. J.; Li, M.; Bristow, A. D.; Wu, N. Q. *Journal of the American Chemical Society* **2012,** 134, (36), 15033-15041.

27. Chen, X.; Liu, L.; Yu, P. Y.; Mao, S. S. *Science* **2011,** 331, (6018), 746-750.

28. You, E.-A.; Zhou, W.; Suh, J. Y.; Huntington, M. D.; Odom, T. W. *ACS Nano* **2012,** 6, (2), 1786-1794.
29. Kooij, E. S.; Ahmed, W.; Zandvliet, H. J. W.; Poelsema, B. *The Journal of Physical Chemistry C* **2011,** 115, (21), 10321-10332.
30. Zhao, Y.; Yang, B.; Xu, J.; Fu, Z.; Wu, M.; Li, F. *Thin Solid Films* **2012,** 520, (9), 3515-3522.
31. Zhang, Z.; Zhang, L.; Hedhili, M. N.; Zhang, H.; Wang, P. *Nano Lett.* **2013,** 13, (1), 14-20.
32. Jones, M. R.; Osberg, K. D.; Macfarlane, R. J.; Langille, M. R.; Mirkin, C. A. *Chem Rev* **2011,** 111, (6), 3736-827.
33. Zhou, X.; Liu, G.; Yu, J.; Fan, W. *Journal of Materials Chemistry* **2012,** 22, (40), 21337-21354.
34. Sordello, F.; Duca, C.; Maurino, V.; Minero, C. *Chemical Communications* **2011,** 47, (21), 6147-6149.
35. Sordello, F.; Maurino, V.; Minero, C. *Journal of Materials Chemistry* 21, (47), 19144-19152.
36. Liu, J.; Liu, G.; Li, M.; Shen, W.; Liu, Z.; Wang, J.; Zhao, J.; Jiang, L.; Song, Y. *Energy & Environmental Science* **2010,** 3, (10), 1503-1506.
37. Shen, W.; Li, M.; Wang, B.; Liu, J.; Li, Z.; Jiang, L.; Song, Y. *Journal of Materials Chemistry* **2012,** 22, (16), 8127-8133.
38. Liu, L.; Karuturi, S. K.; Su, L. T.; Tok, A. I. Y. *Energy & Environmental Science* **2011,** 4, (1), 209-215.
39. Seo, Y. G.; Woo, K.; Kim, J.; Lee, H.; Lee, W. *Advanced Functional Materials* **2011,** 21, (16), 3094-3103.
40. Kwak, E. S.; Lee, W.; Park, N.-G.; Kim, J.; Lee, H. *Advanced Functional Materials* **2009,** 19, (7), 1093-1099.
41. Pan, J. H.; Lei, Z.; Lee, W. I.; Xiong, Z.; Wang, Q.; Zhao, X. S. *Catalysis Science & Technology* **2012,** 2, (1), 147-155.
42. Poznyak, S. K.; Kokorin, A. I.; Kulak, A. I. *Journal of Electroanalytical Chemistry* **1998,** 442, (1), 99-105.
43. Wang, J.; Li, Q.; Knoll, W.; Jonas, U. *Journal of the American Chemical Society* **2006,** 128, (49), 15606-15607.
44. Shchukin, D. G.; Caruso, R. A. *Chemistry of Materials* **2004,** 16, (11), 2287-2292.
45. Ahn, H.-J.; Kim, S.-I.; Yoon, J.-C.; Lee, J.-S.; Jang, J.-H. *Nanoscale* **2012,** 4, (15), 4464-4469.
46. Usami, A. *Chemical Physics Letters* **1997,** 277, (1), 105-108.
47. Ahn, H.-J.; Thiyagarajan, P.; Jia, L.; Kim, S.-I.; Yoon, J.-C.; Thomas, E. L.; Jang, J.-H. *Nanoscale* **2013**.
48. Colvin, V. L. *MRS Bulletin* **2001,** 26, (08), 637-641.
49. MurdochM; Waterhouse, G. I. N.; Nadeem, M. A.; Metson, J. B.; Keane, M. A.; Howe, R. F.; LlorcaJ; IdrissH. *Nature Chemistry* **2011,** 3, (6), 489-492.
50. Cho, C.-Y.; Moon, J. H. *Langmuir* **2012,** 28, (25), 9372-9377.
51. Mandlmeier, B.; Szeifert, J. M.; Fattakhova-Rohlfing, D.; Amenitsch, H.; Bein, T. *Journal*

of the American Chemical Society **2011,** 133, (43), 17274-17282.
52. Hensel, J.; Wang, G.; Li, Y.; Zhang, J. Z. *Nano Lett.* **2010,** 10, (2), 478-483.
53. Yun, H. J.; Lee, H.; Kim, N. D.; Lee, D. M.; Yu, S.; Yi, J. *ACS Nano* **2011,** 5, (5), 4084-4090.
54. Mihi, A.; Ocaña, M.; Míguez, H. *Advanced Materials* **2006,** 18, (17), 2244-2249.
55. Yu, H.; Zhang, S.; Zhao, H.; Xue, B.; Liu, P.; Will, G. *The Journal of Physical Chemistry C* **2009,** 113, (36), 16277-16282.
56. Fuke, N.; Katoh, R.; Islam, A.; Kasuya, M.; Furube, A.; Fukui, A.; Chiba, Y.; Komiya, R.; Yamanaka, R.; Han, L.; Harima, H. *Energy & Environmental Science* **2009,** 2, (11), 1205-1209.
57. Ruani, G.; Ancora, C.; Corticelli, F.; Dionigi, C.; Rossi, C. *Solar Energy Materials and Solar Cells* **2008,** 92, (5), 537-542.
58. Li, Y.; Piret, F.; Leonard, T.; Su, B. L. *Journal of colloid and interface science* **2010,** 348, (1), 43-8.
59. Kim, D. S.; Kwak, S.-Y. *Applied Catalysis A: General* **2007,** 323, (0), 110-118.
60. Kim, K.;Thiyagarajan, P.; Ahn, H.-J.; Kim, S.-I.; Jang, J.-H. *Nanoscale* **2013,** 5, (14), 6254-6260.

2.2 Towards visible light hydrogen generation: quantum dot-sensitization via efficient light harvesting of hybrid-TiO_2

Adapted with permission from ref. 45. Copyright 2013 Springer Nature

2.2.1 Introduction

Photoelectrochemical (PEC) cells are useful devices designed for the chemical process of generating hydrogen via electrolysis of water, namely water splitting, under irradiation of a broad spectrum of sunlight.[1-4] In general, PEC devices are composed of photoelectrodes, where oxidation/reduction of water occurs with response to sunlight, and appropriate aqueous electrolytes containing a redox couple.[5-7] TiO_2 has proven to be a promising photoelectrode in photoconversion systems due to its flat band potential, fast electron transfer mechanism, and photoelectrochemical stability in most aqueous solutions.[8-10] However, the use of TiO_2 as a single electrode material is fundamentally hampered by its large bandgap (3.2 eV), thus resulting in truncated and inclusively low efficiency in the visible region, which accounts for more than half of the entire sunlight spectrum. Accordingly, extending the light absorption window of the photoelectrode to visible light is considered critical to increase the efficiency of photoconversion.[11-13] Notable efforts to lower the bandgap of TiO_2 include doping of heteroatoms[14-16] or coating of metal or semiconductor particles utilizing excitation of surface plasmons[17-19] or quantum dot-sensitization,[5, 20, 21] permitting excitation of electrons in the photoelectrodes at energies much below TiO_2's original energy bandgap.[22-24] Among these approaches, quantum dot-sensitization has drawn considerable attention since it has shown an enhanced interfacial charge transfer mechanism via multiple excitations by single photon absorption.

Light harvesting refers to enhancement of absorbed light via either photon trapping[25-27] or anti-reflection (AR),[28-30] leading to an increase in the fraction of available light.[31, 32] It has been reported that nanostructures can exhibit excellent absorption properties in the visible region via light harvesting, when their dimensions are comparable to the wavelength of light.[33] By enhancing absorption in the visible range via light harvesting, it becomes possible to more effectively sensitize quantum dots with a bandgap in the range of visible light, leading to maximal power conversion efficiency of quantum dot-based PEC cells.

Mesoporous TiO_2 nanostructures fabricated by P25 with a mean diameter of about 25 nm have been widely used for fabrication of the working electrode in dye-sensitized solar systems, a representative photoconversion system, due to their advantage of large surface area for adsorption of dye molecules. However, the small particles are not able to efficiently harvest light in the red and near-infrared regions of the light spectrum and they also reflect a large amount of light due to the high refractive index of TiO_2. Proper modification of the P25 photoelectrode is thus needed and careful design of quantum dot-sensitized devices based on a light harvesting mechanism is crucial to maximize the efficiency in photoconversion systems.

Here, we report an optimized quantum dot-sensitized hybrid-TiO_2 (QD/H-TiO_2) electrode sandwiched with light harvesting layers. The H-TiO_2 electrode is constructed using a 4.5 μm thick mesoporous TiO_2 film made of crystalline nanoparticles (25 nm) and additionally a 500 nm-thick patterned mesoporous TiO_2 layer on the top and 1 μm-thick surface-textured TIO (st-TIO) layer on the bottom, both with diameters on the order of hundreds of nanometers, with the capability of AR and photon trapping, respectively, contributing to maximized light harvesting. The configuration of the light harvesting layer sitting on both the bottom and top of the mesoporous TiO_2 layer provides devices with similar mechanism to mirrors in a laser, where entrapped light is enhanced by repeated reflection at both ends and thus maximizes the intensity of the absorbed light at a wider solar spectrum. Furthermore, CdSe/H-TiO_2 greatly broadens the range of photoconversion below the band gap of H-TiO_2 by enhanced quantum dot-sensitized electron transport substantially supported by the light harvesting mechanism of H-TiO_2. Under AM 1.5 G simulated sunlight illumination, the maximum photocurrent density of CdSe/H-TiO_2 reaches ~ 16.2 mA/cm^2, which is 35% higher than that of the optimized control sample (CdSe/P25), at an applied bias of 0.5 V versus Ag/AgCl. More surprisingly, the photocurrent from hydrogen generation of CdSe/H-TiO_2 solely by the visible spectrum reaches ~ 14.2 mA/cm^2, which is the highest record value in the visible range and almost 88 % of that obtained under UV-visible irradiation. The greatly improved performance of CdSe/H-TiO_2, which is attributable to the ability of light harvesting of H-TiO_2, suggests the strong need for engineering light in photoconversion systems.

2.2.2 Experimental procedures

2.2.2.1 Fabrication of p-P25 and H-TiO$_2$

In order to fabricate p-P25, a 5 mm x 5 mm size patterned PDMS with 500 nm thickness was prepared from the patterned SU8 with air holes with diameter of 500 nm and 500 nm in thickness. Scotch tape was attached to the FTO substrate to define the sample size as 5 mm x 5 mm. P25 paste was placed and flattened via the doctor blade method so that paste had uniform height corresponding with that of the scotch tape. The P25 paste was imprinted by the patterned PDMS with proper pressure so that no air bubbles formed. After annealing the samples at 55 ^{o}C for 45 min to remove the residual solvent, the patterned PDMS and the scotch tape were peeled off. The PDMS can be reused after washing with ethanol. The sample was heated at 500 ^{o}C for 30 min for calcination, followed by TiCl$_4$ treatment with a concentration of 40 mM at 70 ^{o}C for 30 min and final heat treatment at 500 ^{o}C for 30 min. When the st-TIO/FTO substrate was replaced by a FTO substrate, a H-TiO$_2$ structure was created.

2.2.2.2 Fabrication of CdSe/H-TiO$_2$

The successive ionic layer adsorption and reaction (SILAR) process was used to deposit CdSe onto a H-TiO$_2$/FTO substrate. A sodium selenosulfate (Na$_2$SeSO$_3$) solution was prepared by dissolving 0.01 mol Se powder in a 0.1 M Na$_2$SO$_3$ solution at 90 ^{o}C for 9 hours. To assemble CdSe onto H-TiO$_2$, the H-TiO$_2$/FTO substrate was dipped into a 50 mM Cd(Ac)$_2$ · 2H$_2$O ethanol solution for 1 min, washed with ethanol for 30s, and then dipped into a Na$_2$SeSO$_3$ solution for 1 min and rinsed with D.I. water for 30s. Finally, the CdSe/H-TiO$_2$ substrate was dried by blowing nitrogen gas. The two-step dipping procedure is defined as one SILAR cycle. This procedure was repeated twenty times to obtain the desired performance of CdSe and carried out in a glove box filled with nitrogen gas.

2.2.2.3 Characterizations

The morphology of the structures was examined by SEM (NOVA NANOSEM 230 FESEM, 15kV), TEM (JEM-2100, 200kV). The powder diffraction data were obtained using a Rigaku Co. High Power X-Ray Diffractometer D/MAZX 2500V/PC from 20^{o} to 80^{o}. Optical properties measurement (Absorbance, Reflection, Transmission) of structures were investigated by UV-visible spectroscopy (VARIAN, Cary 100). The diffuse reflection was measured using a Cary 5000 UV/Vis/NIR. Photoluminescence (PL) spectrum of the CdSe/H-TiO_2 was measured by spectrofluorometer (JASCO, FP-8500). Photoconversion efficiency was confirmed using IPCE measurement system (QEX10, Pv measurements).

2.2.2.4 PEC measurements

The PEC performance of the TiO_2 electrodes was exploited in a three-cell electrode system under front-side illumination of AM 1.5 G (Newport solar simulator) using a potentiostat (Princeton Applied research VersaSTAT3, AMETEK). An Ag/AgCl electrode and a Pt mesh were used as reference and counter electrodes, respectively. A solution of 0.24 M Na_2S and 0.35 M Na_2SO_3 was used as an electrolyte and sacrificial solution. An exposed area of the working electrode was 0.25 cm^2. The photoresponse was evaluated under chopped illumination from a Newport solar simulator equipped with an AM 1.5 G filter, calibrated with a standard Si solar cell simulating AM 1.5 G. The power of the solar simulator was measured to be 100 mW/cm^2. Photocurrent stability tests were carried out by measuring the photocurrent produced under chopped light irradiation (light/dark cycles of 10 s) at a bias of 0.5 V versus Ag / AgCl. The PEC performances in the visible range were acquired by the solar simulator coupled with a UV cutoff filter ($\lambda > 420$ nm). EIS measurement were performed under the same condition of gas evolutions under illumination of AM 1.5 G.

2.2.2.5 Calculation of effective refractive index of antireflection layer

The volume ratio of TiO_2 : air = 0.46 : 0.54 from the SEM image. On the basis of the effective medium theory,[2, 3] the effective refractive index n_{AR} can be calculated as 1.629 by the following equation

$$\mathbf{n_{AR} = \left[0.46 \times \left(n_{TiO_2}\right)^{q} + 0.54 \times (n_{air})^{q}\right]^{\frac{1}{q}}, \quad q = 2/3}$$

Here, n_{TiO_2} is 2.488 for anatase and n_{air} is 1.

2.2.3 Results and discussion

H-TiO_2 was fabricated by the following four steps, as shown in **Figure 2.2.1a**. First, surface-activated polystyrene beads (PS) obtained by treatment with Triton X-100 were self-assembled using Colvin's method[34] into a few layers of a hexagonal structure on a FTO substrate with a thickness of 1 μm.

PS structures were infiltrated with a $TiCl_4$ aqueous solution and annealed in an air condition, inducing gelation of a TiO_2 sol and calcination of PS simultaneously, and thus forming the TIO structure (I). Second, a surface textured titanium inverse opal (st-TIO, II) coated with a diameter of 7 nm TiO_2 mesoporous structures was created by selective removal of triblock copolymer domains from the coated layer containing TiO_2 precursors and block copolymers on TIO. In principle, the st-TIO has been designed to minimize the loss of surface area for reaction sites while achieving a photon trapping effect. Third, P25 mesoporous structures (III) were deposited onto the st-TIO with a thickness of 5 μm. Fourth, a top-patterned mesoporous P25 nanostructure (p-P25, IV) was created by imprinting using a 500 nm thick PDMS mold with 500 nm diameter and 600 nm pitch square patterns followed by the sintering process. The targeted structure is H-TiO_2, composed of a 4.5 μm thick mesoporous TiO_2 layer with a double sided energy harvesting layer comprising a 1 μm-thick st-TIO layer of a few hundred nanometer scale on the bottom and a 500 nm thick mesoporous TiO_2 square pattern on the top, giving a total thickness of 6 μm. **Figure 2.2.1b** is a scanning electron microscopy (SEM) image of the st-TIO structure (II) with air holes with a diameter of 290 nm. The dimension of the TIO was determined so as to efficiently scatter light for maximized light trapping as optimized in our previous reports.[29, 33, 35] **Figure 2.2.1c** is a SEM image of patterned mesoporous TiO_2 structures obtained by stamping a P25 layer using the PDMS molds followed by final sintering. The dimensions were fixed for the maximized AR effects, based on the previous reports.[28, 29] The volume fraction of TiO_2 in the AR layer is found to be 0.46 based on SEM imaging and the effective refractive index of the AR layer is 1.62 as calculated in the *Experimental procedures* part. **Figure 2.2.1d** is a cross-sectional image of the H-TiO_2 photoanode (V) sandwiched by a thin upper-layer of AR and a photon trapping under-layer. The surface area of the 6 μm-thick H-TiO_2 obtained by BET was 119 m^2/g, which is comparable to that of a compact mesoporous TiO_2-nanocrystalline film (117 m^2/g), as shown in **Figure 2.2.2**. **Figure 2.2.1e** illustrates the engineering mechanism of absorbed light to maximize the intensity of the light. When compared to a conventional P25 electrode, wherein a large portion of light is not only reflected but also limited to having a single pass through the device, H-TiO_2 offers a much improved mechanism for light harvesting. Here, the double sided-large dimension structures function as a mirror at both ends: maximally absorbed photons by the help of the AR layer on the top, simultaneously acting as a total internal reflection barrier due to the higher index of TiO_2 than air when back scattered light propagates from TiO_2 to the air side, are scattered further by the st-TIO frame on the bottom, permitting effective light harvesting via multi-passes of entrapped photons through the entire device.

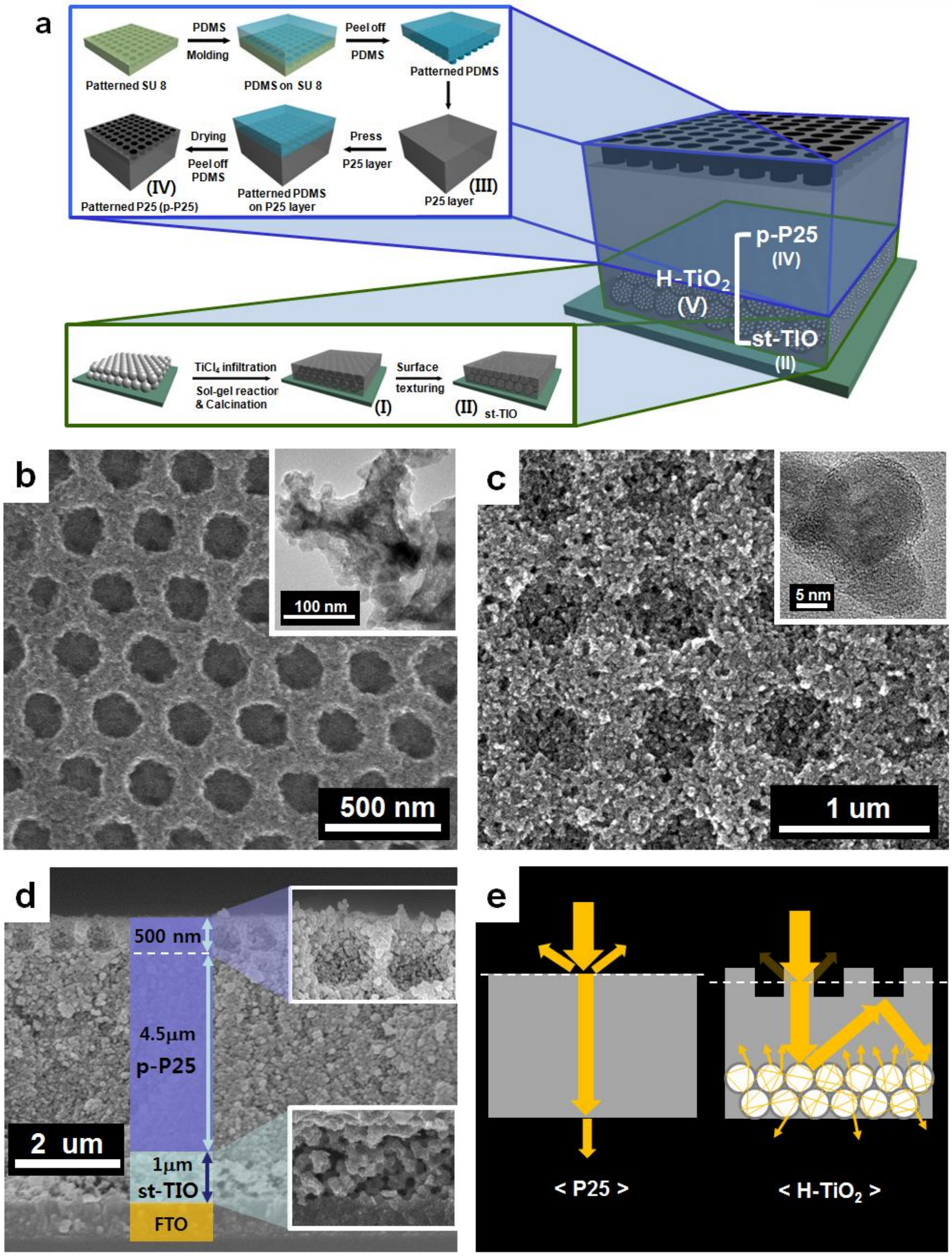

Figure 2.2.1 Schematic illustrations and electron microscopy images of TiO_2 structures. (a) Schematic illustration of the fabrication process for the hybrid TiO_2 structure (H-TiO_2). (b) Top view SEM image of st-TIO for photon trapping. The inset shows transmittance electron microscopy (TEM) image of the mesoporous surface textured-TIO (st-TIO). (c) Top view SEM image of the patterned mesoporous TiO_2 layer for anti-reflection. The inset shows the close-up image of the P25 particles. (d) Cross-sectional SEM image of H-TiO_2. (e) Schematic illustration of pathway of incoming light engineered by H-TiO_2 compared with the case of P25.

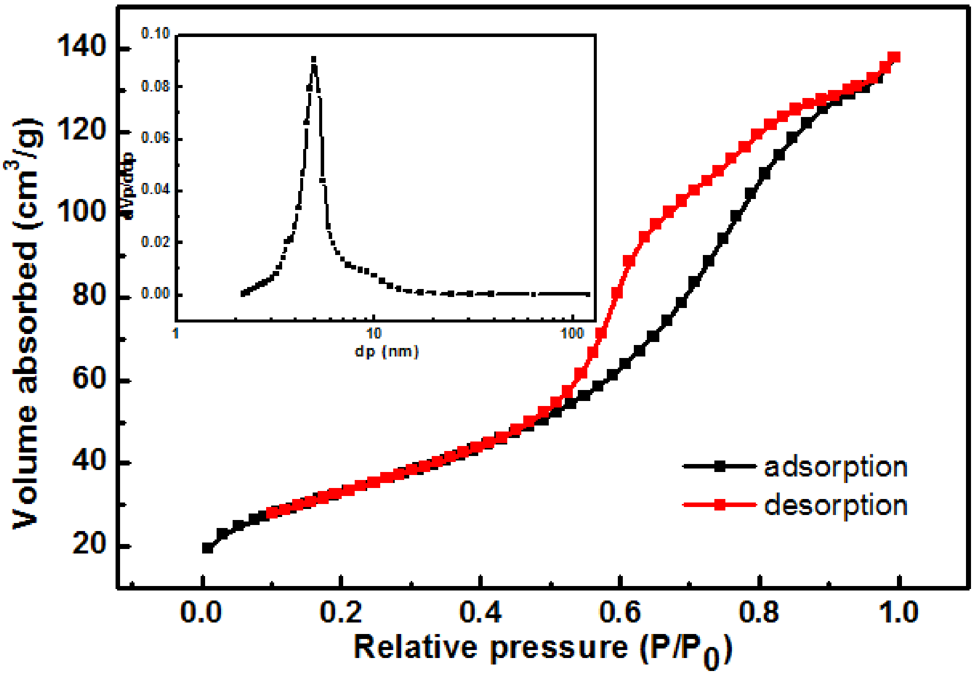

Pore size (nm)	7.162
Pore volume (cm^3 g^{-1})	0.216
Surface area (m^2 g^{-1})	119.038

Figure 2.2.2 BET analysis of H-TiO_2. The inset is pore-size distribution curve. The specific values are summarized in the table.

The enhanced AR property and photon trapping effects due to coupling of properly designed double-sided light harvesting layers can be quantified by the (specular angle) reflection spectra and diffuse reflection spectra, respectively. The reflection spectra were obtained by shining light from a 5 μm thick pure P25 and 5 μm top-surface patterned mesoporous P25 (p-P25) composed of 4.5 μm-thick P25 and an upper layer of patterns with a diameter of 500 nm and 500 nm thickness. P25 was chosen as a control sample since it has been shown to have excellent features as a working electrode in photovoltaic devices. In this configuration, the light passes through air/(TiO_2 patterns)/nanocrystalline TiO_2 interfaces from air to the TiO_2 nanocrystalline layer, and it is assumed that the majority of reflectance originates from the interface of air (n=1) and TiO_2 (n=2.49) due to the notable difference of the refractive index. **Figure 2.2.3a** shows that p-P25 gives ~ 20% lower reflectance as compared to the pure TiO_2 structure over the entire spectral range. This implies that much more light is able to participate in the photoconversion process in p-P25. This is attributable to the gradual change in the refractive index between the air and TiO_2 nanocrystalline layers in p-P25 (1/1.63/2.49, n_{AR} = 1.63 as calculated in the *Experimental procedures*), since the porosity of the patterned TiO_2 layer can modulate the effective refractive index of the diffraction grating layer.[29, 36, 37] In order to investigate the intensity of scattered light under beam irradiation on the device, the diffuse reflectance spectra of 6 μm-thick TiO_2 films made in the form of P25, P25/st-TIO, and H-TiO_2 were measured as shown in **Figure 2.2.3b**. A schematic illustration of the samples is shown in **Figure 2.2.3e**. Interestingly, compared to the pristine P25 film, both films with a 1μm-thick st-TIO layer (P25/st-TIO and H-TiO_2) showed significantly higher diffuse reflection spectra in the visible spectrum of light (380 - 800 nm), indicating that the absorbed light was efficiently scattered within the nanostructure film. The effect of introduction of the light harvesting layers into the P25 film was further exploited by the transmittance spectra by shining light from top to bottom (**Figure 2.2.3c**). As expected from the low absorption coefficient of P25 in the visible region, a significant fraction of the light passes through 6 μm-thick P25 at the longer wavelength range, which clearly shows light harvesting did not occur (black curve). However, when a 1 μm-thick st-TIO layer was introduced into 5 μm-thick P25 on the bottom, creating 6 μm-thick hybrid samples (blue and red curves), the transmission of light is greatly reduced, indicating that most of the light is re-absorbed by the structure in the devices. This is ascribed to the introduction of a few hundred nanometer scale structure as the photon trapping layer. Finally, UV-visible spectroscopic measurements were undertaken in order to explore the ultimate optical response of nanostructured TiO_2 with and without light harvesting layers. **Figure 2.2.3d** shows the UV-visible absorption spectra of an all 6 μm-thick plain P25, p-P25, P25/st-TIO, and H-TiO_2 illuminated at normal incidence from the air side. The absorption peaks spanning from 350 to 400 nm were assigned to the absorption of the conventional TiO_2 nanoparticles. An intense and wider spectrum with a broad absorption band ranging from 400 to 800 nm compared to pure P25 is achieved when either a top or bottom light harvesting layer is adopted. Notably, st-TIO contributed more to increment of the absorption band than anti-reflective p-P25 layer, implying the greater influence of photon trapping effects than AR effects on light harvesting. Conclusively, when the double sided layer is applied, greatly enhanced UV spectra in the visible range are observed, even though the density of TiO_2 particles is lower than that of P25. The enhanced UV absorption of H-TiO_2 is attributed to the synergetic combination of AR and photon trapping effects obtained by the larger dimension nanostructures, which allow for longer effective light path lengths and thus create a clear and strong absorption band in the longer wavelength region ranging from 400 nm to 800 nm.

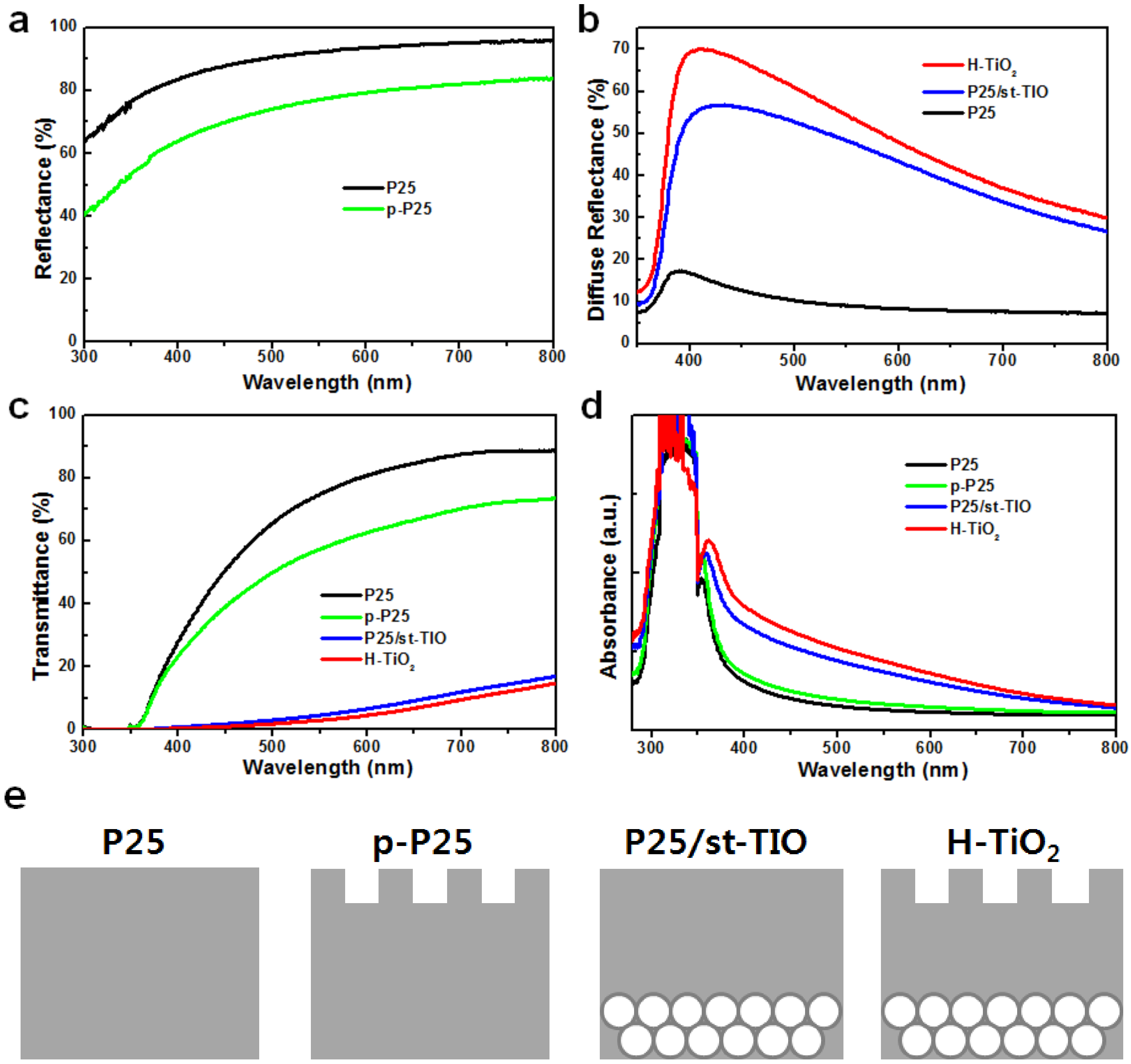

Figure 2.2.3 Optical properties of P25, p-P25, P25/st-TIO, and H-TiO_2 (p-P25/st-TIO). (a) Reflectance spectra recorded, within the UV-visible light wavelength range, on the pure P25 and top-surface patterned P25 (p-P25). (b) Diffuse reflectance spectra of P25, P25/st-TIO, and H-TiO_2, (c) Transmittance spectra, (d) UV-visible absorption spectra, and (e) Schematic illustration of P25, p-P25, P25/st-TIO, and H-TiO_2.

In order to further enhance the working capability of H-TiO_2 in the visible wavelength region, CdSe quantum dots (QDs) were deposited onto the H-TiO_2 structure. The deposition of CdSe on TiO_2 was carried out via 20 cycles of successive ionic layer adsorption and reaction (SILAR) method. **Figure 2.2.4a** presents TEM images of the CdSe QDs deposited onto H-TiO_2. Slightly randomly deposited spherical QDs with an average particle size of 5 nm with lattice spacings of 0.35 and 0.20 nm, which are consistent with the known values for the (002) and (103) planes of CdSe are observed. The enhanced optical properties due to the introduction of QDs on the hybrid samples are compared with the properties observed for CdSe/P25 and pure H-TiO_2 in **Figure 2.2.4b**. An apparent increase and broadening in the optical density near the band gap of CdSe covering a range of 400 - 800 nm confirms the creation of CdSe nanoparticles and the ability of QD sensitization. It should be noted that the overlap of the excitation wavelength of QDs and the regions of the wavelength with great absorption of H-TiO_2 is crucial to maximize the efficient sensitization of QDs. CdSe/P25 also presents enhanced absorption after the deposition of CdSe, yet with a much lower absorption coefficient than that of CdSe/H-TiO_2, likely due to low absorption of pristine P25 in the visible region where CdSe is excited. **Figure 2.2.4c** presents photoluminescence (PL) spectra of the CdSe QDs and CdSe/H-TiO_2. Compared to the PL spectrum of CdSe, which shows a typical near-band-edge emission at 630 nm, that of CdSe/H-TiO_2 is remarkably quenched. This clearly indicates a facile electron transfer mechanism at the interface between CdSe and TiO_2 nanoparticles, and thus low likelihood of electron-hole recombination within CdSe.

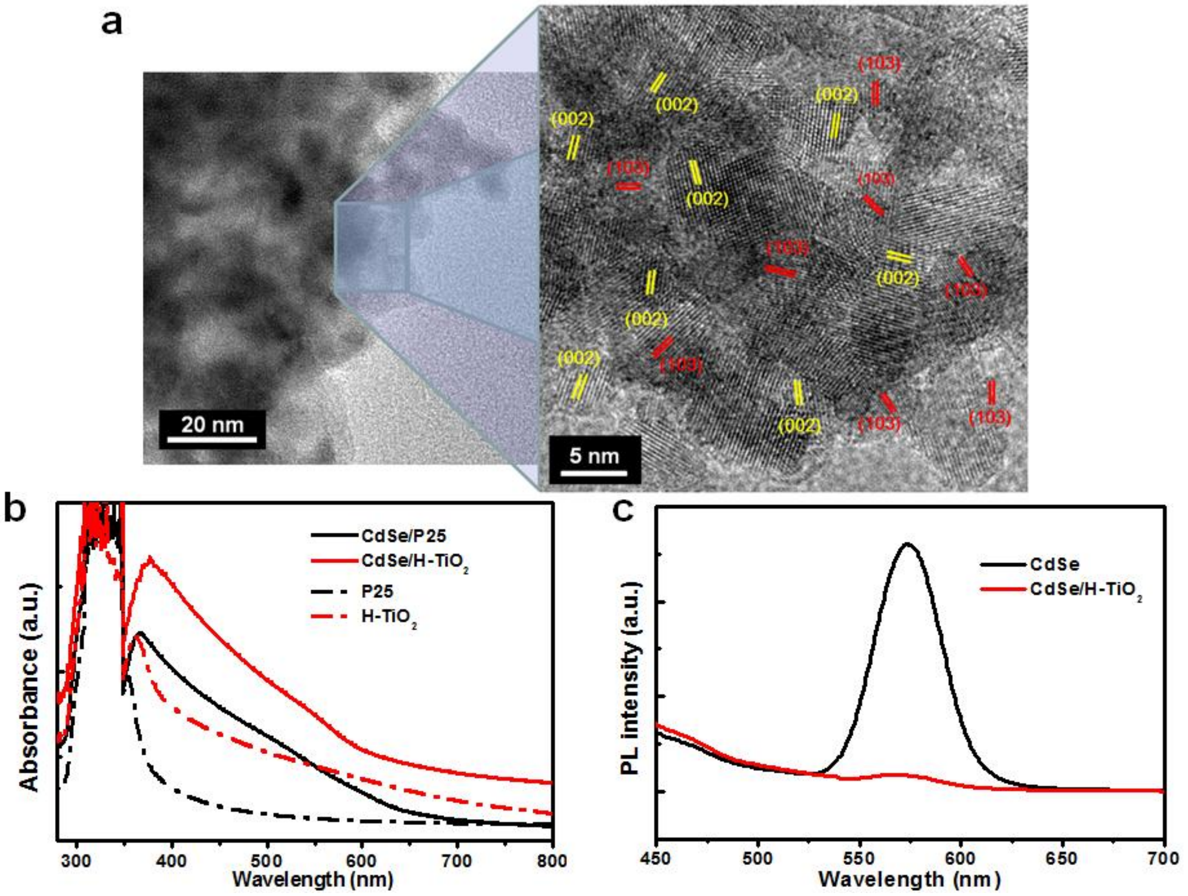

Figure 2.2.4 Characterization of quantum dots: (a) TEM images of CdSe/H-TiO$_2$. The image in the right panel is a close-up image of the rectangular area of the left image. (b) UV absorption spectra of P25 and H-TiO$_2$ before and after the deposition of CdSe. (c) Photoluminescence spectra of CdSe and CdSe/H-TiO$_2$.

In order to investigate the hydrogen generating efficiency of the samples, photo-electrochemical measurements were carried out on a P25 control sample, p-P25, P25/st-TIO, H-TiO_2, and CdSe/H-TiO_2 using Ag/AgCl, a Pt mesh, and as-prepared samples as a reference electrode, counter electrode, and working electrode, respectively, in a 0.24 M Na_2S and 0.35 M Na_2SO_3 electrolyte solution. This solution is commonly used as an electrolyte for quantum dot-based PEC systems, serving as the sacrificial agent. As shown in **Figure 2.2.5a**, which illustrates the electron transfer mechanism of CdSe/H-TiO_2, after the excited electrons are transferred from quantum dots to the conduction band of TiO_2, the electrons are withdrawn to the counter electrode where the hydrogen generation reaction occurs (An image capturing a large amount of H_2 gas generation is presented in **Figure 2.2.6** along with a movie clip).[38, 39] Meanwhile, the holes diffused to the surface of TiO_2 or CdSe oxidize S^{2-} and SO_3^{2-}. **Figure 2.2.5b** presents linear sweep voltammograms of the pristine P25, p-P25, P25/st-TIO, and H-TiO_2, which is described by the direct photoexcitation of electrons from the valence band of TiO_2, under AM 1.5 G simulated sunlight illumination (100 mW/cm^2). All samples with a light harvesting layer show higher photocurrent density than the P25 control sample. Surprisingly, the photocurrent density of an optimized H-TiO_2 reaches ~ 1.65 mA/cm^2 at an applied bias of 0.5 V,[40] which is approximately 2.5 times greater than that of the P25 control sample. This is the highest reported value of current density achieved using a single TiO_2 electrode material, implying that our approach to maximize light harvesting via engineering structural control is successful and also suggesting massive potential of pristine H-TiO_2 in photoconversion systems. **Figure 2.2.5c** compares linear sweep voltammograms of CdSe/H-TiO_2 and CdSe/P25. When the system is further supported by QD sensitization, the photocurrent density of CdSe/H-TiO_2 reaches ~ 16.2 mA/cm^2, 35% higher than that obtained with CdSe/P25, under illumination of 100 mW/cm^2. More surprisingly, as shown in **Figure 2.2.5c**, the photocurrent density of CdSe/H-TiO_2 created by only visible light illumination (blue curve, AM 1.5, a cutoff filter (>420 nm)) reaches ~ 14.2 mA/cm^2, ~ 88 % of that of UV-visible irradiation (red curve) and comparable to the values under UV-visible irradiation in other detailed studies,[41-43] clearly indicating solely visible working capability of CdSe/H-TiO_2. This surprising result is ascribed to the large enhancement of absorption of H-TiO_2 in the visible range, which matches well with the excitation wavelength of CdSe, via efficient light harvesting. **Figure 2.2.5d** shows the photoresponse over time (J-t curve) of CdSe/H-TiO_2 measured at 0.5 V with chopped illumination of AM 1.5 at a rate of 10 s exposure followed by 10 s non-illumination for UV-visible and visible light. The sharp spike in the photocurrent for both cases during the on/off illumination cycles indicates fast transport of photogenerated electrons from QDs to the current collector via the interior TiO_2 networks in accordance with the result of the PL study (**Figure 2.2.4c**). The greater values in the photocurrent density of CdSe/H-TiO_2 than in that of CdSe/P25 can be confirmed by a lower internal resistance measured by the electrochemical impedance spectroscopy (EIS). The measurement was conducted at a frequency range from 100 kHz to 0.1 Hz under open circuit voltage conditions, which provides the curves composed of two semicircles. A small (first) semicircle at a high frequency represents the charge transfer resistance at the interfaces of the electrolyte / Pt counter electrode whereas a large (second) semicircle at an intermediate frequency conveys the transport resistance of electrons at the TiO_2/QD/electrolyte interface.[44] A much smaller diameter of the second semicircle in CdSe/H-TiO_2 indicates a lower interfacial charge transfer resistance between the TiO_2 electrode and electrolytes and thus a more effective separation of photo-generated electron-hole pairs (a faster interfacial charge transfer to the electron donor/acceptor). The incident photon-to-electron conversion efficiency (IPCE) of CdSe/H-TiO_2 exhibits overall higher values than that of CdSe/P25 with a maximum IPCE value of 70.1% (43.7% for CdSe/P25) at 575 nm, as shown in **Figure 2.2.5e**. Importantly, much stronger and broader responses of CdSe/H-TiO_2 were achieved than those of CdSe/P25 from 400 to 630 nm, clearly indicating that CdSe/H-TiO_2 offers superior quantum efficiency in water splitting in the visible region via light harvesting.

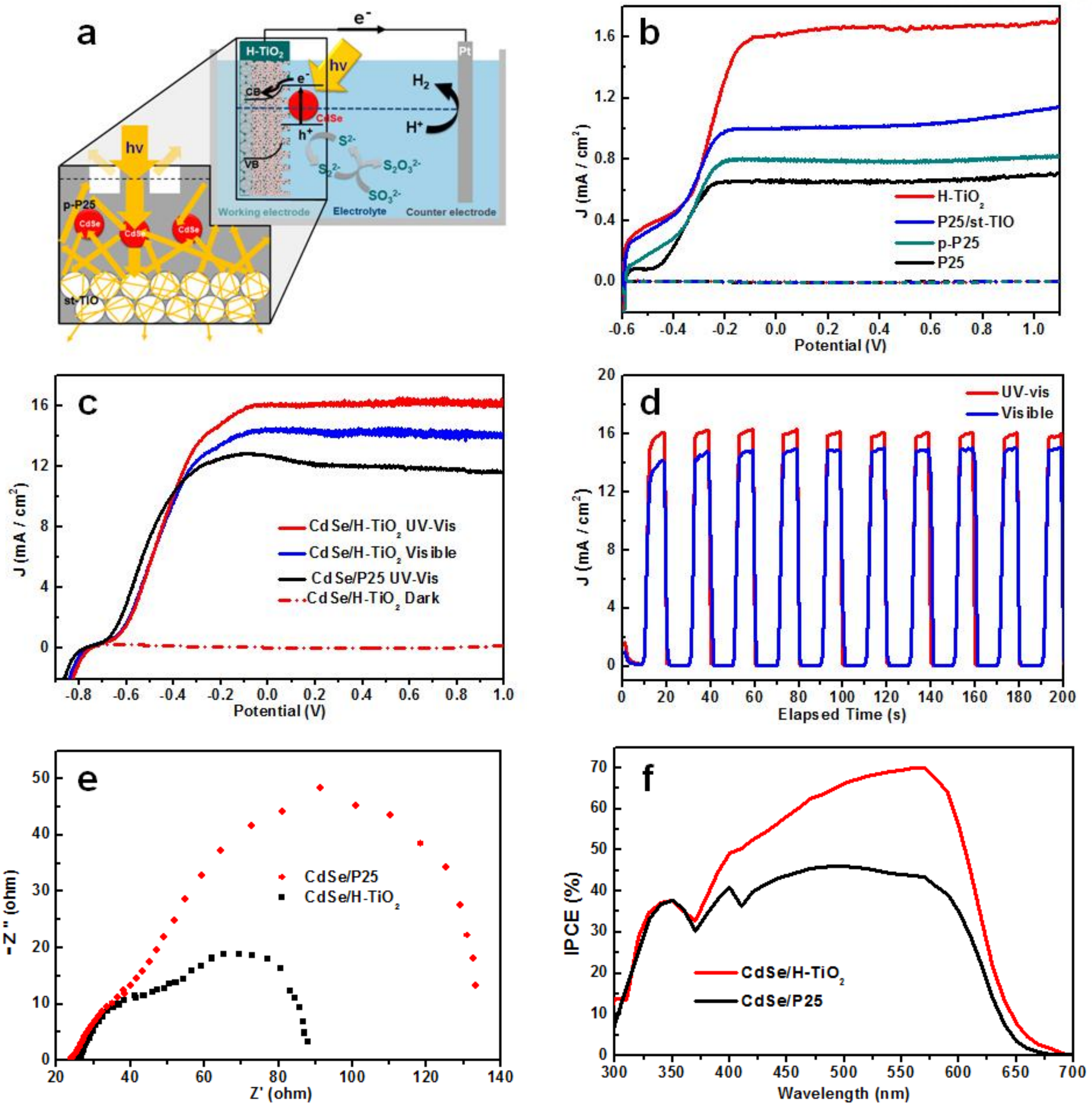

Figure 2.2.5 Schematic diagram and photocurrent response of P25 control, CdSe/P25, H-TiO$_2$, and CdSe/H-TiO$_2$ under AM 1.5 illumination (100 mW/cm^2). (a) Schematic diagram showing the hydrogen generating mechanism of CdSe/H-TiO$_2$ (b) Linear sweep voltammetry measurements of P25, p-P25, P25/st-TIO, and H-TiO$_2$ under UV-visible and dark conditions. (c) Linear sweep voltammetry measurements of CdSe/P25 and CdSe/H-TiO$_2$ under UV-visible, visible light illumination, and dark conditions. (d) J-t curve of CdSe/H-TiO$_2$ at a bias of 0.5 V under UV-visible and visible light illumination. (e) EIS response of P25 and H-TiO$_2$. The measurement was conducted at a frequency range from 100 kHz to 0.1 Hz under open circuit voltage conditions. (f) Measurement of the incident photon-to-electron conversion efficiency. All experiments were performed with a 0.24 M Na$_2$S and 0.35 M Na$_2$SO$_3$ electrolyte (pH = 12) and 100 mW/cm^2 xenon lamp coupled with a UV/IR filter as the light source.

Figure 2.2.6 Experimental setup for PEC measurements showing the presence of a large bubble created from the aggregation of a large amount of H_2 bubbles near the Pt counter electrode. The movie clip is included.

2.2.4 Conclusion

In conclusion, we report a finely designed H-TiO_2 structure that maximizes light harvesting triggered by the configuration of a double sided layer with a few hundred nanometer scale while retaining the sufficient surface area. The observed optical properties confirm excellent light harvesting effects in the H-TiO_2 structure, which can facilitate the water splitting reaction of a TiO_2 semiconductor in the UV-visible range. The photocurrent of CdSe/H-TiO_2 (~ 16.2 mA/cm^2) was 35% greater than that of the representative CdSe/P25 photoelectrode, which is clearly recognized for outstanding performance. Importantly, CdSe/H-TiO_2 under filtered exposure (λ > 420 nm) conditions recorded current density of ~ 14.2 mA/cm^2, the highest value in the visible range, which is attributable to the overlap of the excitation wavelength of CdSe with the wavelength where light harvesting is observed. The excellent performance of CdSe/H-TiO_2 suggests that this strategy can provide a novel route to design photoactive materials via systematic engineering of light for maximum photoconversion efficiency.

2.2.5 References

1. M. G. Walter, E. L. Warren, J. R. McKone, S. W. Boettcher, Q. Mi, E. A. Santori and N. S. Lewis, Solar water splitting cells. *Chemical Reviews* **110**, 6446-6473 (2010).
2. X. Chen, S. Shen, L. Guo and S. S. Mao, Semiconductor-based photocatalytic hydrogen generation. *Chemical Reviews* **110**, 6503-6570, (2010).
3. Y. J. Hwang, C. Hahn, B. Liu and P. D. Yang, Photoelectrochemical properties of TiO_2 nanowire arrays: a study of the dependence on length and atomic layer deposition coating. *ACS Nano* **6**, 5060-5069 (2012).
4. N. Chouhan, C. Chen, W.-S. Chang, K.-W. Cheng and R.-S. Liu, photoelectrochemical cells for hydrogen generation. *Electrochemical Technologies for Energy Storage and Conversion* 541-599 (2011).
5. J. Luo, S. K. Karuturi, L. Liu, L. T. Su, A. I. Tok and H. J. Fan, Homogeneous photosensitization of complex TiO_2 nanostructures for efficient solar energy conversion. *Scientific Reports* **2**, 451 (2012).
6. A. Brune, G. Jeong, P. A. Liddell, T. Sotomura, T. A. Moore, A. L. Moore and D. Gust, Porphyrin-Sensitized Nanoparticulate TiO_2 as the Photoanode of a Hybrid Photoelectrochemical Biofuel Cell. *Langmuir* **20**, 8366-8371 (2004).
7. H. Kisch, Semiconductor photocatalysis—mechanistic and synthetic aspects. *Angewandte Chemie International Edition* **52**, 812-847 (2013).
8. Y. Lu, H. Yu, S. Chen, X. Quan and H. Zhao, Integrating plasmonic nanoparticles with TiO_2 photonic crystal for enhancement of visible-light-driven photocatalysis. *Environmental Science & Technology* **46**, 1724-1730 (2012).
9. I. Paramasivam, H. Jha, N. Liu and P. Schmuki, A Review of photocatalysis using self-organized TiO_2 nanotubes and other ordered oxide nanostructures. *Small* **8**, 3073-3103 (2012).
10. W. Fan, Q. Zhang and Y. Wang, Semiconductor-based nanocomposites for photocatalytic H_2 production and CO_2 conversion. *Physical Chemistry Chemical Physics* **15**, 2632-2649 (2013).
11. L. T. Su, S. K. Karuturi, J. Luo, L. Liu, X. Liu, J. Guo, T. C. Sum, R. Deng, H. J. Fan, X. Liu and A. I. Y. Tok, Photon upconversion in hetero-nanostructured photoanodes for enhanced near-infrared light harvesting. *Advanced Materials* **25**, 1603-1607 (2013).
12. S. Bingham and W. A. Daoud, Recent advances in making nano-sized TiO_2 visible-light active through rare-earth metal doping. *Journal of Materials Chemistry* **21**, 2041-2050 (2011).
13. T. Kamegawa, S. Matsuura, H. Seto and H. Yamashita, A visible-light-harvesting assembly with a sulfocalixarene linker between dyes and a Pt-TiO_2 photocatalyst. *Angewandte Chemie International Edition* **52**, 916-919 (2013).
14. Z. Xu and J. Yu, Visible-light-induced photoelectrochemical behaviors of Fe-modified TiO_2 nanotube arrays. *Nanoscale* **3**, 3138-44 (2011).
15. J. H. Park, S. Kim and A. J. Bard, Novel carbon-doped TiO_2 nanotube arrays with high aspect ratios for efficient solar water splitting. *Nano Letters* **6**, 24-28 (2006).

16. Z. G. Xiong and X. S. Zhao, Nitrogen-doped titanate-anatase core-shell nanobelts with exposed {101} anatase facets and enhanced visible light photocatalytic activity. *Journal of American Chemical Society* **134**, 5754-5757 (2012).
17. J. Lee, S. Mubeen, X. Ji, G. D. Stucky and M. Moskovits, Plasmonic photoanodes for solar water splitting with visible light. *Nano Letters* **12**, 5014-5019 (2012).
18. MurdochM, G. I. N. Waterhouse, M. A. Nadeem, J. B. Metson, M. A. Keane, R. F. Howe, LlorcaJ and IdrissH, The effect of gold loading and particle size on photocatalytic hydrogen production from ethanol over Au/TiO_2 nanoparticles. *Nature Chemistry* **3**, 489-492 (2011).
19. H.-J. Ahn, P. Thiyagarajan, L. Jia, S.-I. Kim, J.-C. Yoon, E. L. Thomas and J.-H. Jang, An optimal substrate design for SERS: dual-scale diamond-shaped gold nano-structures fabricated via interference lithography. *Nanoscale*. **5**, 1836-1842 (2013).
20. M.-H. Jung and M. G. Kang, Enhanced photo-conversion efficiency of CdSe-ZnS core-shell quantum dots with Au nanoparticles on TiO_2 electrodes. *Journal of Materials Chemistry* **21**, 2694-2700 (2011).
21. C. Cheng, S. K. Karuturi, L. Liu, J. Liu, H. Li, L. T. Su, A. I. Y. Tok and H. J. Fan, Quantum-dot-sensitized TiO_2 inverse opals for photoelectrochemical hydrogen generation. *Small* **8**, 37-42 (2012).
22. G. Liu, L.-C. Yin, J. Wang, P. Niu, C. Zhen, Y. Xie and H.-M. Cheng, A red anatase TiO_2 photocatalyst for solar energy conversion. *Energy & Environmental Science* **5**, 9603-9610 (2012).
23. L. Liu, G. Wang, Y. Li, Y. Li and J. Zhang, CdSe quantum dot-sensitized Au/TiO_2 hybrid mesoporous films and their enhanced photoelectrochemical performance. *Nano Research* **4**, 249-258 (2011).
24. X. Chen, L. Liu, P. Y. Yu and S. S. Mao, Increasing solar absorption for photocatalysis with black hydrogenated titanium dioxide nanocrystals. *Science* **331**, 746-750 (2011).
25. S.-H. Lee, N. M. Abrams, P. G. Hoertz, G. D. Barber, L. I. Halaoui and T. E. Mallouk, Coupling of titania inverse opals to nanocrystalline titania layers in dye-sensitized solar cells. *The Journal of Physical Chemistry B* **112**, 14415-14421 (2008).
26. Z. Zhang, L. Zhang, M. N. Hedhili, H. Zhang and P. Wang, Plasmonic gold nanocrystals coupled with photonic crystal seamlessly on TiO_2 nanotube photoelectrodes for efficient visible light photoelectrochemical water splitting. *Nano Letters* **13**, 14-20 (2012).
27. S. Foster and S. John, Light-trapping in dye-sensitized solar cells. *Energy & Environmental Science* **6**, 2972-2983 (2013).
28. J. Kim, J. K. Koh, B. Kim, J. H. Kim and E. Kim, Nanopatterning of mesoporous inorganic oxide films for efficient light harvesting of dye-sensitized solar cells. *Angewandte Chemie International Edition* **51**, 6864-6869 (2012).
29. H.-J. Ahn, S.-I. Kim, J.-C. Yoon, J.-S. Lee and J.-H. Jang, Power conversion efficiency enhancement based on the bio-inspired hierarchical antireflection layer in dye sensitized solar cells. *Nanoscale* **4**, 4464-4469 (2012).
30. J. N. Munday and H. A. Atwater, Large integrated absorption enhancement in plasmonic solar cells by combining metallic gratings and antireflection coatings. *Nano Letters* **11**,

2195-2201 (2010).

31. K. X. Wang, Z. Yu, V. Liu, Y. Cui and S. Fan, Absorption enhancement in ultrathin crystalline silicon solar cells with antireflection and light-trapping nanocone gratings. *Nano Letters* **12**, 1616-1619 (2012).
32. Q. Zhang, E. Uchaker, S. L. Candelaria and G. Cao, Nanomaterials for energy conversion and storage. *Chemical Society Reviews* **42**, 3127-3171 (2013).
33. P. Thiyagarajan, H.-J. Ahn, J.-S. Lee, J.-C. Yoon and J.-H. Jang, Hierarchical metal/semiconductor nanostructure for efficient water splitting. *Small* **9**, 2341-2347 (2013).
34. V. L. Colvin, From opals to optics: colloidal photonic crystals. *MRS Bulletin* **26**, 637-641 (2001).
35. K. Kim, P. Thiyagarajan, H.-J. Ahn, S.-I. Kim and J.-H. Jang, Optimization for visible light photoelectrochemical hydrogen generation: gold-coated and surface-textured TIO nano-networks. *Nanoscale* **5**, 6254-6260 (2013).
36. D. G. Stavenga, S. Foletti, G. Palasantzas and K. Arikawa, Light on the moth-eye corneal nipple array of butterflies. *Proceedings of the Royal Society B: Biological Sciences* **273**, 661-7 (2006).
37. H. Li, B. Jiang, R. Schaller, J. Wu and J. Jiao, Antireflective photoanode made of TiO_2 nanobelts and a ZnO nanowire array. *The Journal of Physical Chemistry C* **114**, 11375-11380 (2010).
38. J. Luo, L. Ma, T. He, C. F. Ng, S. Wang, H. Sun and H. J. Fan, TiO_2/(CdS, CdSe, CdSeS) nanorod heterostructures and photoelectrochemical properties. *The Journal of Physical Chemistry C* **116**, 11956-11963 (2012).
39. J. Hensel, G. Wang, Y. Li and J. Z. Zhang, Synergistic effect of CdSe quantum dot sensitization and nitrogen doping of TiO_2 nanostructures for photoelectrochemical solar hydrogen generation. *Nano Letters* **10**, 478-483 (2010).
40. S. K. Karuturi, C. Cheng, L. Liu, L. Tat Su, H. J. Fan and A. I. Y. Tok, Inverse opals coupled with nanowires as photoelectrochemical anode. *Nano Energy* **1**, 322-327 (2012).
41. X.-F. Gao, W.-T. Sun, G. Ai and L.-M. Peng, Photoelectric performance of TiO_2 nanotube array photoelectrodes cosensitized with CdS/CdSe quantum dots. *Applied Physics Letters* **96**, 153104-3 (2010).
42. K. Shin, S. i. Seok, S. H. Im and J. H. Park, CdS or CdSe decorated TiO_2 nanotube arrays from spray pyrolysis deposition: use in photoelectrochemical cells. *Chemical Communications* **46**, 2385-2387 (2010).
43. M. Seol, J.-W. Jang, S. Cho, J. S. Lee and K. Yong, Highly efficient and stable cadmium chalcogenide quantum dot/ZnO nanowires for photoelectrochemical hydrogen generation. *Chemistry of Materials* **25**, 184-189 (2012).
44. M. Jung, and M. Kang, Enhanced photo-conversion efficiency of CdSe–ZnS core–shell quantum dots with Au nanoparticles on TiO_2 electrodes. *Journal of Material Chemistry* **21**, 2694-2700 (2011).
45. K. Kim, M.-J. Kim, S.-I. Kim and J.-H. Jang, Towards visible light hydrogen generation: quantum dot-sensitization via efficient light harvesting of hybrid-TiO_2, *Scientific Reports* **3**, 3330 (2013).

2.3 α-Fe_2O_3 on patterned fluorine doped tin oxide for efficient photoelectrochemical water splitting

Adapted with permission from ref. 29. Copyright 2015 Royal Society of Chemistry

2.3.1 Introduction

In the last decade, the generation of hydrogen gas has been extensively studied as a promising method for renewable green energy sources. Among its most attractive features are that it does not create byproducts of pollutants during the energy generation reaction and it can be directly applied as a fuel for combustion. Hydrogen gas can be easily obtained from water molecules via the photocatalytic process of water splitting in photoelectrochemical (PEC) systems. In order to enable PEC water splitting, a semiconductor material that can efficiently absorb the energy of sunlight is necessary. A variety of semiconductor photoanode materials (TiO_2[1-3], ZnO[4, 5], WO_3[6, 7], etc.) have been studied in the context of criteria such as cost effectiveness, chemical stability, and proper bandgap energy and band edge position in the energy diagram. As the PEC water splitting field has rapidly developed, interest in the working capability under visible light, which occupies nearly half of the portion of sunlight, has gradually increased. Materials that have small bandgap energy falling into the visible region thus have become essential for efficient water splitting systems.

α-Fe_2O_3 (hematite) has attracted a great deal of attention due to the advantages of a low bandgap energy of 2.1 ~ 2.2 eV, which covers the visible light range, and low cost, stability, and abundance.[8, 9] Despite these advantages, some factors that cause high recombination rates, such as short carrier lifetime (~ 1 ps)[10], poor light absorption near the band edge[11], and very short hole diffusion length ranging in a few nanometers[12, 13] must still be overcome. These problems have restricted the charge separation and charge collection properties accordingly, resulting in significantly degraded performance. To date, many strategies have been explored to overcome the aforementioned limitations of hematite for PEC devices by enhancing the electronic and optical properties; i.e. nanostructuring the photoelectrodes (nanotubes, nanowires, flower shape and inverse opal etc.)[14-18] and doping with some heteroatoms (Sn, Co and Ti etc.)[16, 19-21] etc. Alternatively, interlayer structures with better crystallinity between the current collector and the hematite structures were suggested for facile transport of electrons to the electrode.[22] Building a p-n junction at the interface of NiO/hematite[23] or silicon/hematite[24] helps deliver the generated electrons toward the current collector before recombination occurs. Several enhanced conductive materials such as antimony-doped tin oxide (ATO), gold, graphene, carbon nanotubes (CNTs) etc.[25-28] have been researched for the same reason.

Fluorine doped tin oxide (FTO) is a widely used transparent conducting electrode in photo-electronic systems such as solar cells and PEC water splitting because of its remarkable advantages in cost and chemical stability. Recently, patterned-FTO (p-FTO) having light scattering effects has been suggested as an efficient conducting layer in DSSCs (**Scheme 2.3.1**)[23].

We hypothesized that a three dimensional p-FTO structure could serve as not only a light scattering layer, but also a direct electron transporting network with very facile processes in a PEC water splitting system. It was found that a worm-like hematite structure coated on a p-FTO exhibits a photocurrent density of 1.88 mA/cm^2, a 1.7 times increase in comparison with a corresponding structure on an unpatterned FTO substrate.

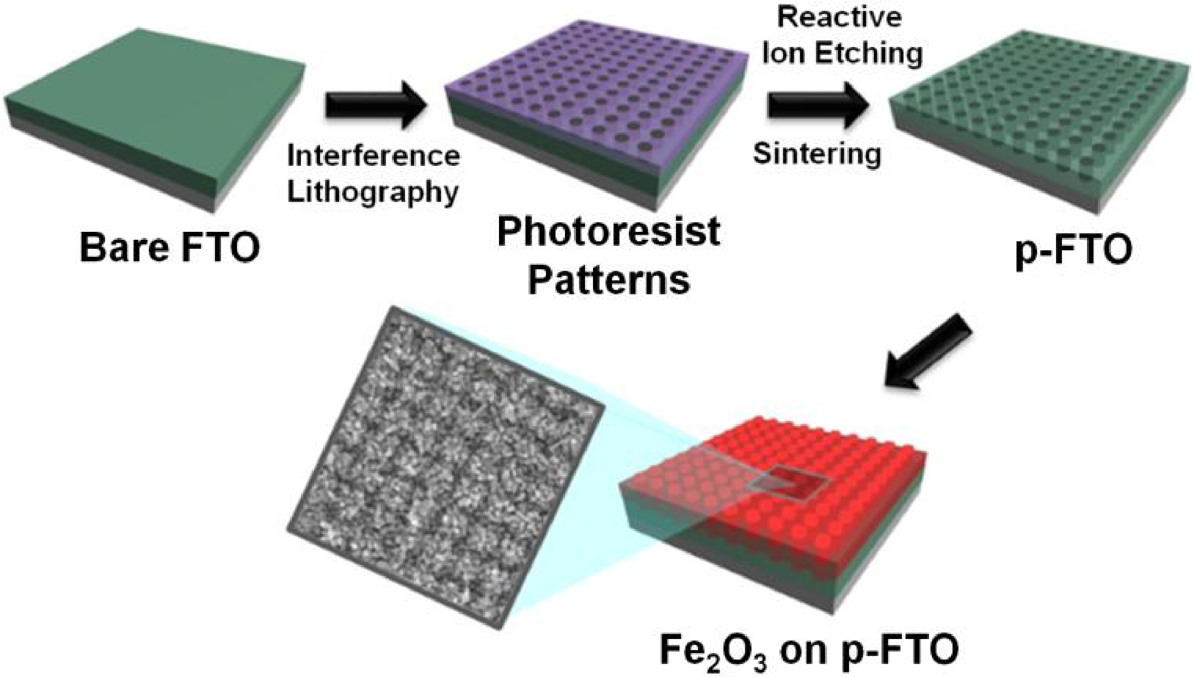

Scheme 2.3.1 Illustration for the fabrication of α-Fe_2O_3 on p-FTO.

2.3.2 Experimental procedures

2.3.2.1 Preparation of patterned FTO (p-FTO)

The FTO substrate was washed by sequential ultrasonication in acetone, isopropanol, deionized water, and ethanol for 10min. each followed by nitrogen blowing. A SU-8 solution (SU-8:CP = 1:2.25) was spin-coated on the cleaned FTO at 3000 rpm for 30 s followed by prebaking on a hotplate at 100ºC for 30min. The photoresist-coated FTO was double-exposed under a 365 nm laser source to make square patterns via interference lithography. To determine the pitch distance and the hole diameter of the patterns, the angle of Lloyd's mirror and the time of exposure were varied. The exposed samples were post-baked on the hotplate at 70 ºC for 10 min. The unexposed regions were then removed in a propylene glycol monomethyletheracetate solution for a minute and washed in isopropyl alcohol for 30s, resulting in SU-8 square patterns.

Reactive ion etching (RIE) was performed to vertically etch FTO. The plasma was generated at a pressure of 40mTorr with a RF power of 300W. The gas pressure ratio of CF_4, CHF_3, Ar, and O_2 was around 2:9:1:1. p-FTO was created after removal of the residue of SU-8 by annealing at 500 ºC for an hour.

2.3.2.2 Preparation of the α-Fe_2O_3 on p-FTO

The fabrication of the worm-like α-Fe_2O_3 layer followed the procedure previously reported by this group.[1] 30 ml of a 150 mM $FeCl_3 \cdot 6H_2O$ aqueous solution was transferred into a Teflon-lined autoclave, and the substrates were reclined on the inside of the autoclave facing the p-FTO side to the wall. After 6hrs of reaction at 100 ºC, a uniform layer of FeOOH was formed on the p-FTO substrate. The substrates were thoroughly rinsed with D.I. water and ethanol. The samples were then annealed at 550 ºC in air for one hour to convert FeOOH to a hematite film. To enhance the crystallinity of hematite, the samples were further annealed at 800 ºC in air for 20 min.

2.3.2.3 PEC measurements

The PEC performance of α-Fe_2O_3 on p-FTO was explored in a three-cell electrode system under front-side illumination of AM 1.5G and 100 mW/cm^2 using 300W power from a Xe lamp. An Ag/AgCl (KCl sat.) electrode and a Pt mesh were used a reference and counter electrode, respectively. A solution of 1M NaOH (pH 13.6) was used as an electrolyte. The exposed area of the working electrode was set to be 0.25 cm^2 by making a window with scotch tape. Photocurrent stability tests were carried out by measuring the photocurrent produced under chopped light irradiation (light/dark cycles of 10s.) at a bias of 1.5 V vs. RHE. EIS was carried out at a frequency range from 100 kHz to 0.1 Hz.

2.3.3 Results and discussion

Patterned α-Fe_2O_3 was fabricated via three steps, as shown in **Scheme 2.3.1**. Square patterns of SU-8 were built on the pre-cleaned FTO via the interference lithography (IL) technique. p-FTO was created through reactive ion etching (RIE) of patterned SU-8 coated FTO using SU-8 patterns as a mask. The residues of the photoresists were removed by sintering at high temperature. The worm-like hematite was deposited on p-FTO by a method reported elsewhere.

The morphologies of p-FTO and patterned α-Fe_2O_3 on p-FTO are characterized by atomic force microscopy (AFM) and scanning electron microscopy (SEM) observations. The height and the pitch of the SU-8 patterns were about 400 nm and 560 nm, respectively, as shown in **Figure 2.3.1**. The morphology of p-FTO after RIE and the annealing steps to remove the residues of the SU-8 patterns is shown in **Figure 2.3.2a** and **2.3.2b**. The detailed conditions of the RIE process are provided in the experimental part of Supplementary Information. Uniform height and a clear hole shape were difficult to achieve due to the rough surface of bare FTO. **Figure 2.3.2c** shows the worm-like hematite layer with a similar overall morphology to that of p-FTO. The worm-like α-Fe_2O_3 is one of the well-known hematite structures that has shown excellent performance in PEC systems.[8] The patterned worm-like hematite materials were densely grown on p-FTO, as shown in **Figure 2.3.2c**, proving strong potential for a large surface area and light scattering caused by the interactions between the periodically aligned patterned-structure and the exposed light.

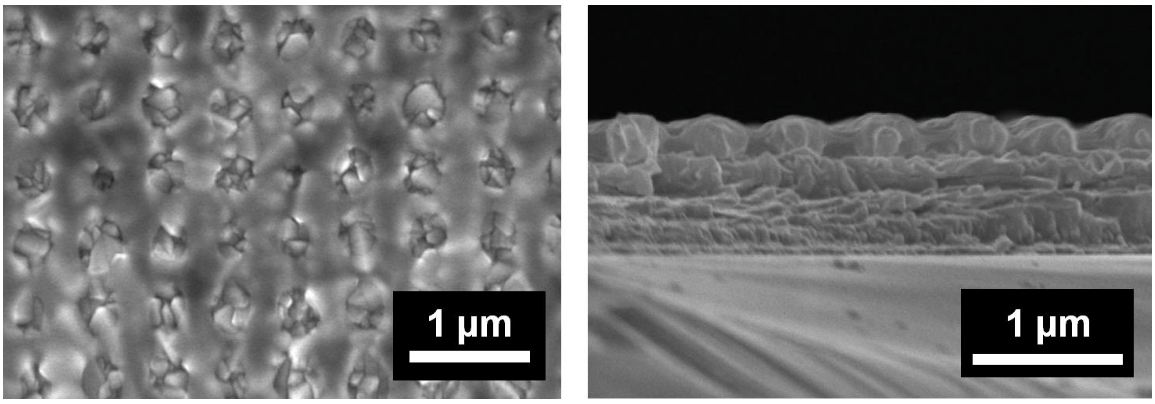

Figure 2.3.1 SEM images of SU-8 patterns on FTO; the top and cross-section view.

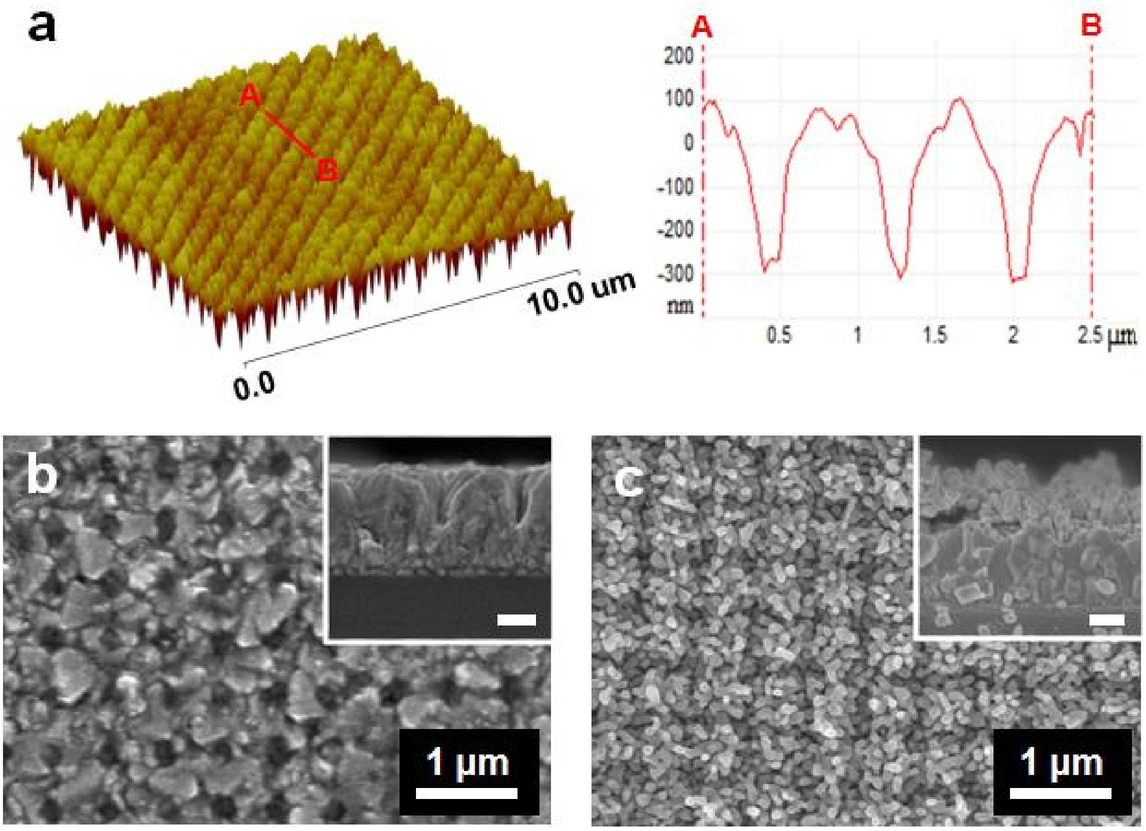

Figure 2.3.2 Atomic force microscope (AFM) and scanning electron microscope (SEM) images of p-FTO and patterned α-Fe_2O_3 on p-FTO. a) The three-dimensional surface morphology and the depth profile of p-FTO, b) Top view and side view of p-FTO (inset image, scale bar is 250 nm), and c) Top view and side view of α-Fe_2O_3/p-FTO (inset image, scale bar is 250 nm).

Figure 2.3.3 shows the optical properties of p-FTO through an analysis of the UV-visible spectroscopy results. The diffuse reflectance in **Figure 2.3.3a** compares the degree of light scattering of bare FTO and p-FTO. The 3D p-FTO improves light scattering effects in the visible range due to the nanostructures that interact well with the exposing light. It has been reported that the direction of incident light changes in a variety of ways when meeting different media. The effect can be larger with certain materials having a rough surface or periodic structure on a hundreds of nanometer scale and a large refractive index. The large intensity of light scattering accounts for the longer pathways of light in the structure, as shown in the schematic image (**Scheme 2.3.2**). The light absorbance is very important because it is strongly related with how much of the light is utilized for the generation of photocurrent in the PEC cells. Ultimately, the substantially enhanced light scattering effect of p-FTO with a three-dimensional structure improves the light absorption of the catalyst, and thus enhances the photocurrent under the UV-visible region. The greatly increased absorption of α-Fe_2O_3 coated on p-FTO compared with bare FTO over all wavelength regions is shown in **Figure 2.3.3b**.

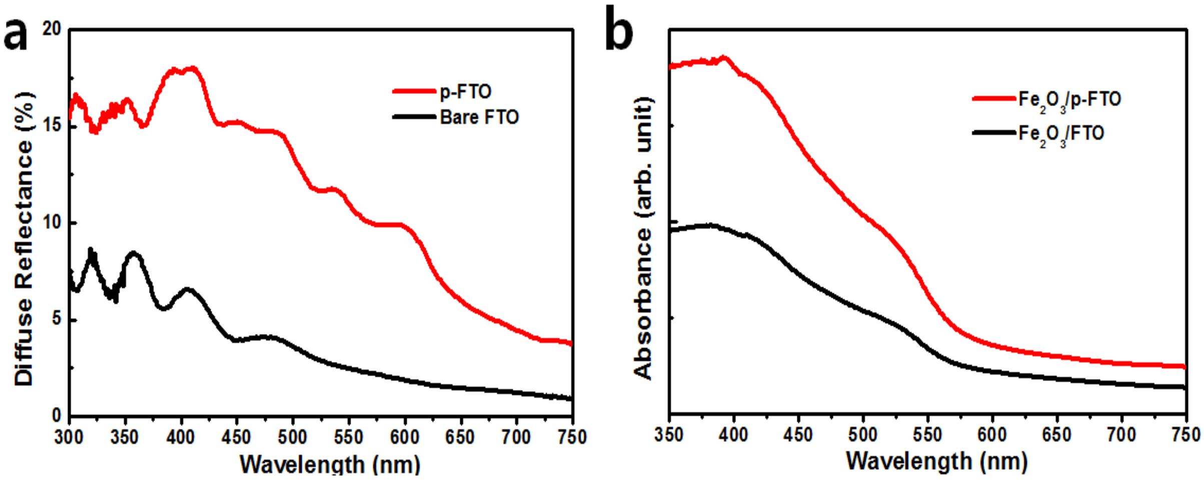

Figure 2.3.3 Optical properties of α-Fe_2O_3/bare FTO and α-Fe_2O_3/p-FTO: a) Diffuse reflectance and b) absorption spectra.

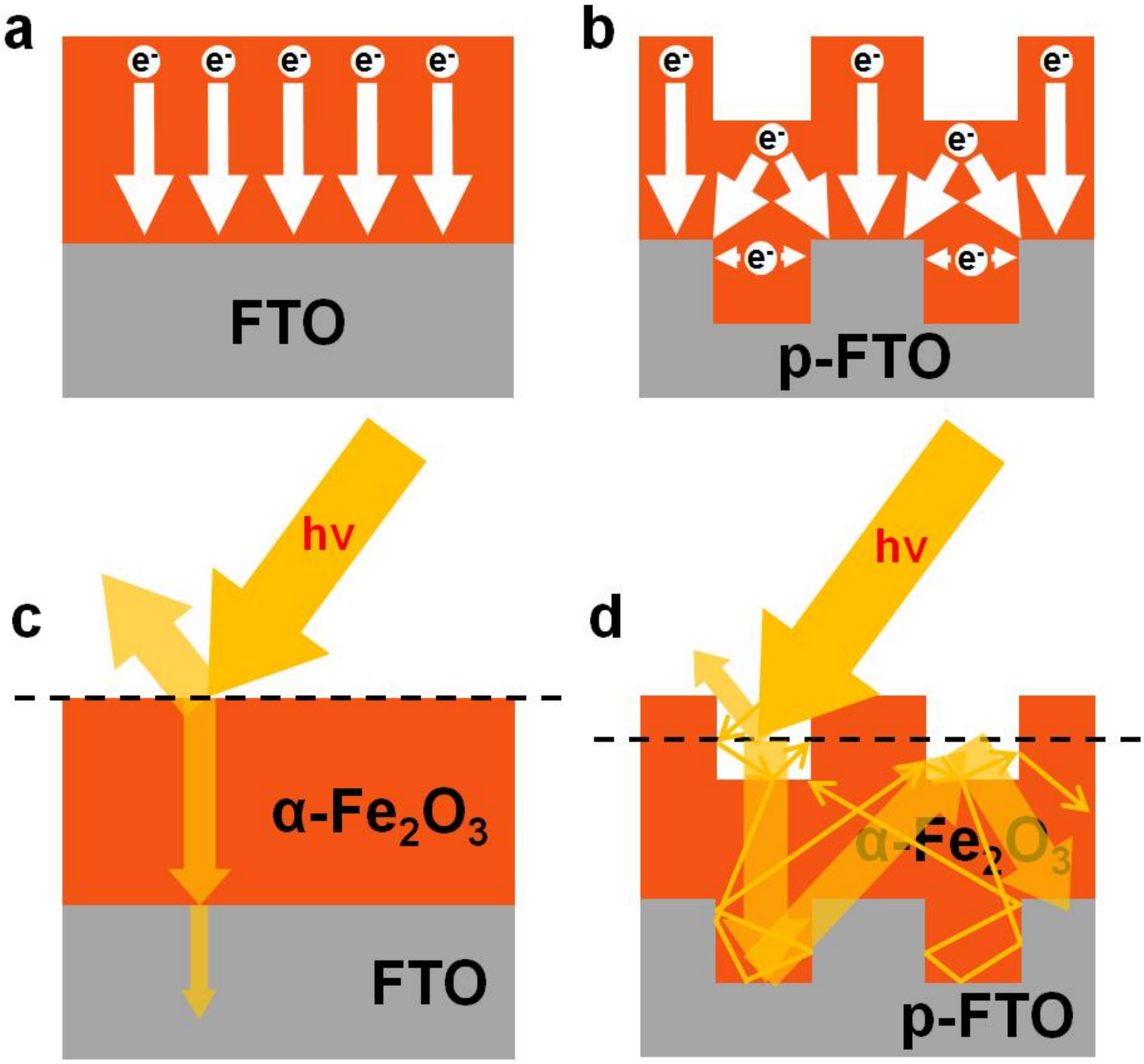

Scheme 2.3.2 Schematic diagrams that show a), b) the shorter migration pathway of the photogenerated electrons and c), d) the greater scattering of incident sunlight in α-Fe_2O_3/p-FTO than α-Fe_2O_3/bare FTO.

The photocurrent densities of α-Fe_2O_3 on bare FTO and p-FTO were measured at a potential range from 0.4 V to 2 V vs. RHE under AM 1.5 G simulated sunlight illumination, as shown in **Figure 2.3.4a**. α-Fe_2O_3/FTO and α-Fe_2O_3/p-FTO respectively had a photocurrent density of 1.1 mA/cm^2 and 1.88 mA/cm^2 at 1.5 V vs. RHE. Compared to the photocurrent density of α-Fe_2O_3, which is similar to the values reported in other α-Fe_2O_3 studies,[15] the value on p-FTO is 1.7 times higher under UV-visible light illumination. This improvement can be attributed to enhanced light absorption and rapid transfer of photogenerated electrons. p-FTO enables i) the light to have longer paths via efficient scattering, and thus enhanced absorption, and ii) photogenerated electrons to reach the current collector rapidly by providing a shorter migration length between α-Fe_2O_3 and the three-dimensional current collector substrate, as described in the schematic diagram (**Scheme 2.3.2**).

In order to explore the improved electron transfer behavior of α-Fe_2O_3/p-FTO, the EIS responses of α-Fe_2O_3/FTO and α-Fe_2O_3/p-FTO were measured in 1 M NaOH electrolyte at a frequency range from 100 kHz to 0.1 Hz under illumination of AM 1.5 G, as shown in **Figure 2.3.4b**. The intercepts with the real axis at the high–frequency region represent the R_s (equivalent series resistance) values, corresponding to the contact resistance between the α-Fe_2O_3 electrode material and the current collector substrate. The lower R_s value of α-Fe_2O_3/p-FTO (21.9 Ω) than that of α-Fe_2O_3/FTO (33.7 Ω) implies facile transport of electrons achieved by short migration paths through the α-Fe_2O_3 active material directly contacting the 3D p-FTO current collector. The diameter of the semicircle at the middle frequency region is related with R_{ct}, which corresponds to the interfacial charge transfer resistance between the α-Fe_2O_3 layer and the electrolyte. α-Fe_2O_3/p-FTO had a lower R_{ct} value, indicating improved transport behavior of holes due to a decrease of bulk recombination achieved by the rapid transfer of electrons to the 3D-current collector.

The current density-time curves of α-Fe_2O_3 on bare FTO and p-FTO were obtained by a chopped illumination of AM 1.5 G at an interval of 10 s on/off for UV-visible light at 1.5 V vs. RHE (**Figure 2.3.4c**). The abrupt occurrence and decay of the photocurrent density with sharp rectangular shapes during the on/off illumination sequence implies fast conduction of photo-generated electrons from α-Fe_2O_3 to p-FTO. Photocurrent in the J-t curves remained constant and closely matched that of the J-V curves in **Figure 2.3.4a**, indicating that the α-Fe_2O_3 materials are very stable over many cycles.

The incident photon-to-electron conversion efficiency (IPCE), with a rapid increase at about 580 nm corresponding to roughly 2.14 and 2.17 eV band gap energy of α-Fe_2O_3/FTO and α-Fe_2O_3/p-FTO, is shown in **Figure 2.3.4d**. The IPCE curve of α-Fe_2O_3/p-FTO slightly increased at about 675 nm wavelength. The IPCE value of 65 % at 300 nm α-Fe_2O_3/p-FTO showed overall improved performance compared with α-Fe_2O_3/bare FTO. This is consistent with the result of Tauc plots in **Figure 2.3.5**.

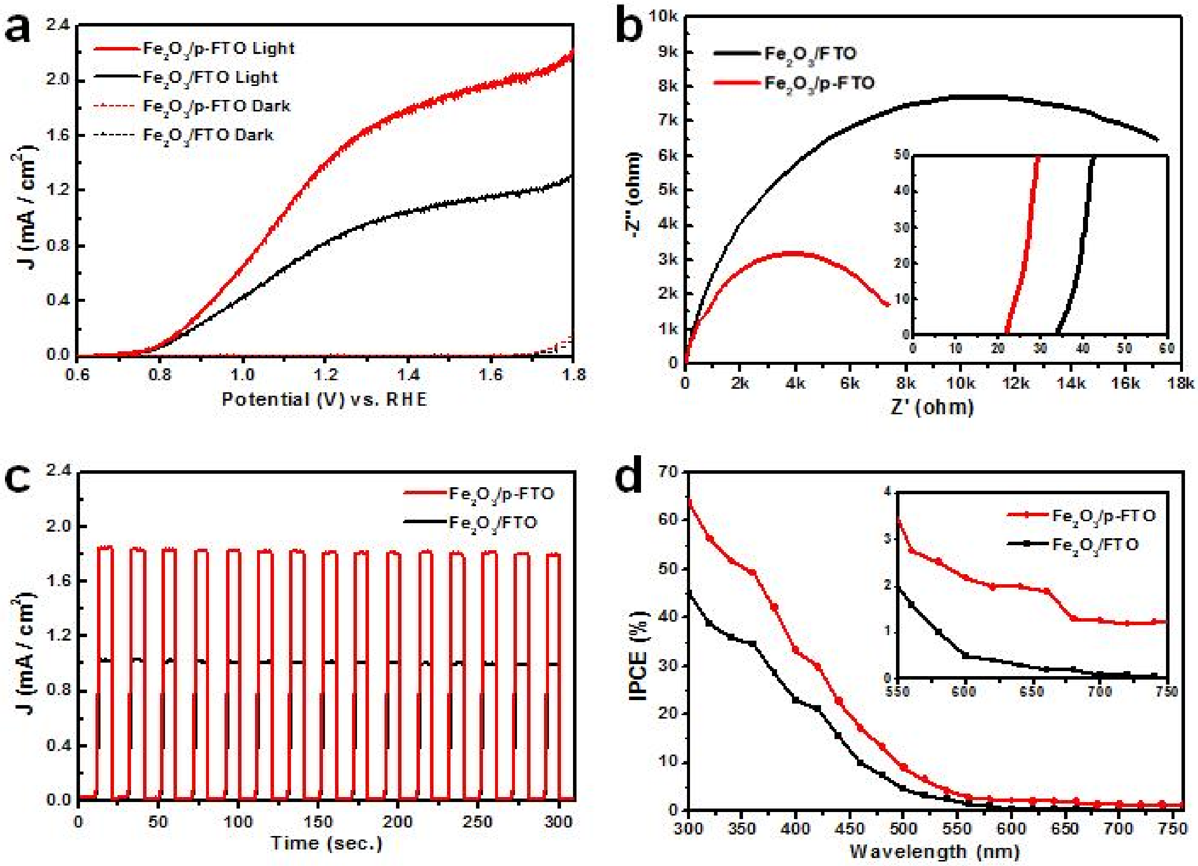

Figure 2.3.4 The photoelectrochemical properties of α-Fe_2O_3 on bare FTO and p-FTO (a) Linear sweep voltammetry curves (LSV, photocurrent - potential curves) of α-Fe_2O_3/FTO and p-FTO under UV-visible light and dark conditions. (b) Nyquist plots of α-Fe_2O_3/FTO and α-Fe_2O_3/p-FTO to investigate the electrochemical impedance spectroscopy (EIS) responses. (c) Photocurrent–time (J-t) curves of α-Fe_2O_3/FTO and α-Fe_2O_3/p-FTO at a bias of 1.5 V vs. RHE under UV-visible light illumination. (d) Measurement of the incident photon-to-electron conversion efficiency.

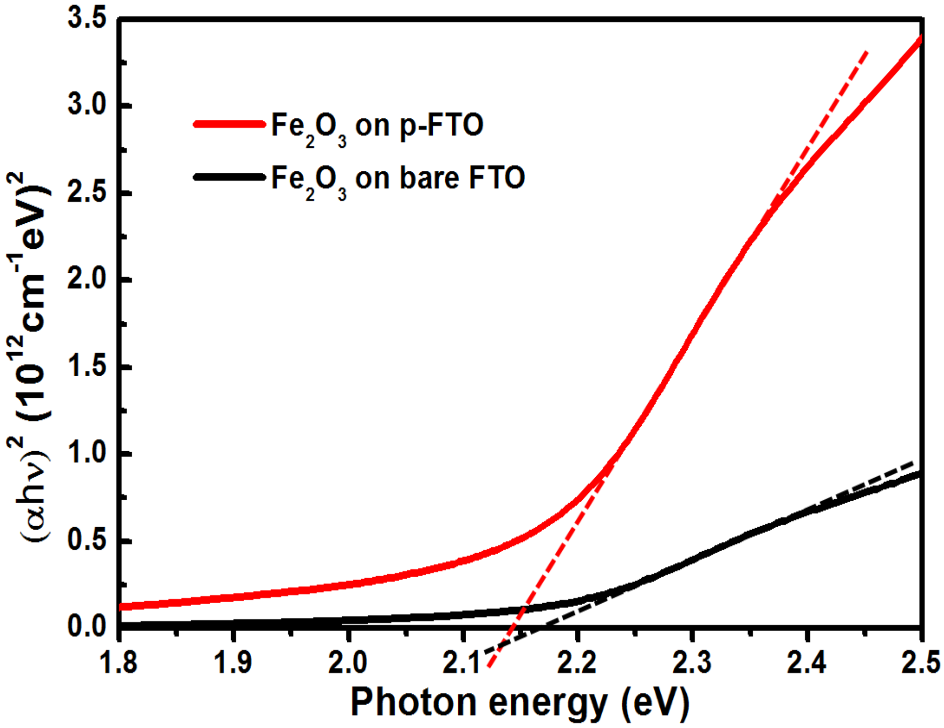

Figure 2.3.5 Tauc plots calculated using absorbance data of UV-visible spectroscopy.

2.3.4 Conclusion

Despite the very attractive properties of hematite as a photoanode in water splitting systems, many limitations remain. We overcome these issues by simply coupling a three-dimensionally and periodically patterned current collector, p-FTO, with worm-like α-Fe_2O_3. p-FTO was fabricated by a facile RIE method of SU-8 square patterns generated via interference lithography on a commercial FTO substrate. p-FTO provides enhanced light scattering effects and rapid and direct transfer pathways to the current collectors, leading to enhancement of the photocurrent density achieved by reducing recombination of photogenerated electrons and holes. Hematite on p-FTO showed 1.7 times improved photocurrent density relative to the corresponding structure on bare FTO. This is meaningful since key problems of hematite photoanodes for photoelectrochemical water splitting were overcome efficiently by simple patterning of the current collectors.

2.3.5 References

1. R. Raja, P. Sudhagar, A. Devadoss, C. Terashima, L. K. Shrestha, K. Nakata, R. Jayavel, K. Ariga and A. Fujishima, *Chemical Communications*, 2015, **51**, 522-525.
2. K. Kim, P. Thiyagarajan, H.-J. Ahn, S.-I. Kim and J.-H. Jang, *Nanoscale*, 2013, **5**, 6254-6260.
3. K. Kim, M.-J. Kim, S.-I. Kim and J.-H. Jang, *Sci. Rep.*, 2013, **3**.
4. T. Wang, R. Lv, P. Zhang, C. Li and J. Gong, *Nanoscale*, 2015, **7**, 77-81.
5. A. Kargar, Y. Jing, S. J. Kim, C. T. Riley, X. Pan and D. Wang, *ACS Nano*, 2013, **7**, 11112-11120.
6. H. Zheng, J. Z. Ou, M. S. Strano, R. B. Kaner, A. Mitchell and K. Kalantar-zadeh, *Advanced Functional Materials*, 2011, **21**, 2175-2196.
7. D.-D. Qin, C.-L. Tao, S. A. Friesen, T.-H. Wang, O. K. Varghese, N.-Z. Bao, Z.-Y. Yang, T. E. Mallouk and C. A. Grimes, *Chemical Communications*, 2012, **48**, 729-731.
8. J. Y. Kim, G. Magesh, D. H. Youn, J.-W. Jang, J. Kubota, K. Domen and J. S. Lee, *Sci. Rep.*, 2013, **3**.
9. M. Marelli, A. Naldoni, A. Minguzzi, M. Allieta, T. Virgili, G. Scavia, S. Recchia, R. Psaro and V. Dal Santo, *ACS Applied Materials & Interfaces*, 2014, **6**, 11997-12004.
10. A. G. Joly, J. R. Williams, S. A. Chambers, G. Xiong, W. P. Hess and D. M. Laman, *Journal of Applied Physics*, 2006, **99**, -.
11. K. Sivula, R. Zboril, F. Le Formal, R. Robert, A. Weidenkaff, J. Tucek, J. Frydrych and M. Grätzel, *Journal of the American Chemical Society*, 2010, **132**, 7436-7444.
12. H.-J. Ahn, M.-J. Kwak, J.-S. Lee, K.-Y. Yoon and J.-H. Jang, *Journal of Materials Chemistry A*, 2014, **2**, 19999-20003.
13. M. Barroso, S. R. Pendlebury, A. J. Cowan and J. R. Durrant, *Chemical Science*, 2013, **4**, 2724-2734.
14. H. Jun, B. Im, J. Y. Kim, Y.-O. Im, J.-W. Jang, E. S. Kim, J. Y. Kim, H. J. Kang, S. J. Hong and J. S. Lee, *Energy & Environmental Science*, 2012, **5**, 6375-6382.
15. D. A. Wheeler, G. Wang, Y. Ling, Y. Li and J. Z. Zhang, *Energy & Environmental Science*, 2012, **5**, 6682-6702.
16. Y. Ling, G. Wang, D. A. Wheeler, J. Z. Zhang and Y. Li, *Nano Letters*, 2011, **11**, 2119-2125.
17. X. Shi, K. Zhang, K. Shin, J. H. Moon, T.-W. Lee and J. H. Park, *Physical Chemistry Chemical Physics*, 2013, **15**, 11717-11722.
18. Y. Qiu, S.-F. Leung, Q. Zhang, B. Hua, Q. Lin, Z. Wei, K.-H. Tsui, Y. Zhang, S. Yang and Z. Fan, *Nano Letters*, 2014, **14**, 2123-2129.
19. R. H. Goncalves and E. R. Leite, *Energy & Environmental Science*, 2014, **7**, 2250-2254.
20. Y. Hou, F. Zuo, A. Dagg and P. Feng, *Angewandte Chemie International Edition*, 2013, **52**, 1248-1252.

21. J. Baltrusaitis, Y.-S. Hu, E. W. McFarland and A. Hellman, *ChemSusChem*, 2014, **7**, 162-171.
22. O. Zandi, J. A. Beardslee and T. Hamann, *The Journal of Physical Chemistry C*, 2014, **118**, 16494-16503.
23. F. Wang, N. K. Subbaiyan, Q. Wang, C. Rochford, G. Xu, R. Lu, A. Elliot, F. D'Souza, R. Hui and J. Wu, *ACS Applied Materials & Interfaces*, 2012, **4**, 1565-1572.
24. M. T. Mayer, Y. Lin, G. Yuan and D. Wang, *Accounts of Chemical Research*, 2013, **46**, 1558-1566.
25. K.-Y. Yoon, J.-S. Lee, K. Kim, C. H. Bak, S.-I. Kim, J.-B. Kim and J.-H. Jang, *ACS Applied Materials & Interfaces*, 2014.
26. J. Young Kim, J.-W. Jang, D. Hyun Youn, J. Yul Kim, E. Sun Kim and J. Sung Lee, *RSC Advances*, 2012, **2**, 9415-9422.
27. Y. Sun, W. D. Chemelewski, S. P. Berglund, C. Li, H. He, G. Shi and C. B. Mullins, *ACS Applied Materials & Interfaces*, 2014, **6**, 5494-5499.
28. C. H. Bak, K. Kim, K. Jung, J.-B. Kim and J.-H. Jang, *Journal of Materials Chemistry A*, 2014, 2, 17249-17252.
29. K. Kim, I.-H. Kim, K.-Y. Yoon, J.-Y. Lee and J.-H. Jang, *Journal of Materials Chemistry A*, 2015, 3, 7706-7709.

Chapter 3

Solar Steam Generation

3.1 Mesoporous Three-Dimensional Graphene Networks for Highly Efficient Solar Desalination under 1 sun Illumination

Adapted with permission from ref. 39. Copyright 2018 American Chemical Society

3.1.1 Introduction

The earth is facing serious environmental problems such as a lack of clean fuel and fresh water supplies, which will be indispensable in the future with a rapid growth of modern industry, population expansion, and accompanying serious environmental pollution problems.[1] Solar energy is a critical energy source, with pure, free, inexhaustible, and fairly accessible properties at any location, including developing countries and remote areas without basic infrastructures. Although water is one of the most abundant resources on earth, covering three-quarters of the earth's surface, 97% is seawater. An efficient desalination technique of this abundant seawater using solar energy without extra energy input could thus be a promising solution to supply fresh water to human beings in the future.[2−5] Solar desalination occurs in nature by bulk heating of seawater to produce rain with unlimited energy supply and minimum environmental impact. However, as an alternative technique for obtaining fresh water, it is highly limited by poor light-to-heat conversion efficiency because of the failure of heat localization by heat loss to bulk water, as well as inappropriate structures for generated vapor molecules to escape.[6−8] Therefore, recent studies have focused on generating a localized high temperature only at the surface of seawater, which facilitates efficient steam generation under 1 sun solar irradiation without any artificial concentration of light or electric power.[7,9−12] These results were achieved by ensuring maximum absorption of active materials in the full solar spectrum range (from 300 to 2500 nm), hydrophilic surface property, effective thermal insulation from bulk water, and an efficient escape process for generated vapor bubbles with minimal heat loss.[13−19] Recently, a wood piece has been suggested as a good thermal insulator with earth-abundance, hydrophilic surface, low distortion, and efficient water transportation properties in the field of solar steam generation.[20−23] Wu *et al.* developed a low cost and scalable photothermal system by coating nature produced wood with polydopamine.[24] Despite effective heat loss interception, the device reported relatively low evaporation rate and solar steam generation efficiency under 1 sun illumination because of insufficient solar absorption.[25] As efficient photoabsorbers, highly absorptive 3D graphene based materials have recently attracted great attention. Zhang *et al.* reported a vertically aligned graphene sheet membrane with an appropriate structure to release vapor, a hydrophilic surface, and high absorption for excellent photothermal transduction.[26] However, the macroporous structure with over 10 μm pores decreases the surface area for vapor generation, and mass production would be difficult because of the very complex fabrication procedure.[27] Mass-productive, 3D porous graphene based materials with a large surface area, outstanding light absorption, and an excellent photothermal transduction property is meanwhile one of the most attractive active materials for scalable and efficient solar desalination.[28–33] Here, we report a simple design of a gram-scale, hydrophilic, and mesoporous three-dimensional graphene network (3DGN)-based solar desalination device for efficient solar steam generation. About 92% solar-to-vapor conversion efficiency with a 1.64 kg/m^2h of evaporation rate is achieved under 1 sun illumination condition because of the synergistic effect of the enormously large surface area of the mesoporous 3D graphene structure, a hydrophilic surface with various functional groups, and high absorbance over the broadband sunlight wavelength.

3.1.2 Experimental procedures

3.1.2.1 Materials

PVA (M_w = 31,000−50,000), $NiCl_2 \cdot 6H_2O$, and 7 nm fumed silica were obtained from Sigma-Aldrich Chemical Company. Graphite powder and sodium chloride were purchased from Bay Carbon Inc. and Samchun Chemical, respectively. All chemicals were used without any further purification.

3.1.2.2 Preparation of GO Sheets.

GO was prepared from graphite powder by the Hummer's method. For purification, GO was washed by rinsing with 1 wt % HCl and filtrated with enough deionized (DI) water. GO was then centrifuged with DI water several times until the pH of the solution became neutral. Finally, the GO sheets were stacked by precipitation of a dispersed aqueous solution onto the wood piece via a drop casting method.

3.1.2.3 Preparation of 3DGN (3DGN-Ni).

PVA (10 wt %) was dissolved in DI water at 90 °C and then mixed with a $NiCl_2$ aqueous solution. Thin PVA/$NiCl_2$ films were prepared by self-assembly of colloidal silica NPs. The prepared composite was dried in a vacuum oven for one day. The prepared composite was annealed at 1000 °C for 30 min. in 100 sccm of H_2 in an Ar atmosphere at 4 Torr with a 20 °C/min. heating rate. After annealing, the samples were cooled to room temperature rapidly followed by immersion into an etching solution consisting of HF and HCl for 48 h. to remove the colloidal silica template and nickel simultaneously. For the 3DGN-Ni sample, a NaOH aqueous solution was used as the etching solution to remove the colloidal silica only.

3.1.2.4 Preparation of the Photoabsorbers on the Wood Piece.

A wood piece was prepared by a radial cut of a round wood stick with 1.5 cm thickness. The wood piece's cylindrical-shaped vessel structures with a high aspect ratio enable it to float when partially dipped into a 3.5% NaCl aqueous solution (simulated seawater) during measurement of the solar desalination efficiency. Various quantities of completely dried

3DGN (3DGN-Ni) were dispersed in 1 mL of DI water. Using the well-dispersed aqueous solution, 3DGN (3DGN-Ni) was uniformly deposited on the wood piece via a facile drop casting method.

3.1.2.5 Characterization.

The characterization was investigated by scanning electron microscopy (Hitach High-Technologies S-4800), transmission electron microscopy (TEM) (JEOL JEM-2100), Raman spectroscopy (WITec alpha300R), XPS (Thermo Fisher K-alpha), UV-Vis-NIR spectroscopy (Agilent Cary 5000), and ion chromatography (Thermo Fisher Scientific ICP 1600 for cation and ICP 2100 for anion). Thermal conductivity of powder samples was measured by the thermal constant analyzer (Hot Disk TPS 2500S). Steam Generation Measurements. The temperature and mass change by the evaporation of water for GO, 3DGN-Ni, and 3DGN on the bare wood and water only (none) were measured under the irradiation of simulated solar illumination (Sol2A class ABA 94062A, 1000 W Xenon lamp, Newport) at a power density of 1 kW/m^2. The temperature was measured using a thermographic camera, and the mass change from evaporation was investigated with an outer thermal insulation layer (about 1 cm thick styrofoam) using an electronic microbalance with an accuracy of 0.1 mg every 1 min. A cylindrical shape wood piece with 1.5 cm thickness was floated on the surface of water in a 10 mL glass beaker with 2.2 cm diameter and 4.5 cm height.

3.1.3 Results and discussion

Mesoporous 3DGNs designed to have ultrahigh absorption of sunlight and to release generated vapors efficiently in the air-pockets were mass-produced as a photoabsorber material by the procedure depicted in **Scheme 3.1.1a**. Briefly, annealing poly vinyl alcohol (PVA)/nickel precursors wrapped onto silica nanospheres in a hydrogen environment reduced nickel ions and generated few-layer graphene sheets by precipitation of carbon on the surface of aggregated nickel particles. Silica nanospheres and aggregated nickel compounds served as the template and catalyst, respectively, for the growth of mesoporous graphene. Etching a silica-only compound or both a nickel and silica compound creates mesoporous 3DGN-Ni or 3DGN with a few nanometer-sized pores, respectively. **Scheme 3.1.1b** shows the design of a highly efficient, inexpensive, and environment friendly solar desalination device constructed with the photoabsorber material (3DGN) at the top surface and a water transporting water transporting layer (wood piece) on the body. The mesopores in the 3DGN enhance the light absorption via multiple scattering of absorbed light and help the generated vapors escape into the air, as shown in the zoomed in the circle of **Scheme 3.1.1b**. The wettable wood piece provides very efficient water paths by capillary force because of the presence of dense, vertically aligned tube structures with a few tens of micrometer vessels, as shown in **Figure 3.1.1**. The wood piece also served as a thermal insulator at the interface between the bulk seawater and the photoabsorber material because of its very low thermal conductivity (～0.45 W/mK for wet-state wood), as reported.[22] The heat loss of the generated steam to the bulk water intrinsically reduces the solar-to-vapor conversion efficiency because the heating of bulk water is not necessary and generated steam may condense back to bulk water. Floating the insulating wood piece, which places photoabsorber materials at the water－air interface, localizes the intense heat on the evaporative surface, resulting in the efficient generation of water bubbles without heat loss to the bulk seawater.

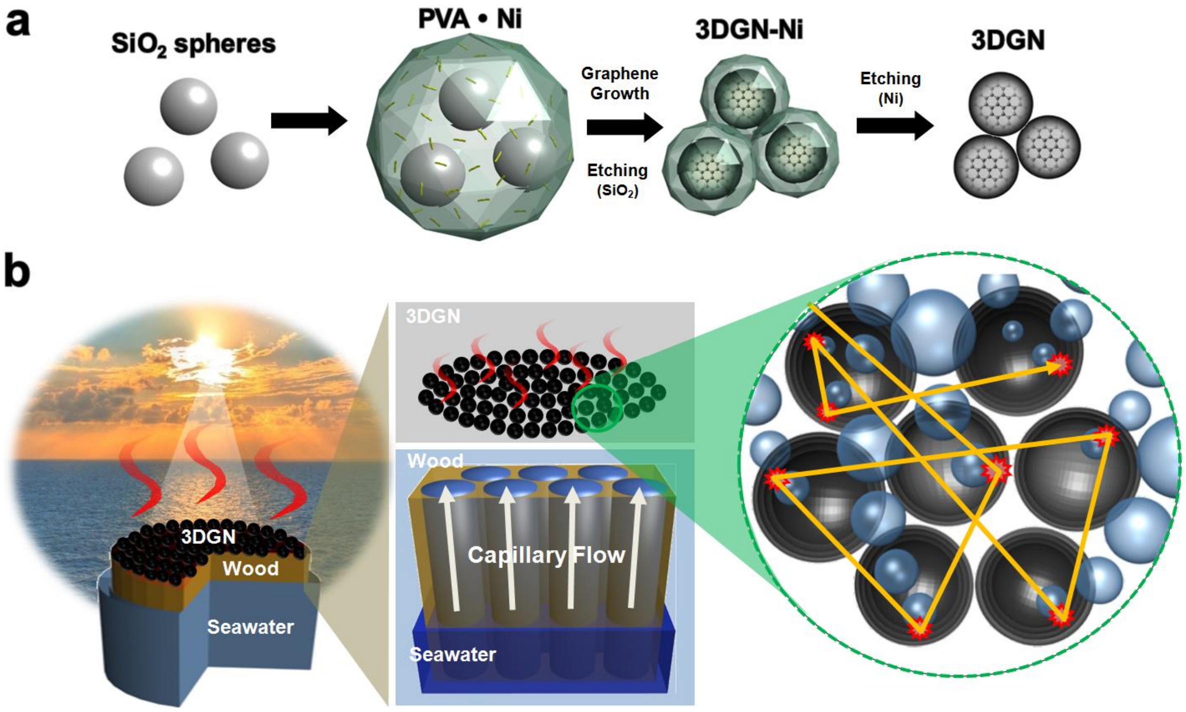

Scheme 3.1.1 Schematic of the (a) 3DGN fabrication procedure and (b) the working process of the 3DGN-based solar desalination device. The right inset shows multiple scattering of light and the formation of water bubbles in the mesoporous structure of 3DGN.

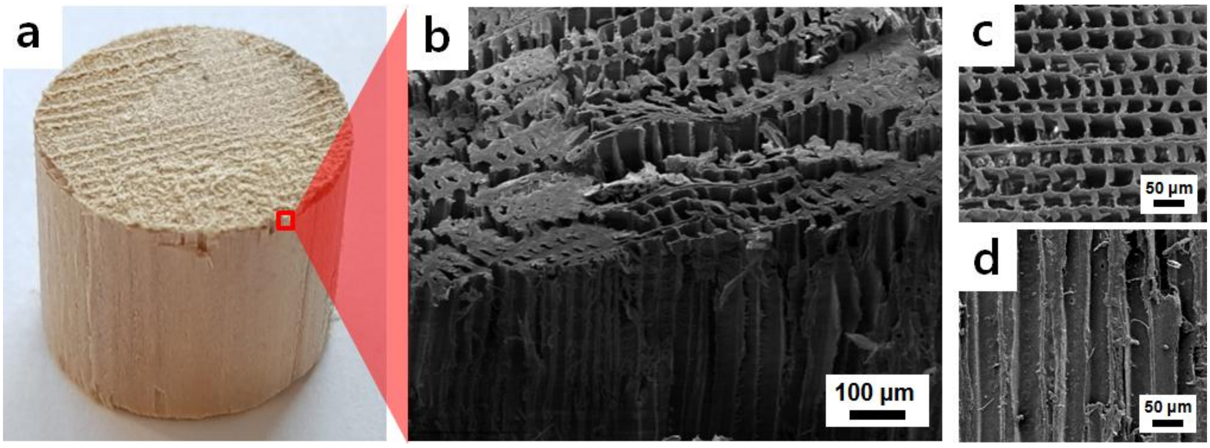

Figure 3.1.1 Digital camera image (a) and scanning electron microscopy (SEM) images (b-d) of the wood piece water transport medium.

In this study, we compared the photo-thermal energy conversion performance of 3DGN with graphene oxide (GO) and 3DGN-Ni as a representative photoabsorber of broadly studied carbon materials[18, 28, 29] and the photoabsorber with enhanced thermal conductivity incorporating nickel compounds[30] (0.1855 W/mK (3DGN-Ni) vs. 0.073 W/mK (3DGN) measured by the thermal constant analyzer), respectively. **Figure 3.1.2** shows the morphologies of GO, 3DGN-Ni, and 3DGN, which have large differences in the porosity of their structures. The GO sample was prepared by precipitation of GO sheets exfoliated by Hummer's method. An abundant portion of pores in 3DGN-Ni and 3DGN are observed after etching templates, whereas GO forms a sheet-like structure without many pores, which implies that the generated vapors in GO cannot readily escape into the air (**Figure 3.1.2a**). Compared to 3DGN (**Figure 3.1.2c**), 3DGN-Ni is a less porous structure with agglomerated nickel particles on the surface formed during the high temperature annealing process (**Figure 3.1.2b**). **Figure 3.1.2d** confirms the presence of many pores enveloped by 3-7 layers of graphene (See the inset). Releasing the generated vapor molecules is very important for continuous and efficient generation of vapor molecules since the high heat capacity of water vapor molecules trapped in the structure of the photoabsorber material inhibits the temperature increase of the photoabsorber material. If the water layer is not sufficiently shallow in the large inner pore, the vapors are liquefied back before escaping while the vapor bubbles travel through the water region.[31] Therefore, the presence of micro/mesopores in the photoabsorber material is essential for vaporized water bubbles to escape into the air and thus for efficient solar vapor generation. The mesoporous cavities partitioned by a few layers of graphene not only facilitate the evaporation of smaller water droplet by providing appropriate cavities for the generation of the vapor but also enhance the absorption property due to multiple scattering of light,[32] and thus lead to high photo-thermal energy conversion efficiency (**Scheme 3.1.1b**). The surface areas and pore size distributions of GO, 3DGN-Ni, and 3DGN were examined by Brunauer−Emmett−Teller (BET) and Barrett–Joyner–Hallender (BJH) methods, respectively. **Figure 3.1.3** shows that the surface areas of GO, 3DGN-Ni, and 3DGN were about 5 cm^2/g, 306 cm^2/g, and 1203 cm^2/g, respectively, with a rapidly increased portion of micro/mesopores with an increase of the surface area.

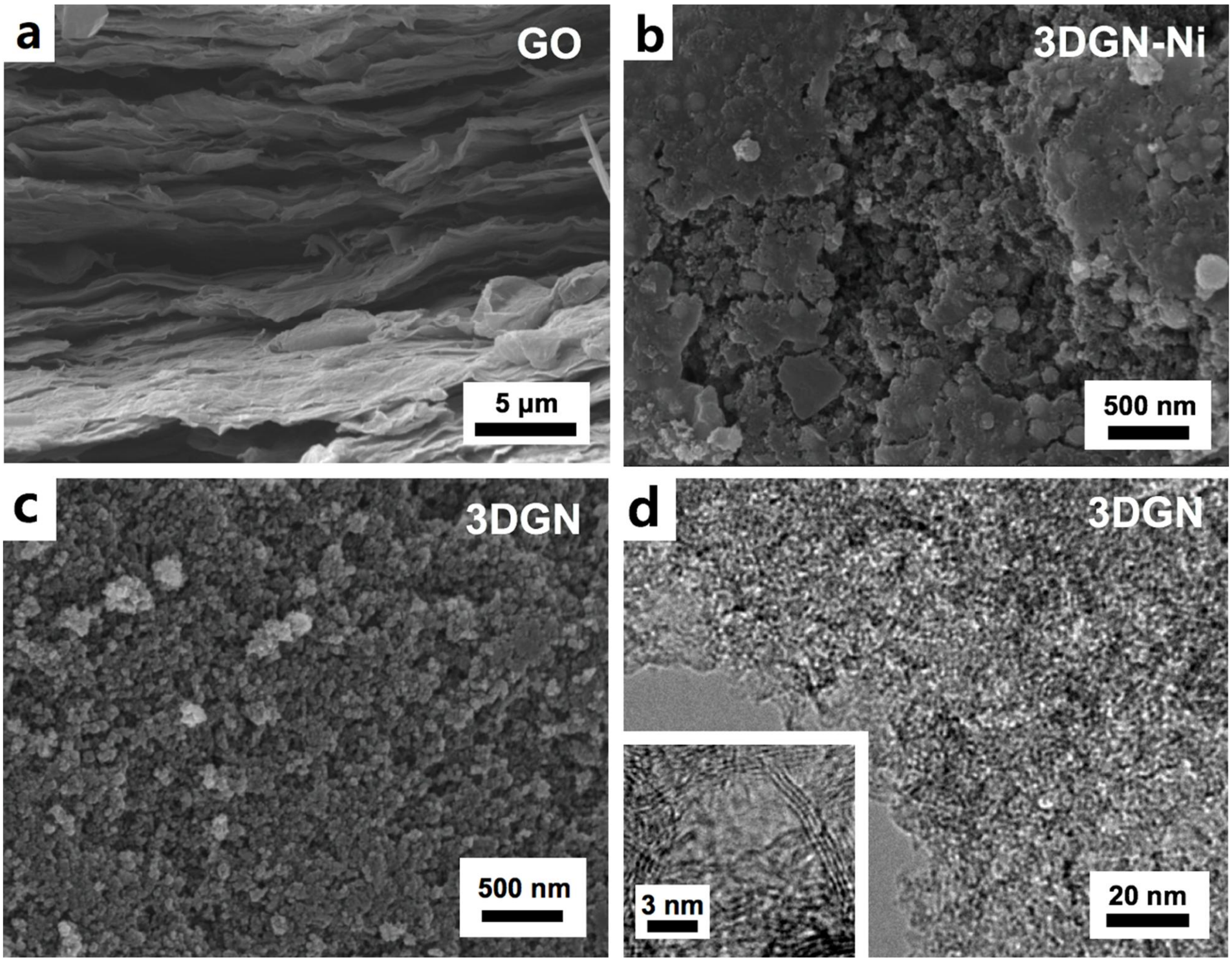

Figure 3.1.2 Morphologies of (a) GO, (b) 3DGN-Ni, and (c, d) 3DGN confirmed via electron microscopy. The inset is a magnified TEM image of few-layered graphene sheets.

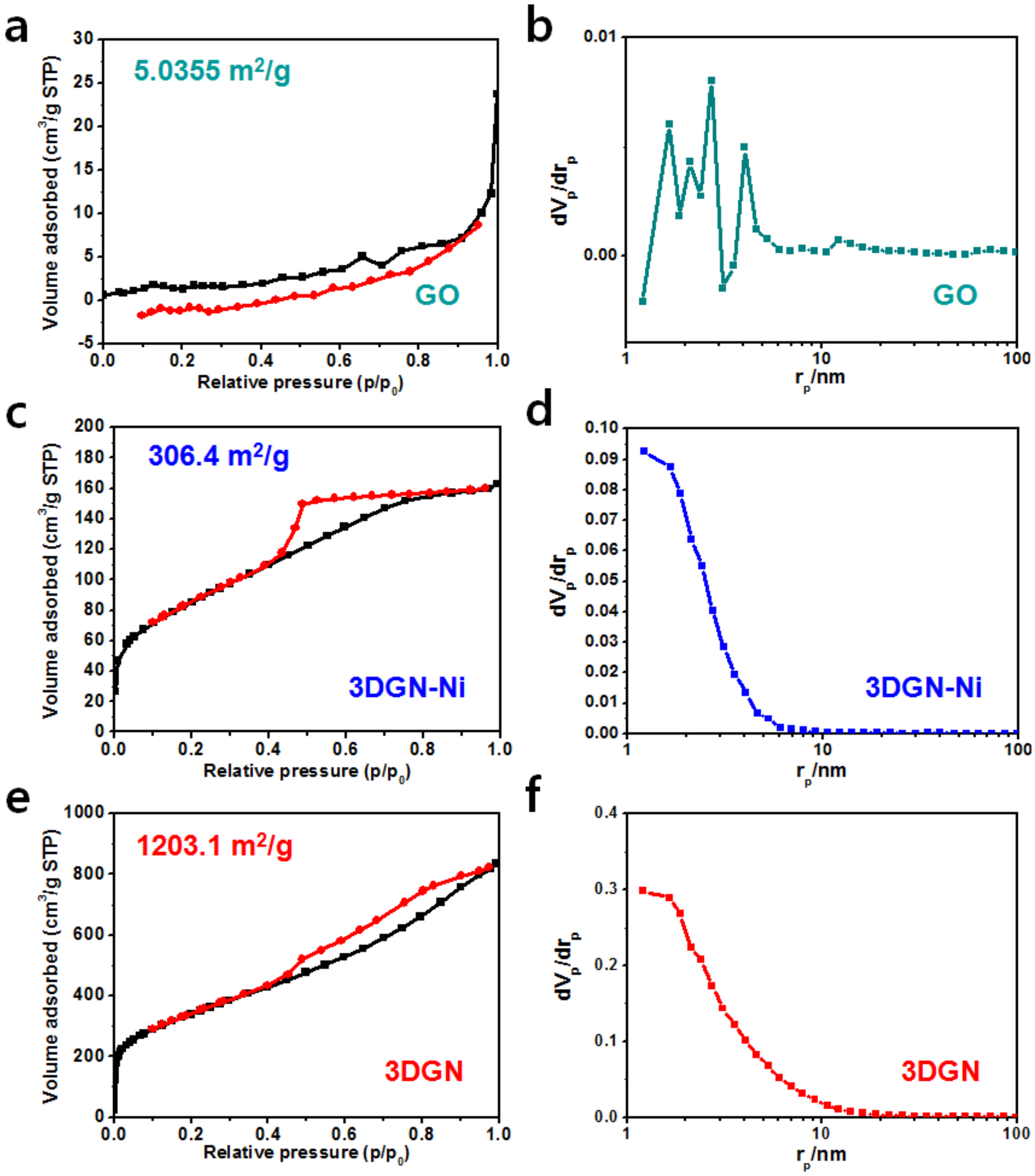

Figure 3.1.3 BET investigation of the surface area and the pore size distribution of GO, 3DGN-Ni, and 3DGN.

Figure 3.1.4 shows digital camera images of the photoabsorber materials on the wood post and various characterization results of the photoabsorber materials including the bare wood transport medium. 3DGN-Ni and 3DGN look dark black whereas GO is dark grey, when the same amount of photoabsorber materials are loaded, indicating higher absorption of 3DGN based materials than GO (**Figure 3.1.4a**). As can be seen in the Raman spectra (**Figure 3.1.4b**), the characteristic D-band (~1350 $\mathrm{cm^{-1}}$) and G-band (~1600 $\mathrm{cm^{-1}}$) were observed for all photoabsorber materials, whereas the 2D-band (~2700 $\mathrm{cm^{-1}}$) only appeared in 3DGN-Ni and 3DGN, implying the presence of a greater portion of graphitic regions than in GO. To generate the steam effectively via the thermal evaporation of transferred seawater, solar desalination device should have the photoabsorber material containing a high light absorption and efficient energy conversion from sunlight to heat. For a quantitative characterization of the photoabsorber materials, the absorption spectra were measured in the broadband solar spectrum ranging from 300 to 2500 nm wavelength via UV-Vis-NIR spectrometry (**Figure 3.1.4c**). While the GO sheets exhibited an absorbance value of around 90%, both 3DGN-Ni and 3DGN exhibit higher absorption exceeding 97% in the full range of the spectrum. 3DGN has slightly higher absorption than 3DGN-Ni, due to the greater content of mesoporous structure, which causes the light scattering in 3DGN. This is confirmed by the reflectance spectra of 3DGN and 3DGN-Ni in **Figure 3.1.5**. The average absorbance of the bare wood was found to be only ~50% in the ultraviolet and visible regions and ~40% in the near-infrared region. **Figure 3.1.4d** shows the C1s X-ray photoelectron spectroscopy (XPS) peak of 3DGN (The whole range of the spectrum with both C and O contents is given in **Figure 3.1.6**). The C1s peak is deconvoluted into four types of carbon peaks, C-C (aromatic) at ～284.2 eV, C-O (hydroxyl and epoxy) at ~285.7 eV, C=O (carbonyl) at ~287.2 eV, and O-C=O (carboxyl) at ~288.5 eV, indicating the abundant presence of hydrophilic functional groups in the structures. A water droplet dropped on the surface of 3DGN leaked into 3DGN in a few seconds, confirming the hydrophilic surface property of the mesoporous structure. The XPS analyses of GO and 3DGN-Ni in **Figure 3.1.6** indicate a similar surface property to that of 3DGN.

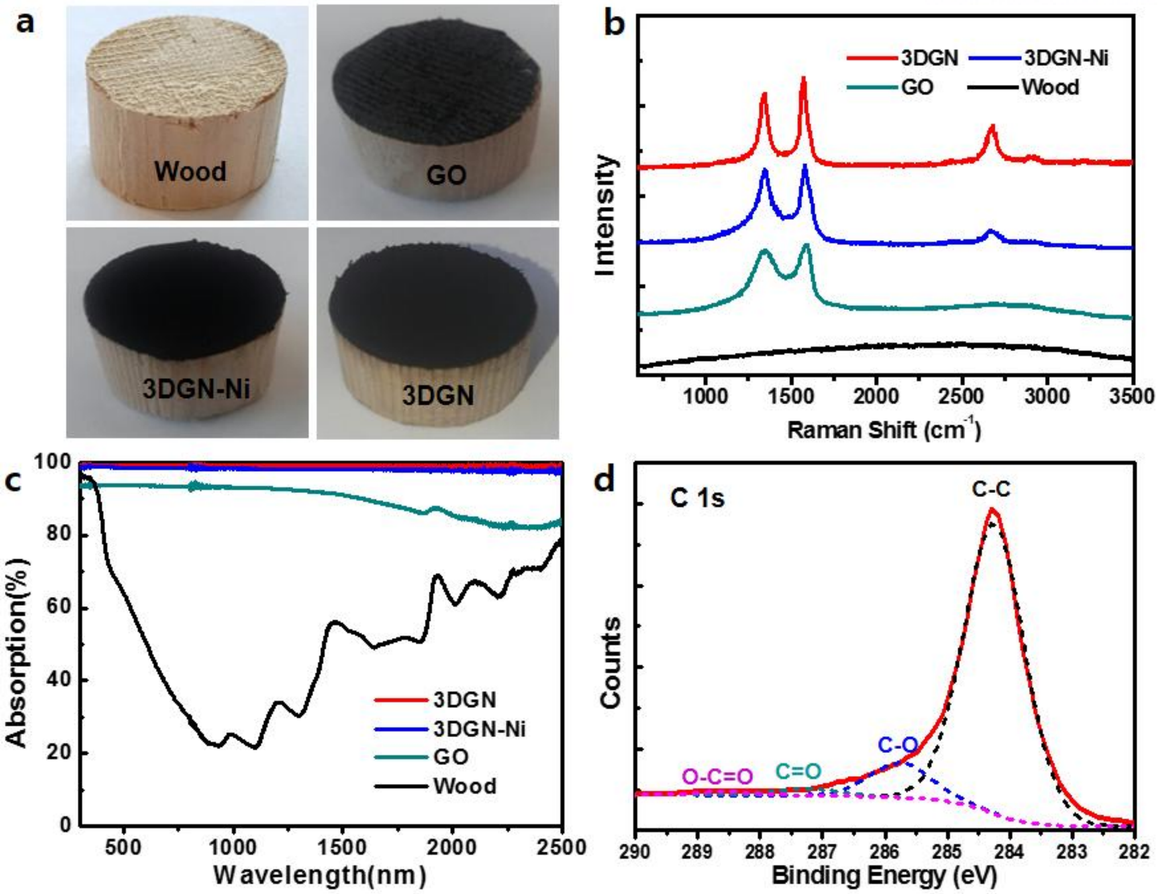

Figure 3.1.4 Characterization of materials used to solar desalination device. (a) DC image of the bare wood and GO, 3DGN-Ni, 3DGN on the wood. (b) Raman spectra and (c) UV-Visible spectroscopy of wood, GO, 3DGN-Ni and 3DGN. (d) C1s XPS spectrum of 3DGN.

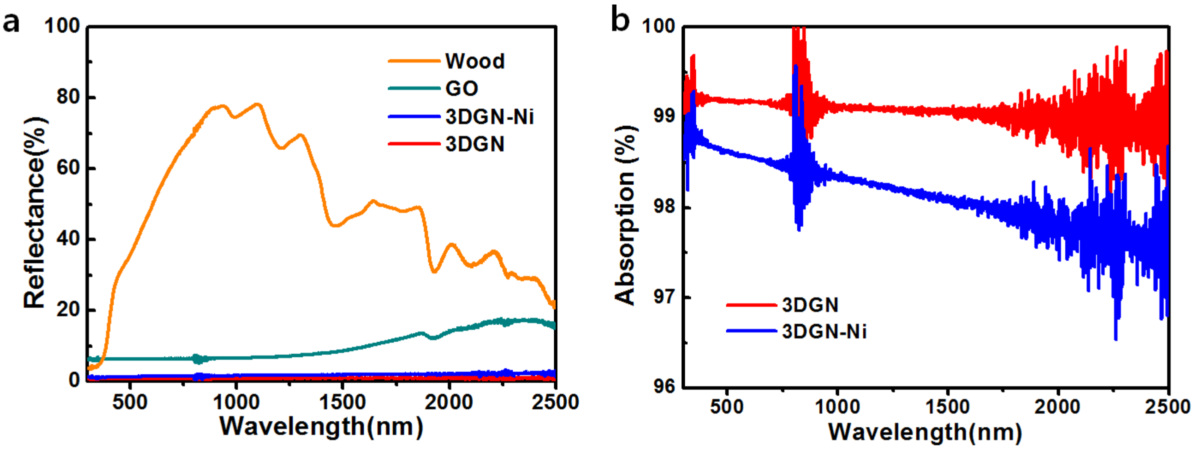

Figure 3.1.5 (a) Reflectance of the wood piece, GO, 3DGN-Ni and 3DGN, and (b) magnified absorption graph for 3DGN-Ni and 3DGN from 300nm to 2500nm wavelength.

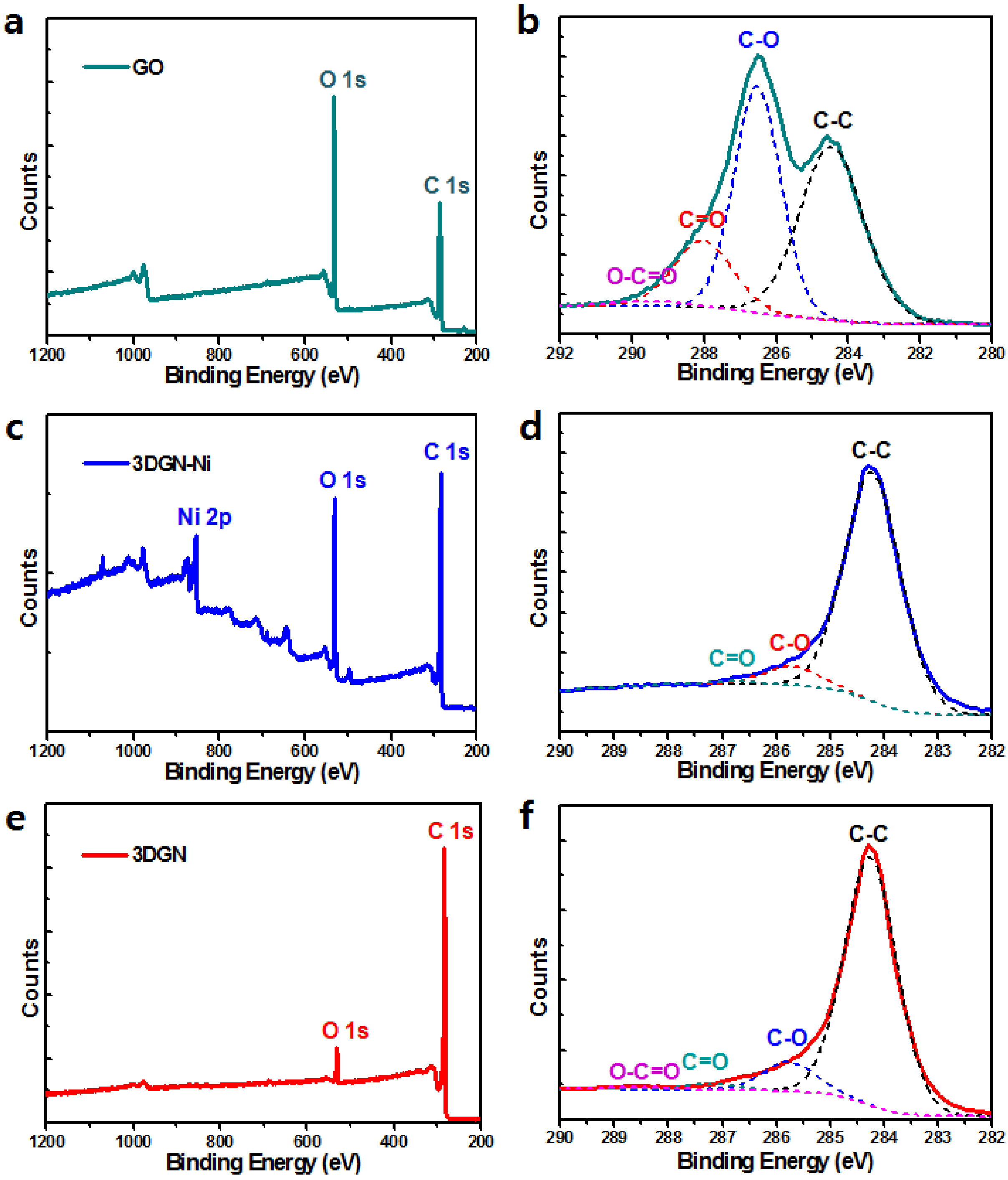

Figure 3.1.6 XPS general spectra and curve fitting of C1s spectra of (a, b) GO, (c, d) 3DGN-Ni and (e, f) 3DGN.

With desirable features such as ultrahigh sunlight absorption and hydrophilicity of mesoporous 3DGN, and the low thermal conductivity of the wood piece with minimum heat loss, the 3DGN deposited wood piece can be used directly as an efficient solar steam generation device. The prepared solar desalination devices were placed under a solar simulator (AM 1.5, 1000W Xenon lamp, Newport) while the top surface of the photoabsorbers was fully wet in about 20 seconds by water transferred via the vertical path of the wood piece from bulk seawater at ~24 °C and ~20% humidity. After 1 sun solar illumination for one hour, the temperature on the top surface of the photo-absorbers (GO, 3DGN-Ni, and 3DGN) rapidly increased from room temperature to around 41.8 °C, 46.2 °C, and 61.0 °C, respectively, as shown in **Figure 3.1.7a**. The temperature at the surface of the bare wood and bulk water remained at 34.3 °C and 30.1 °C, respectively, since no photothermal conversion mechanism is operative. 3DGN showed the largest temperature increase among all samples, indicating that it provides the most effective photothermal conversion efficiency. This is ascribed to the synergistic effects of excellent solar absorption, a hydrophilic surface property, and a mesoporous structure of 3DGN. The lower temperature differences before/after illumination for GO than 3DGN and 3DGN-Ni are attributed to the lower light absorption properties and porosities. The much greater solar-to-thermal energy conversion of 3DGN than 3DGN-Ni with a similar absorption property and wettability but lower thermal conductivity is attributed to the larger amount of micro/mesopores that greatly facilitate the evaporation of water bubbles without heat loss into the air in 3DGN. By combining the highly absorptive and mesoporous materials onto the wood post, the large temperature increase on the surface of the 3DGN under the 1 sun illumination resulted in the appearance of vapor bubbles, which indicates active evaporation of water (**Figure 3.1.8**). The digital camera image of 3DGN and thermographic images of GO, 3DGN-Ni, and 3DGN deposited wood posts on saline water reveal the temperature variations between the top of the photoabsorber materials and the bulk saline water after the sunlight illumination. The large temperature difference between the top and bottom of the devices demonstrates that the insulating wood post not only acts as a water transport medium but also effectively localizes the heat at the surface of the photoabsorber material and thus minimizes the heat loss into bulk water. As a result, the temperature difference in 3DGN, the most effective photoabsorber, was about 36.5 °C while the values were 17.7 °C and 22.3 °C for GO and 3DGN-Ni, respectively, after 1 hour of solar illumination with 1 kW/m^2.

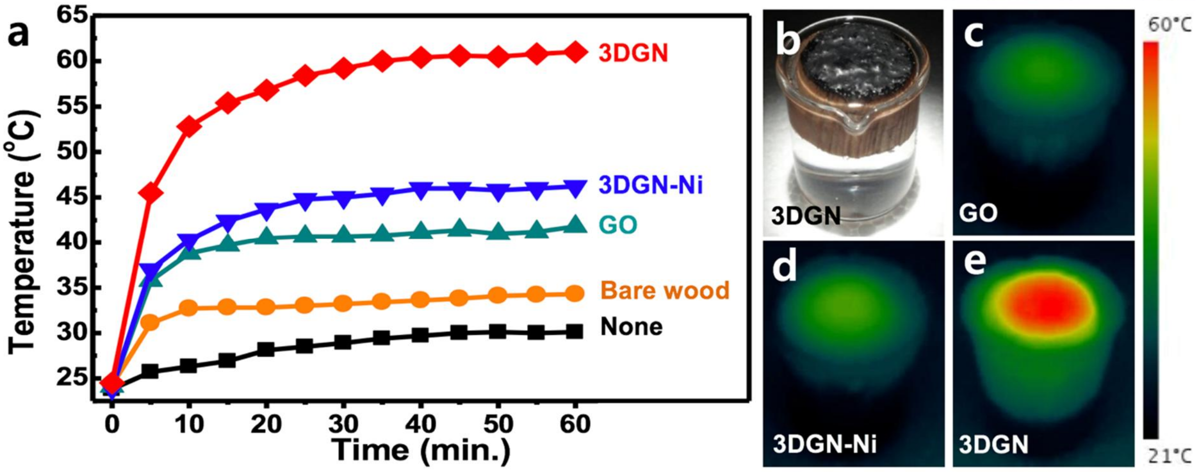

Figure 3.1.7 (a) Temperature changes at the top of bulk saline water, bare wood, and photoabsorber materials (GO, 3DGN-Ni, and 3DGN) on wood pieces. (b) DC image of 3DGN and thermographic images of (c) GO (d) 3DGN-Ni, and (e) 3DGN on the wood piece under 1 sun illumination for 1 hour. Amounts of photoabsorber materials are the same at 20 mg.

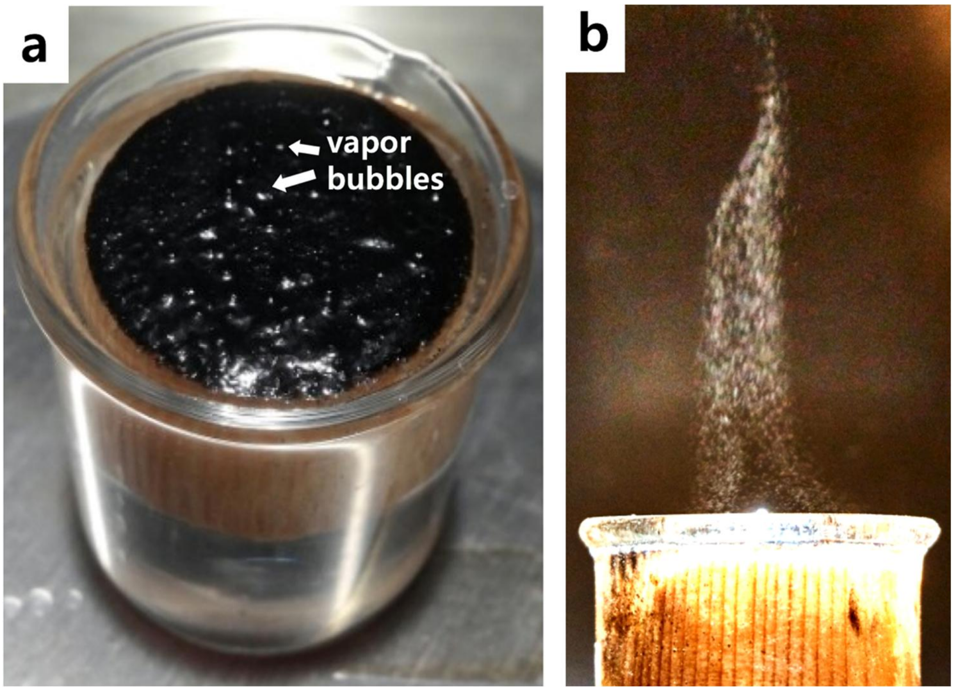

Figure 3.1.8 (a) Vapor bubbles (numerous white dots) on the surface of photoabsorber materials and (b) evaporated vapor flow to the air generated under 6 sun illumination condition.

To evaluate the solar-to-vapor conversion efficiency and the desalination ability of GO, 3DGN-Ni, and 3DGN deposited on the wood post under simulated solar illumination (1 kW/m^2), the mass change of 3.5% saline water was measured, as shown in **Figure 3.1.9**. All evaporation rates were measured at a steady state after illumination of simulated sunlight for 1 hour. Under a solar intensity of 1 kW/m^2, the mass change rate of the wood post with 20 mg of 3DGN was as high as about 1.64 kg/m^2·h, which is approximately 4.82 times higher than that of saline water only (about 0.34 kg/m^2·h). The steam generation rate of the bare wood remains at only 0.72 kg/m^2·h, which indicates the important role of the increased optical absorption with the efficient photoabsorber materials. GO and 3DGN-Ni samples on the wood posts present mass change rates of 1.42 and 1.49 kg/m^2·h, respectively, because lower light absorption (**Figure 3.1.4b** and **Figure 3.1.5**) and less pore content with lower surface area of the photoabsorber materials hinder fast steam generation. The solar-to-vapor conversion efficiency (η) was calculated by the followed **Equations (3.1.1)**.

$$\textbf{Equations (3.1.1):}\quad \eta = \frac{Q_e}{A\ C_{opt}\ Q_s} \qquad (Q_e = m\lambda + mC\Delta T)$$

where A is the cross-sectional area of light illumination, C_{opt} is the optical concentration, and Q_s is the intensity of the normal direct solar irradiation (1 kW/m^2). Q_e denotes the power consumed for steam generation, m is the mass flux by the energy converted from solar to heat only without natural evaporation in a dark condition (no illumination, **Figure 3.1.10**), λ is the latent heat of the phase change from water to vapor, C is the specific heat capacity of water (4.2 J/g·K), and ΔT denotes the temperature increase of the water. As shown in **Figure 3.1.9b**, pure water was found to have an efficiency of 14.7% under an illumination of 1 kW/m^2. For efficient solar-to-vapor conversion of the photoabsorber materials, which is directly related with the evaporation rate, a high temperature difference via efficient photothermal energy conversion, large surface area, and high micro/meso-porosity is very important to generate vapor molecules and to facilitate their escape into the air. The evaporation rates were consistent with the tendencies of these properties for the photoabsorber materials (GO, 3DGN-Ni, and 3DGN), as already confirmed. Although the three photoabsorbers have relatively small differences in the absorbance for the whole sunlight spectrum range, the greater portion of micro/mesopores and larger surface area of 3DGN facilitate a much higher evaporation rate and efficient solar-to-vapor conversion. The mass changes for various amounts of 3DGN deposited on wood posts were also investigated to optimize the solar-to-vapor conversion efficiency, as shown in **Figure 3.1.9c**. The values of mass change show saturation at 20 mg of 3DGN since the bottom thick 3DGN layer stacked with more than 20 mg of 3DGN could not absorb the sunlight to effectively increase the temperature and to generate vapor. As shown in **Figure 3.1.9b**, 3DGN (20 mg) on the wood sample has an efficiency of 91.8% with an evaporation rate of 1.64 $kg/m^2 \cdot h$, which is superior to the best values in the previously reported literature (**Table 3.1.1**). 91.4 % and 76.6 % of the original value were maintained after 20 cycles and 6 hours continuous irradiation, which prove relatively good durability of our device (**Figure 3.1.11**). To systematically evaluate the effect of desalination, the difference in salinity between simulated seawater and collected vapor was measured by inductively coupled plasma mass-spectroscopy (ICP-MS). The concentrations of sodium and chloride ions in the collected vapor were dramatically decreased compared with the concentrations of ions in simulated seawater before solar desalination of the porous 3DGN-based device. As shown in **Figure 3.1.9d**, the salinity of the vapor collected via the desalination process was far below the salinity levels of safe drinking-water defined by the World Health Organization (WHO) and the US Environmental Protection Agency (EPA) standards.[7]

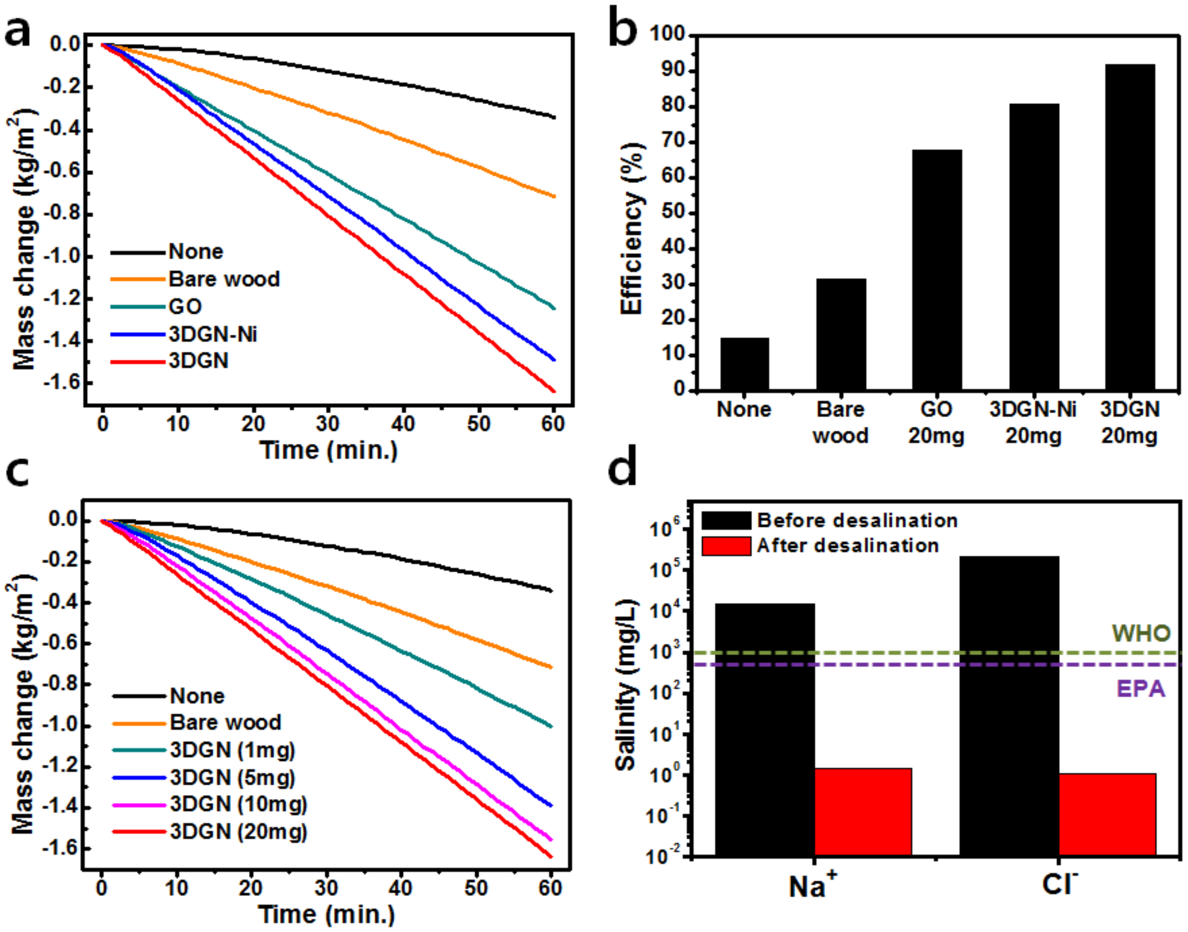

Figure 3.1.9 (a) Vapor-evaporation-induced mass changes of water with solar desalination devices constructed by 20 mg of GO, 3DGN-Ni, and 3DGN on the wood posts as a function of time under solar illumination of 1 kW/m2. (b) Solar-to-vapor conversion efficiency calculated by the rate of mass change after sunlight illumination for 1 hour. (c) Vapor-evaporation-induced mass changes of water of with various amount of 3DGN under solar illumination of 1 kW/m2. (d) Measured density of ions in the simulated seawater sample (3.5%) before (black) and after (red) desalination with recommended global average salinity bars for drinking water.

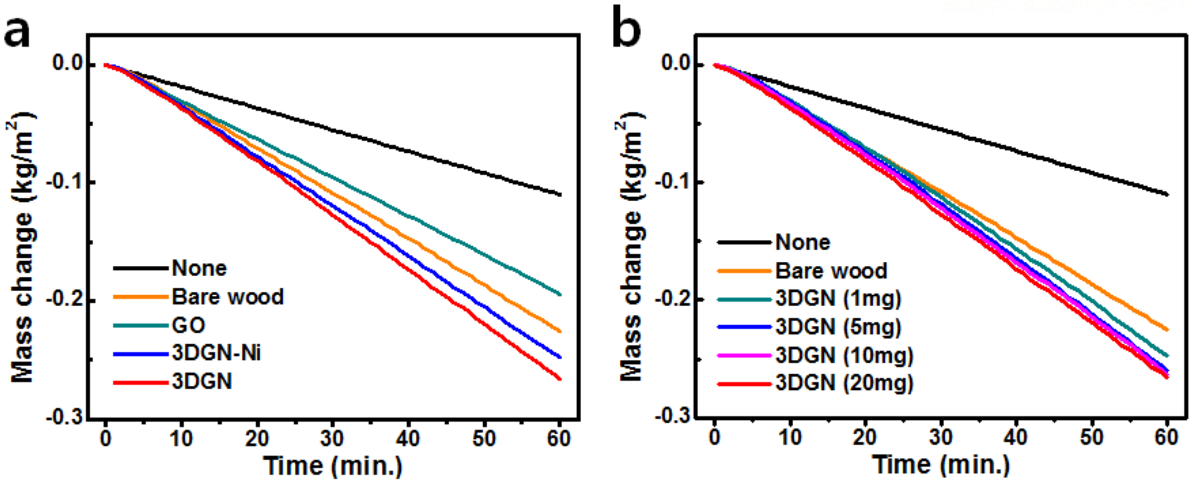

Figure 3.1.10 Vapor-evaporation-induced mass changes of water (a) with 20mg of GO, 3DGN-Ni and 3DGN, and (b) with various amounts of 3DGN samples on the wood pieces as a function of time under dark condition.

Table 3.1.1 The comparison of solar desalination efficiency of the 3DGN deposited on the wood piece with previously reported device measured under 1 sun illumination.

Solar Desalination Device	**Mass Change (kg / m^2 h)**	**Solar-Vapor Conversion Efficiency (%)**	**Reference**
3DGN / wood	1.64	91.8	**This study**
h-G foam	1.4	91.4	Adv. Mater., 2017 [2d]
GDY/CuO CF	1.55	91	Chem. Mater., 2017 [5b]
VA-GSM	1.62	86.5	ACS Nano, 2017 [6]
3D-CG/GN	1.25	85.6	Adv. Mater., 2017 [5d]
Porous N-doped graphene	1.50	80	Adv. Mater., 2015 [4c]
GO / 2D water path	1.45	80	PNAS, 2016 [10b]
Carbonized mushroom	1.475	78	Adv. Mater., 2017 [5e]
F-wood	1.05	72	ACS Appl. Mater. Interfaces, 2017 [5g]
Al NPs / AAM	1	58	Nat. Photonics, 2016 [3b]

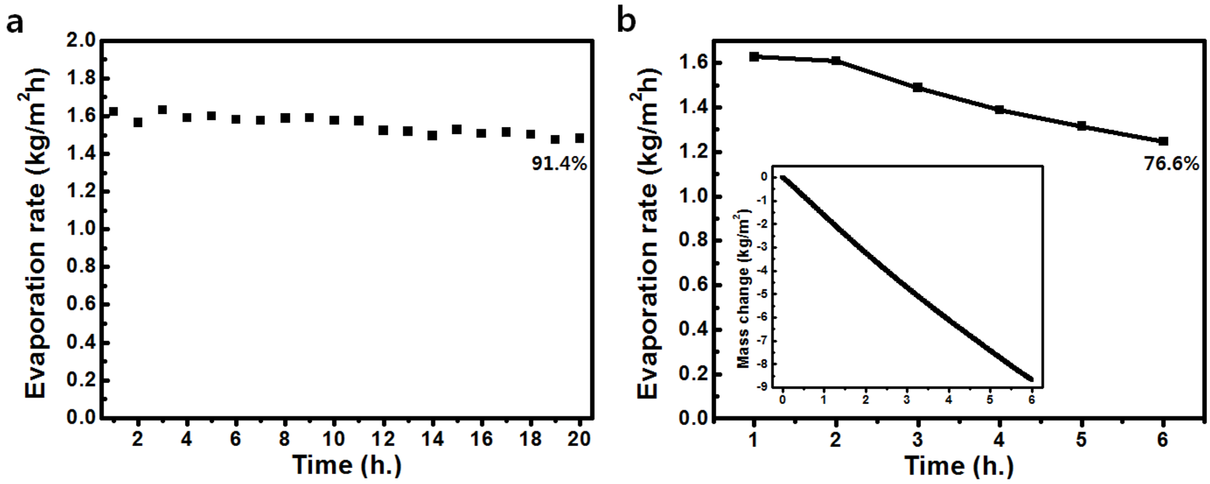

Figure 3.1.11 Durability evaluation through the confirmation of (a) cyclic perfomance and (b) long-time stability.

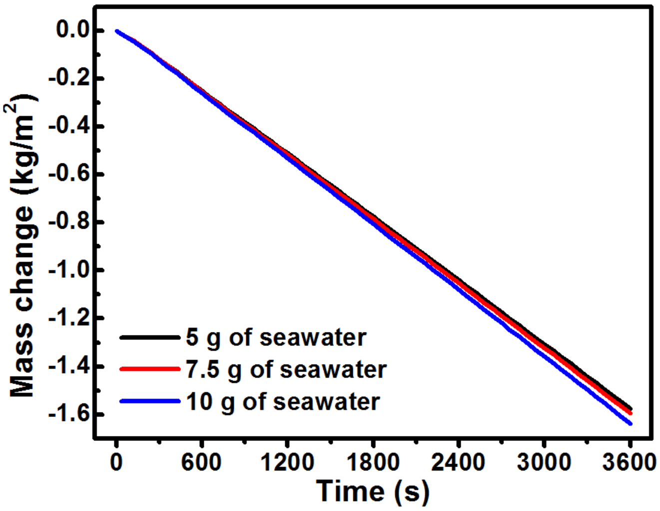

Figure 3.1.12 Mass change as the different quantities of seawater.

3.1.4 Conclusion

Mass-producible 3DGN exhibits excellent properties as an optimized photoabsorber material for an efficient solar desalination device including outstanding photo-absorption of over 90% at broadband wavelength of sunlight and a micro/mesoporous structure with a large surface area of more than 1200 m2/g, which helps vapors to easily nucleate and escape into the air. Furthermore, the wood post delivers the water from the bulk to sites of evaporation and enables the heat generated from the 3DGN photo-absorber material to localize only at the surface via thermal insulation and thereby minimize the heat loss to the bulk water. 3DGN deposited on a wood post can serve as an effective solar desalination device with excellent solar-to-vapor conversion efficiency of over 91.8%, about 35% higher than the efficiency of the broadly used GO deposited on a wood post under the same sunlight illumination condition (one sun, 1 kW/m^2). This is superior to the world-record values documented in previously reported studies. Since the entire device consists of mass-producible and inexpensive materials, it can provide a straightforward solution for the serious global water scarcity problem.

3.1.5 References

1. J. Bartram, C. Brocklehurst, M. Fisher, R. Luyendijk, R. Hossain, T. Wardlaw and B. Gordon, International Journal of Environmental Research and Public Health, 2014, 11, 8137.
2. L. Zhou, Y. Tan, D. Ji, B. Zhu, P. Zhang, J. Xu, Q. Gan, Z. Yu and J. Zhu, Science Advances, 2016, 2, e1501227.
3. M. Fujiwara and T. Imura, ACS Nano, 2015, 9, 5705-5712.
4. M. Gao, P. K. N. Connor and G. W. Ho, Energy & Environmental Science, 2016, 9, 3151-3160.
5. H. Ren, M. Tang, B. Guan, K. Wang, J. Yang, F. Wang, M. Wang, J. Shan, Z. Chen, D. Wei, H. Peng and Z. Liu, Advanced Materials, 2017, 29, 1702590.
6. X. Wang, G. Ou, N. Wang and H. Wu, ACS Applied Materials & Interfaces, 2016, 8, 9194-9199.
7. L. Zhou, Y. Tan, J. Wang, W. Xu, Y. Yuan, W. Cai, S. Zhu and J. Zhu, Nature Photonics, 2016, 10, 393-398.
8. M. S. Zielinski, J.-W. Choi, T. La Grange, M. Modestino, S. M. H. Hashemi, Y. Pu, S. Birkhold, J. A. Hubbell and D. Psaltis, Nano Letters, 2016, 16, 2159-2167.
9. Y. Liu, S. Yu, R. Feng, A. Bernard, Y. Liu, Y. Zhang, H. Duan, W. Shang, P. Tao, C. Song and T. Deng, Advanced Materials, 2015, 27, 2768-2774.
10. Y. Fu, G. Wang, T. Mei, J. Li, J. Wang and X. Wang, ACS Sustainable Chemistry & Engineering, 2017, 5, 4665-4671.
11. G. Zhu, J. Xu, W. Zhao and F. Huang, ACS Applied Materials & Interfaces, 2016, 8, 31716-31721.
12. Y. Ito, Y. Tanabe, J. Han, T. Fujita, K. Tanigaki and M. Chen, Advanced Materials, 2015, 27, 4302-4307.
13. Y. Liu, X. Wang and H. Wu, Chemical Engineering Journal, 2017, 309, 787-794.
14. X. Gao, H. Ren, J. Zhou, R. Du, C. Yin, R. Liu, H. Peng, L. Tong, Z. Liu and J. Zhang, Chemistry of Materials, 2017, 29, 5777-5781.
15. S. Yu, Y. Zhang, H. Duan, Y. Liu, X. Quan, P. Tao, W. Shang, J. Wu, C. Song and T. Deng, Scientific Reports, 2015, 5, 13600.
16. Y. Li, T. Gao, Z. Yang, C. Chen, W. Luo, J. Song, E. Hitz, C. Jia, Y. Zhou, B. Liu, B. Yang and L. Hu, Advanced Materials, 2017, 29, 1700981.
17. N. Xu, X. Hu, W. Xu, X. Li, L. Zhou, S. Zhu and J. Zhu, Advanced Materials, 2017, 29, 1606762.
18. K.-K. Liu, Q. Jiang, S. Tadepalli, R. Raliya, P. Biswas, R. R. Naik and S. Singamaneni, ACS Applied Materials & Interfaces, 2017, 9, 7675-7681.
19. G. Xue, K. Liu, Q. Chen, P. Yang, J. Li, T. Ding, J. Duan, B. Qi and J. Zhou, ACS Applied Materials & Interfaces, 2017, 9, 15052-15057.
20. M. Zhu, Y. Li, F. Chen, X. Zhu, J. Dai, Y. Li, Z. Yang, X. Yan, J. Song, Y. Wang, E. Hitz, W. Luo, M. Lu, B. Yang and L. Hu, Advanced Energy Materials, 2017, DOI: 10.1002/aenm.201701028, 1701028.

21. C. Chen, Y. Li, J. Song, Z. Yang, Y. Kuang, E. Hitz, C. Jia, A. Gong, F. Jiang, J. Y. Zhu, B. Yang, J. Xie and L. Hu, Advanced Materials, 2017, 29, 1701756.
22. X. Wu, G. Y. Chen, W. Zhang, X. Liu and H. Xu, Advanced Sustainable Systems, 2017, 1, 1700046.
23. Q. Jiang, H. Gholami Derami, D. Ghim, S. Cao, Y.-S. Jun and S. Singamaneni, Journal of Materials Chemistry A, 2017, 5, 18397-18402.
24. P. Zhang, J. Li, L. Lv, Y. Zhao and L. Qu, ACS Nano, 2017, 11, 5087-5093.
25. F. M. Canbazoglu, B. Fan, A. Kargar, K. Vemuri and P. R. Bandaru, AIP Advances, 2016, 6, 085218.
26. J.-S. Lee, S.-I. Kim, J.-C. Yoon and J.-H. Jang, ACS Nano, 2013, 7, 6047-6055.
27. J.-C. Yoon, J.-S. Lee, S.-I. Kim, K.-H. Kim and J.-H. Jang, Scientific Reports, 2013, 3, 1788.
28. Y. Fu, T. Mei, G. Wang, A. Guo, G. Dai, S. Wang, J. Wang, J. Li and X. Wang, Applied Thermal Engineering, 2017, 114, 961-968.
29. X. Li, W. Xu, M. Tang, L. Zhou, B. Zhu, S. Zhu and J. Zhu, Proceedings of the National Academy of Sciences, 2016, 113, 13953-13958.
30. A. R. Sadrolhosseini, A. S. M. Noor, K. Shameli, A. Kharazmi, N. M. Huang and M. A. Mahdi, Journal of Nanomaterials, 2013, 2013, 986764.
31. K. Bae, G. Kang, S. K. Cho, W. Park, K. Kim and W. J. Padilla, Nature Communications, 2015, 6, 10103.
32. K. Kim, P. Thiyagarajan, H.-J. Ahn, S.-I. Kim and J.-H. Jang, Nanoscale, 2013, 5, 6254-6260.
33. K. Kim, S. Yu, C. An, S.-W. Kim and J.-H. Jang, ACS Applied Materials & Interfaces, 2018, 10, 15602-15608.

Publication list

1. **Kwanghyun Kim**, Sunyoung Yu, Cheolwon An, Sung-Wook Kim and Ji-Hyun Jang*, Mesoporous Three-Dimensional Graphene Networks for Highly Efficient Solar Desalination under 1 sun Illumination, *ACS Applied Material & Interfaces*, 2018, 10(18), 15602-15608.

2. **Kwanghyun Kim**, Sunyoung Yu, Sung-Wook Kim, Taegeon Kim, Sang-Min Kim, Se-Young Kang, Seung Min Han*, and Ji-Hyun Jang*, Highly Transparent Poly(glycidyl methacrylate-co-acryloisobutyl POSS) for 100 μm-thick Submicron Patterns with an Aspect Ratio over 100, *Chemical Communications*, 2017, 53, 8172-8175.

3. **Kwanghyun Kim**, Jeongyeop Lee, Gyeongcheon Jo, Seungmin Shin, Jin-Baek Kim, and Ji-Hyun Jang*, Dendrimer-Capped Gold Nanoparticles for Highly Reliable and Robust Surface Enhanced Raman Scattering, *ACS Applied Materials & Interfaces*, 2016, 8(31), 20379-20384.

4. **Kwanghyun Kim**, Ik-Hee Kim, Ki-Yong Yoon, Jeongyeop Lee, and Ji-Hyun Jang*, α-Fe_2O_3 on Patterned Fluorine Doped Tin Oxide for Efficient Photoelectrochemical Water Splitting, *Journal of Materials Chemistry A*, 2015, 3, 7706-7709.

5. Chang Hong Bak, **Kwanghyun Kim**, Kyoung Ok Jung, Jin-Baek Kim*, and Ji-Hyun Jang*, Efficient Photoelectrochemical Water Splitting of Nanostructured Hematite on Three-dimensional Nanoporous Metal Electrode, *Journal of Materials Chemistry A*, 2014, 2, 17249-17252.

6. Ki-Yong Yoon, Jung-Soo Lee, **Kwanghyun Kim**, Chang-Hong Bak, Sun-I Kim, Jin-Baek Kim, and Ji-Hyun Jang*, Hematite-Based Photoelectrochemical Water Splitting Supported by Inverse Opal Structures of Graphene, *ACS Applied Material & Interfaces*, 2014, 6(24), 22634-22639.

7. Hyo-Jin Ahn, Myeong-Jong Kim, **Kwanghyun Kim**, Myung-Joon Kwak, and Ji-Hyun Jang*, Optimization of Quantum Dot-Sensitized Photoelectrode for Realization of Visible Light Hydrogen Generation, *Small*, 2014, 10(12), 2325-2330.

8. **Kwanghyun Kim**, Myeong-Jong Kim, Sun-I Kim, and Ji-Hyun Jang*, Towards Visible Light Hydrogen-Generation: Quantum-Dot Sensitization via Efficient Light Harvesting of Hybrid-TiO_2, *Scientific Reports*, 2013, 3, 3330.

9. **Kwanghyun Kim**, Pradheep Thiyagarajan, Hyo-Jin Ahn, Sun-I Kim, and Ji-Hyun Jang*, Optimization for Visible Light Photocatalytic Water Splitting: Gold-Coated and Surface-Textured TiO_2 Inverse Opal Nano-Networks, *Nanoscale*, 2013, 5(14), 6254-6260.

10. Jong-Chul Yoon, Jung-Soo Lee, Sun-I Kim, **Kwanghyun Kim**, and Ji-Hyun Jang*, Three-Dimensional Graphene Nano-Networks with High Quality and Mass Production Capability via Precursor-Assisted Chemical Vapor Deposition, *Scientific Reports*, 2013, 3, 1788.

*** Note that following contents are reroduced with permissions.**

2.1 of **Chapter 2** is reproduced in part with permission of “Optimization for Visible Light Photocatalytic Water Splitting: Gold-Coated and Surface-Textured TiO_2 Inverse Opal Nano-Networks”, Copyright @ 2013 Royal Society of Chemistry.

2.2 of **Chapter 2** is reproduced in part with permission of “Towards Visible Light Hydrogen-Generation: Quantum-Dot Sensitization via Efficient Light Harvesting of Hybrid-TiO_2”, Copyright @ 2013 Springer Nature.

2.3 of **Chapter 2** is reproduced in part with permission of “α-Fe_2O_3 on Patterned Fluorine Doped Tin Oxide for Efficient Photoelectrochemical Water Splitting”, Copyright @ 2015 Royal Society of Chemistry.

3.1 of **Chapter 3** is reproduced in part with permission of “Mesoporous Three-Dimensional Graphene Networks for Highly Efficient Solar Desalination under 1 sun Illumination”, Copyright @ 2018 American Chemical Society.

Acknowledgement

2018 년 봄은 제 인생에 있어서 가장 크다고 할 수 있는 2 번의 순간이 있었습니다. 결혼의 순간과 학위를 마치는 지금 이 순간이 있었기에 평생 잊지 못할 것입니다. 길고 쉽지 않은 여정이 끝났다고 할 수 있지만, 이것도 인생의 수많은 언덕들 중 조금 더 큰 언덕을 넘은 것이라는 것을 잘 알고 있습니다. 그래서인지 학위를 마치는 이 순간을 아주 간절하게 기다려왔지만, 막상 지금 아무런 실감이 나지 않는 것인지 감흥이 크게 다가오지 않네요. 스스로 많은 부족함을 느끼면서 학위를 마치게 되어서 그런 것 같습니다. 앞으로 부족함을 채우는데 더욱 매진하여 빠른 시일 내에 진정한 박사의 모습으로 거듭나겠습니다. 항상 주어진 모든 일에 최선을 다하는 모습, 계속해서 발전해 나가는 모습을 다짐하며 한 걸음씩 힘든 발걸음을 내딛으며 여기까지 왔다고 생각했는데 마무리하는 이 시점에서 돌아보니 한없이 부끄럽고, 후회되는 일들이 생각납니다. 이런 감정, 생각을 잘 간직하여 앞으로 더 멋진 사람으로 성장해나가도록 더 노력하겠습니다.

아직 부족한 것이 많고, 크게 달라지는 것도 없다는 것을 잘 알지만 그래도 이 한 단계를 넘어서면서 곁에서 도와주신 많은 분들께 작게나마 보답할 수 있는 자리에 겨우 오른 것 같다는 생각이 듭니다. 제 학위를 시작부터 완성까지 부족한 저를 책임지고 이끌어주신 장지현 교수님께 정말 대단히 감사 드립니다. 그리고 많이 바쁘신 중에도 귀한 시간을 내어 심사위원으로 참여해주신 김진영 교수님, 서관용 교수님, 류정기 교수님, 장지욱 교수님께도 정말 감사 드립니다. 그리고 제 연구를 도와주셨던 전석우 교수님과 한승민 교수님께도 감사 드립니다. 또, 실험실 내에서 많은 도움을 주었던 모든 선배님들과 후배들에게 고맙고, 특히 연구를 같이했거나 곁을 지켜주신 분들께는 특별한 감사를 전하고 싶습니다.

그리고 제 주변 분들께도 감사의 말씀을 전하고 싶습니다. 제가 여기까지 올 수 있게 해준 부모님께도 감사 드리고, 저를 예쁘게 봐주시는 안산에 계신 부모님께도 감사의 말씀을 드립니다. 그리고 항상 큰 힘이 되어주는 박사의 길을 동참한 여러 친구들과 형 동생들, 그리고 유니스 친구들에게 정말 감사합니다.

제가 이 학위를 끝까지 잘 마칠 수 있도록 가장 큰 힘이 되어준 사람은 제 아내, 최솔입니다. 많은 저의 부족함을 채워주고, 제가 세상에서 가장 멋지고 똑똑한 사람인 것처럼 자신감을 주는 우리 솔이가 있어서 숱하게 무너질뻔한 순간에도 꿋꿋하게 잘 버티며 이 자리까지 올 수 있었습니다. 정말 사랑하고 많이 감사합니다. 앞으로는 우리 인생에서 온전히 우리의 행복을 위해 살아갈 수 있는 사람이 되겠습니다. 그것이 위 모든 분들에 대한 보답이라고 생각합니다.